NORTHWESTERN UNIVERSITY

Utilizing Point Defects in Zintl Compounds to Understand and Engineer their Thermoelectric Properties

A DISSERTATION

SUBMITTED TO THE GRADUATE SCHOOL
IN PARTIAL FULFILLMENT OF THE REQUIREMENTS

for the degree

DOCTOR OF PHILOSOPHY

Field of Material Science & Engineering

By

Max Wood

EVANSTON, ILLINOIS

December 2020

ABSTRACT

Utilizing Point Defects in Zintl Compounds to Understand and Engineer their Thermoelectric Properties

Max Wood

A significant portion of material science research is concerned with understanding the way that defects affect the properties materials. In the field of thermoelectrics introducing or removing point (0D), dislocation (1D), grain boundary (2D), or precipitate (3D) defects are popular methods for altering a materials thermoelectric efficiency. Herein I discuss different studies conducted during my PhD that focus on using point defects to alter the electronic properties of Zintl based compounds.

Point defects in a material can bring about changes in a material's electronic transport that can be classified as stemming from changes in: carrier concentration/electron chemical potential, band structure, or scattering. Herein lies a discussion of what ways each of these transport parameters are affected by point defects, as well as methods to control point defects that lead to these changes in parameters. This document demonstrates two different methods for controlling carrier concentration via point defects by using secondary phases (Phase Boundary Mapping in ZnSb) or a vapor phase (Saturation Annealing in

Mg_3Sb_2) to set atomic chemical potentials, which in turn affects the materials point defect concentration. This document also discuss how the aliovalent substitution of Al onto the Mg site of $Yb_{14}MgSb_{11}$ can be used to shift the Fermi-level of a material to learn about its underlying band structure. The final two chapters of this document focus more on how point defects can lead to changes in transport that do not necessarily deal with changes in carrier concentration. This includes how isovalent substituion of Mg onto Zn site of $CaZn_2Sb_2$ can be used to alter the band structure of the compound, or how isovalent Yb substitution onto the Mg site in $Mg_3Sb_{1.5}Bi_{0.5}$ can result in an increase in scattering due to changes in bonding in the material.

Acknowledgements

Dedication: Dedicated to the community of women from Iowa (Sunny, Lori, Peg, Bridget, Sue, Charleton, and many others) who took care of my Mom (Jeannie). You offered her friendship when she was well, care when she was sick, and support to my brother and me when she was gone. Your presence in her life was instrumental in providing me certainty that my mom was taken care of so that I could be away at grad school. Your presence during the end of and after her life gave me the support I needed to pick up the pieces and go back to grad school. This document, these papers, my future career do not exist without all of you.

Thank you.

Personal Statement: My time at Northwestern has been trying both from personal and professional perspectives. While the acknowledgements section of dissertation is generally focused on thanking those who served more in a professional capacity, I struggle to compartmentalize the support that helped me through the death of my remaining parent and the support that helped my academic pursuits. With this distinction being too unclear I endeavor to acknowledge the efforts of everyone in my community that was instrumental to this work.

Additionally, I plan to use this section to share some of my experiences as a graduate student in the hopes that a future student reading it might feel less alone and more

confident in their pursuits. While I found many university services talking about the concept of "imposter syndrome", I did not find many actual people willing to role-model the vulnerability required to talk about how they felt or had felt that their achievements didn't warrant their positions. I found myself at times thinking, "while others also felt out of place, I am actually out of place." In order to not be found out, I hid. This took the form of me not asking for help when I needed it; not seeking enough feedback on my work; and not taking any risks in promising a deliverable even when I could see the potential growth it could lead to.

In retrospect, I can see the destabilizing force that loosing my father in my senior year of undergrad and knowing my mother was terminally ill was having on my early academic experience at NU. However, at the time I kept these facts closely guarded secrets for fear of being just additional evidence that I would not be able to perform up to the standards of my peers. Putting this into words, I am realizing just how absurd this notion sounds, but I did not feel comfortable at the time sharing it to get this kind of feedback. If you're reading this and anything resonates with you please know you're not alone, it's okay to seek help, and that building a more inclusive environment has to start with someone sharing their experience.

Individual Acknowledgments:

Sam: in the times of most struggle in my life I always knew that I could depend on you. I look back on our mom's final months as one of the happiest times in my life and I know this is only the case because I had you there with me.

Shreya: Thank you for being my partner. Words can not express what the love and support you provided me throughout the past 8 years means to me. I am incredibly

excited for you as you start your own PhD journey and am looking forward to seeing all that you accomplish.

Jeff: Thank you for seeing and believing in a potential in me that I didn't know was there. When entering your group, I didn't envision myself doing anything beyond synthesis and characterization. However, you patiently pushed me to learn analytical tools and concepts that I highly value today, even though they were initially of outside my comfort zone. You gave me responsibilities in interacting with collaborators and working on projects that I didn't feel qualified for, but the success I found with your support convinced me otherwise. Additionally, you allowed me the space and resources to develop and test my own research questions, without feeling a need to seek permission. In this autonomy I found a love of problem solving and discovery, which I hope to take with me for the rest of my life.

Umut: You were the first person I got to know in Jeff's group and you taught me the basics of solid state chemistry, experimental research, paper writing, lab maintenance, and more that I still rely on today. I will forever appreciate the time you invested in me to build the researcher I am today. I am especially thankful for the lunch you took me to after I told you about my mother and the reassurance you gave me that my academic career would continue after my leave of absence.

Jimmy: Thank you for being my scientific sounding board and friend in the lab. I learned so much from talking to you and always felt I could ask you the "dumb" questions I had and not be met with any judgement. Being able to work with you on the two papers we coauthored in an atmosphere where our successes felt completely shared is an

experience I'll cherish. In this thesis Chapter 3 is based on work that Jimmy and I shared first authorship on.

Max (Dylla): we shared a name, a department, an advisor, and for 2 years, an apartment. Right after joining Jeff's group, your ability to quickly understand and then explain topics related to our research was impressive and highly appreciated. The openness with which you discussed the uncertainty in finishing the program made my own insecurities feel normal. Thank you for you vulnerability, friendship, and support.

Wedding planners & photographer (Shane, Chris, Michaela, Rohit & Tiffany): I am so pleased that I got to call you all friends during my time here. You all made me feel so valued as a friend when on a week's notice you planned my wedding with Shreya, including decorating your apartment and baking 3 superb cakes. The months after my leave of absence was a time during which I most questioned if I really belonged at Northwestern, and seeing you all go above and beyond to make the most beautiful wedding reception, reassured me that I had found my people.

Saneyuki, Sam (Miller), and Stephen: as senior students I really appreciated the time you spent helping me navigate the lab, training me on how to use equipment, and role-modeling what successful PhDs and post-PhD careers should look like. Matthias: thank you for your work as social chair for our group; your efforts at making sure everyone was included was always appreciated. Shash: thank you for answering endless questions I had about DFT and defects. I was always in awe of the creativity with which you approached your projects, and was grateful that you included me in your work with half-heuslers. The COHP calculations that Shash performed on Mg_3Sb_2 are included in the 6th chapter of this thesis. Ian: as someone who had previously worked in industry prior to starting your

PhD, I always appreciated you sharing your perspective of what mattered in life and in research. As a desk mate I look back fondly on all the side conversations that we would have throughout the day. Kazuki: I am grateful for the openness with which you included me in your work on Mg_3Sb_2 and your help in the lab. I always knew I could depend on you and felt that our projects were strengthened by our collaborative efforts. The samples Yb alloyed samples that we worked on together form the expiramental section of the 6th capter of this thesis. Muath &Bricker: thank you for all the work you put into helping me with the TECCA project, which allowed me to focus on finishing other projects and graduating. James & Naomi: thank you for all your help in the 14-1-11 synthesis. You both were a joy to get to know and work with. Ramya: I enjoyed getting to know you in my last three years, and really value our conversations regarding life and our families that we shared. Maddy: thank you for pointing out all the hard homework questions in Jeff's class to me 3 days before anyone else got to them, giving me time to figure out what response I should give. Michael: thank you for all the work you put into doing defect calculations on ZnSb and $Yb_{14}MgSb_{11}$, and for your work in reformatting our ZnSb paper. Shristi & Naomi : thank you giving me the chance to get to practice my role in research mentorship. The summer project that Shristi and I worked on together forms the 2nd chapter of this thesis. Tyler: thank you for letting me use equipment in the Kantazidis lab and for all the discussions on thermoelectrics that we shared. Alex: thank you for including me on your work on graphene-wrapped Mg_3Sb_2, and for house sitting our cat while we were away. Kent: I am very grateful that I got to know you before leaving. I look forward to using your advice and experience as a post-doc in my next endeavor.

I also want to thank all students, researchers and faculty who attended the JPL calls every week, gave me feedback on my work, and let me ask questions about their work. Sabah: you felt like a second PI to me who I could email if I had a question and who validated my work on projects related to our collaboration. Prof Kauzlarich and Chris: getting to work with you on the muti-band model for the $Yb_{14}Mg_{1-x}Al_xSb_{11}$ solid solution that forms Chapter 4 of this thesis was a highlight of my PhD, and I am very grateful for your patience in the time I developed what my contribution would be. I also need to thank Prof. Hautier and Franceco for computing the band structures discussed in chapter 4. Finally thank you to Prof. Haile, Prof. Poeppelmeier, and Prof. Wolverton for taking the time to read this document and serve as members of my committee.

Table of Contents

List of Tables

List of Figures

CHAPTER 1

Introduction

1.1. Zintl-Klemm Concept

1.1.1. Historical Reference

Roald Hoffman has stated the Zintl-Klemm concept is "the single most important theoretical concept in solid state chemistry of the last century" [27]. In order to understand the importance of Zintl-Klemm concept its useful to understand the historical context in which it arose. In 1916 Walther Kossel [28] and Gilbert Lewis [29] independently published separate works that identified the octet rule. While both scientists identified the tendency of main group elements to bond in ways that lead to a filled octet, Kossel's perspective of bonding would be today more closely associated with ionic bonding, while Lewis's would be thought of as covalent bonding [30]. Three years later Langmuir introduced the concept of a formal charge in an attempt to broaden these concept to apply to elements that did not always bond in ways reflective of their actual or perceived electron count at the time. [31].

In 1913 William and Henry Bragg published their seminal findings on the reflection of x-rays by crystals [32]. As the field of x-ray crystallography developed more structural information for various elements and compounds became available and scientists began developing theories to explain and predict these structures. Goldschmidt deduced atomic raddii for a number of elements based on their closed-packed structures [33]. Hume-Rothery

took this information, as well as available information on atomic radii determined from ionic salts, and developed rules to predict atomic structures and solid solutions based on atomic radii, valency, and electronegativity of the elements involved in bonding[34;35;36].

A)

Fig. 1.—The Sodium Chloride Structure.

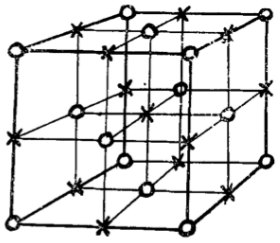

O +VE OR Na^+ IONS.
× −VE OR Cl^- IONS.

If a univalent face-centred cubic metal has this structure, the positive metallic ions are shown as circles, O, and the negative electrons as crosses, ×.

B)

Fig. 6.

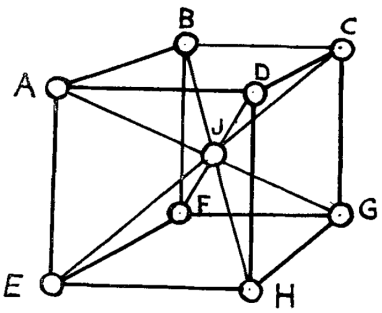

The Body-centred Cubic Structure.

C)

$$\frac{2r_1}{\sqrt{2}} = r_1 + r_2.$$

If $\frac{2r_1}{\sqrt{2}} < r_1 + r_2$, then the closing-up process is stopped by the contact of unlike ions;

D)

TABLE III.

Ionic Radii deduced on the assumption that $Cs^+ = I' = 1{\cdot}974$ Å.

Li^+	= 1·041		
Na^+	= 1·257	F'	= 1·041 ?
K^+	= 1·552	Cl'	= 1·589
Rb^+	= 1·689	Br'	= 1·739
Cs^+	= 1·974	I'	= 1·974

Figure 1.1: A collection of figures, equations, and tables taken from "The Metalic State" published by Dr. W. Hume-Rothery in 1927. A) NaCl structure B) Body Centered Cubic structure, C) Equation showing the critical atomic ratio of cations and anions to form the rock salt structure D) Table of ion radii calculated by Dr. Hume-Rothery from existing data on different salt lattice paramters.

While the Hume-Rothery rules could rationalize the structures of a number of compounds there are notable exceptions including several binary compounds studied by Eduard Zintl containing electroposative metals bonded with semimetals[37;38;39]. An often cited example of one such compound is NaTl. Based on the Hume-Rothery rules at the

time, MgHg and NaTl were expected to crystallize in the same structure. The valence electron count of both compounds were deemed comparable with Mg having one extra electron compared to Na and Hg having one less electron compared to Tl, and Na/Mg and Hg/Tl were thought to have similar atomic radii. Considering that MgS and NaCl both crystallize in the rock salt structure can potentially help our modern perspective empathize with what scientists were trying to reconcile at the time. When investigating these structures Zintl noted MgHg crystallized in a BCC structure with an atomic coordination number of 8, while NaTl crystallized in a diamond like structure with an atomic coordination number of 4 (Figure: 1.2)[30]. Assuming non-directional bonding, where ions are modeled as hard spheres with a charge one could potentially rationalize a switch from 8 to 6 coordination or 6 to 4 coordination between these compounds due to slight changes in atomic radii, but moving from 8 to 4 coordination in two compounds composed of elements adjacent to each other on the periodic table couldn't be explained by Home-Rothery.

Through Zintl's work and those who continued it after his early passing in 1941, we have come to understand the structure in NaTl is different than MgHg becasue NaTl is composed of a mixture of ionic and covalent bonding. If we consider that the electropositive Na atom donates an electron to the Thulium, then we can think of the Tl^- valence electron count is 4. As a consequence the Tl^- ion acts as a tetrahedrally bonded, 4 valence electron species and forms a diamond like framework with other Tl^- ions.

Today the term Zintl compound is used to describe compounds where there is a large degree of electron transfer between some atom and a sharing of electron density between

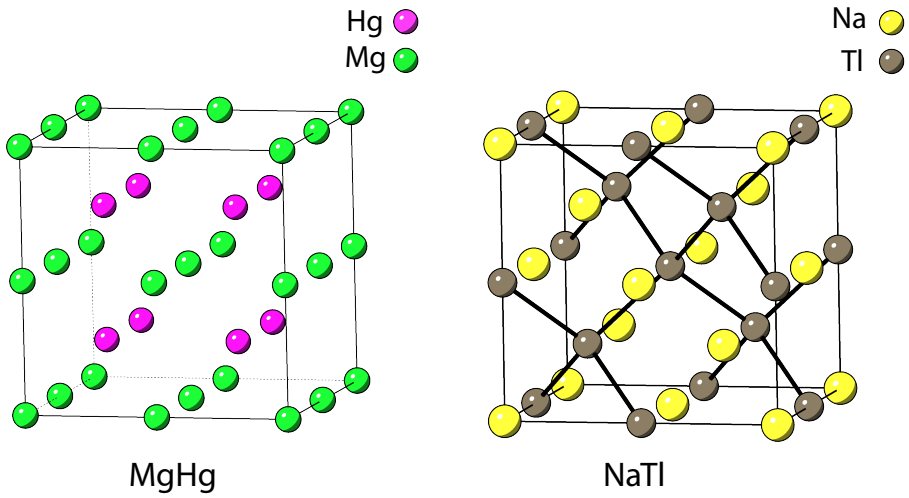

Figure 1.2: Crystal Structures for MgHg and NaTl. Note how the two compound have the same net valence and are composed of elements adjacent on the periodic table yet this slight difference in chemistry leads to significantly different crystal structures.

other atoms, or in other words compounds that have a mixture of ionic bonding and covalent bonding present among different atoms in the same compound. Typically this is composed of highly electroposative cations that donate their electrons to an poly anionic substructures, though polycationic zintl phases do exist[40]. Anions within a Zintl form covalent bonds such that with the addition of the cation electrons every atom making up the anionic structure has a filled octet. Nesper[41] and Miller[42] have stated on the topic: there exists a well-defined relationship between chemical and electronic structures in a Zintl phase and a chemist can understand the structure by using simple electron counting rules.

1.1.2. Zintl Counting Rules

Zintl compounds are different from other intermetallics by their valence precise nature. One way of formulating this concept is through the 8-N rule, where N is the total valence electron count. In a binary compound, A_aX_x where A is the ionizing species and X is the covalently bonded species normalized valence electron count (VEC) is given by:

$$VEC = \frac{a \cdot e(A) + x \cdot e(X)}{x} \tag{1.1}$$

Where $e(A)$ is the electron count for atom A, and $e(X)$ is the electron count for atom X. Using NaTl as an example, Na has 1 valence electron and Tl has 3 meaning the total valence electron count for the compound is 4. This requires that for the structure to be zintl phase, there would be 4 covalent bonds in the material, which is expressed by the Tl atom being tetrahedral coordinated.

Another example that highlights the usefulness of the Zintl-Klemm concept is contrasting how the differences in bonding in ZnSb and β - Zn_4Sb_3 (Figure 1.3) can explain thier semiconducting properties. Without any knowledge of structure one may niavely consider ZnSb to be a p-type metalic conductor due to its valence electron count (e(Zn) + e(Sb) = 2 + 5 = 7)[43]. However, with knowledge of the structure we can identify an [Sb−Sb] diamer that can effectively explain a valence count that leads to semi-conducting behavior. Each Sb atom starts with 5 valence electrons; add to this the 2 valence electrons donated from the Zn atoms and one half of a 2-centered 2-electron (2c-2e) bond between Sb atoms and we arrive at a valence count of 8 electrons per Sb atom.

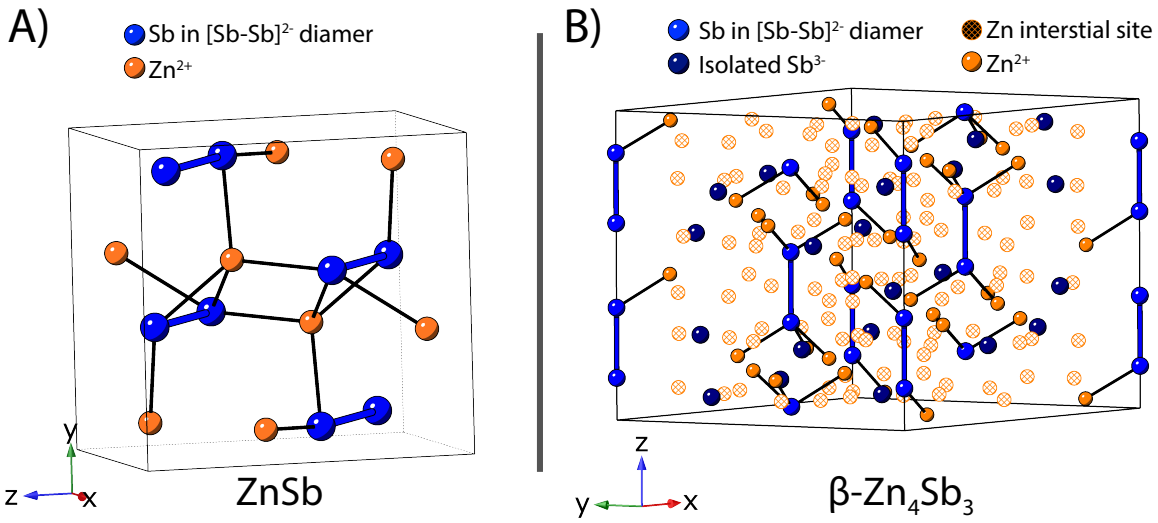

Figure 1.3: Crystal Structures for A) ZnSb and B) β-Zn_4Sb_3. In these structures Sb atoms and the bond between Sb atoms that forms the Sb-Sb diamer are light blue for distinction, isolated Sb atoms are dark blue, Zn atoms are orange, and interstial sites for Zn atoms are marked with an orange cross hatch.

Another way of checking that a compound is valence balanced is by breaking the compound into the compound into its ionic and polyionic components that form the primative unit cell, assigning charges to these species, and checking to make sure these species's charges cancel. Using ZnSb again as an example we would assign the fully ionized Zn atom to have a charge of 2+ after loosing its 4s electrons and the [Sb−Sb] diamer a charge of 4- as two additional electrons are needed for each Sb atom to have a full octet. The primitive unit cell of ZnSb is composed of 8 formula units such that: $8Zn^{2+} + 4[Sb{-}Sb]^{4-} = 8ZnSb^{0}$.

This second method makes valence counting in complex structures made of poly-ionic structure motifs significantly easier such as those found in β-Zn_4Sb_3[44] [45]. The chemical name β-Zn_4Sb_3 is a bit misleading as high resolution diffraction has shown the actual stoichiometry to be $Zn_{3.83}Sb_3$. The bonding in this compound in the unit cell is composed of 60 sb atoms in $6[Sb{-}Sb]^{4-}$ diamers and 18 stand alone Sb^{3-} ions summing to a charge state of -78. The zinc atoms in this compound are disordered with 36 Zn^{2+} sites considered close to fully occupied framework sites summing to a total charge state of +72. In a charge neutral intrinsic semi-conductor we would expect for there to be an additional 3 Zn^{2+} occupying interstitial sites (Figure 1.3B) $39Zn^{2+} + 6[Sb{-}Sb]^{4-} + 18Zn^{3-} = 3Zn_{13}Sb_{10}{}^{0}$. However, structure refinements have found only enough charge density to account for another 2.3 sites occupied per unit cell[45]. One might be tempted to think this valence imbalance would indicate β-Zn_4Sb_3 is not a Zintl-phase, howevever this Zn defeciency perfectly accounts for the degenerate p-type carrier concentration found in β-Zn_4Sb_3 samples.

Beyond helping us establish what is and isn't a Zintl phase, these charge counting rules can also serve as a helpful guide for what dopants should be used to change the

carrier concentration in a Zintl semi-conductor. If p-type transport is desired from an intrinisic Zintl-phase then doping strategies that reduce the valence elctron count are desired, whereas if n-type transport is desired dopants that increase the valence electron count should be considered. The most common doping strategy found in the literature is through the use of substitutional defects, though using non-stoichemtric nominal compositions to induce vacancies or interstitial type defects are also common.

Considering Mg_3Sb_2 as an example substituting a small fraction of the Mg ($[Ne]3s^2$)) sites with Na ($[Ne]3s^1$) would result in a reduction of the valence electron count and therefore lead to an increased p-type carrier concentration. Meanwhile substituting Sb ($[Kr]4d^{1}05s^{2}5p^{3}$) with Te($[Kr]4d^{1}05s^{2}5p^{4}$) would result in an increase in the valence electron count and consequently an increased n-type carrier concentration. We can also consider what effect intrinsic defects would have on Mg_3Sb_2 carrier concentration. If extra Mg was added to Mg_3Sb_2 during synthesis, we would expect there to be an increased concentration of Mg interstitial and Sb vacancies. Based on our Zintl counting rules we would expect both of these defects to add electrons as interstitial Mg would likely ionize to Mg^{2+} donating 2 electrons and an Sb vacancy reduces two electron states that Mg electrons were previously occupying. Adding extra Sb to the synthesis of Mg_3Sb_2 would result in Mg vacancies, which we would reduce the valence electron count and lead to an increase in p-type carrier concentration.

1.2. Point Defects

1.2.1. Defect Formation Energy

The formation energy of a point defect can be computationally calculated by equation 1 [46;6].

$$E^f\left[X^q\right] = E_{tot}\left[X^q\right] - E_{tot}\left[bulk\right] - \sum_i n_i\mu_i + qE_F \tag{1.2}$$

Where $E_{tot}\left[X^q\right]$ is the total energy derived from a supercell calculation containing a defect represented by X with a charge of q. $E_{tot}\left[bulk\right]$ is the energy of the supercell had the defect not been in place. n_i is the number of impurity atoms of chemical potential μ_i added ($n_i > 0$) or taken away ($n_i < 0$) to make the defect. q is the charge of the defect created, and E_F is the chemical potential of electrons also referred to as the Fermi energy. For the sake of simplicity I am leaving out a number of subtleties and considerations that must be taken into account when calculating a defect's formation energy. For a more extensive review please see Freysoldt C et al. [6].

The first thing to note equation 1.2 is that the formation energy of charged defects is dependent on the host phase's Fermi energy. Figure 1.4, shows a defect formation energy diagram of an amphoteric defect with three charge states. As the Fermi-Energy approaches the conduction band, the energy of a negatively charged defect (hole creating) becomes more favorable, whereas as the Fermi-Energy approaches the valence band the energy of a positively charged defect (electron creating) becomes more favorable. Intuitively this can be explained through le Chatelier's principle. As the system becomes

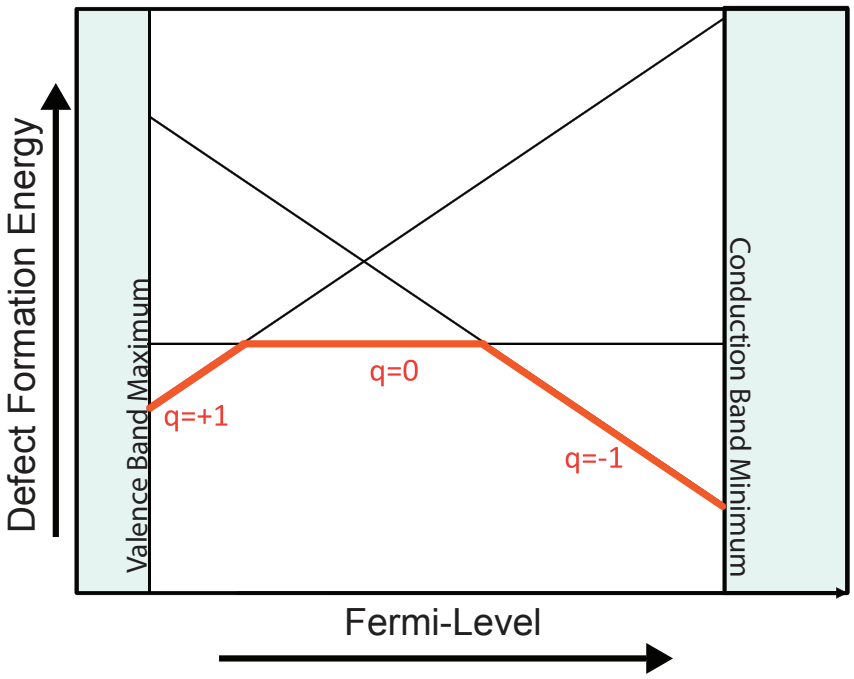

Figure 1.4: Modified from Freysoldt C et al.[6]. Schematic illustration of formation energy (E^f) vs Fermi level (E_F) for an amphoteric defect that occurs in three charge states. At the valence band maximum (VBM) there are three different energies that equation 1 has calculated corresponding to charge of +1 on the bottom, 0 in the middle and -1 with the highest formation energy. As the Fermi energy increases to the conduction band minimum (CBM), the energy of these defects change such that they cross at different points. The bolded orange line gives the formation energy of this defect at different Fermi energies as it changes charge.

more electron rich the energy of electron accepting defects will decrease, and as the system becomes more electron poor the energy of electron donating defects will decrease.

The second important concept to grasp from equation 1.2 is that the formation energy of charged defects is dependent on the chemical potential reservoir that the defect atoms are coming from or going to. The chemical potential of an atom is the change in energy of a system associated by adding or removing said atom. It is given by $\mu_i = \left(\frac{\partial G}{\partial N_i}\right)_{T,P,N_{j\neq i}}$ where G is the Gibbs free energy, N_i is the number of particles of species i, given that

temperature, pressure, and number of particles of other species are held constant[47]. Intuitively, this can be rationalized as: if a defect requires an atom to be removed from the main phase and placed into a high energy reservoir, the total energy of this defect will be higher compared to if the atom could have been placed in a lower energy reservoir.

Consequently, equation 1.2 gives us two tools to change the formation energy, and thereby concentration of charged defects in a material. One is changing the Fermi level of the material, and the second is changing the chemical potential of the atoms in the material. Unfortunately, the goal of understanding and controlling formation energies was to have a better control over Fermi level and carrier concentration. This leaves the only dial to control defect formation energy available to an experimentalist as changing the chemical potentials of the atomic species.

1.2.2. Chemical Potential

Understanding and controlling chemical potentials requires first an understanding of equilibrium and the Gibb's phase rule. Two phases in a closed system (total volume, total energy, and total number of particles remain constant) are said to be in equilibrium if both phases have the same temperature, pressure, and chemical potentials of their atomic species[47]. The Gibb's phase rule is used to find a system's degrees of freedom or the largest number of independent intensive variables that can be varied simultaneously and arbitrarily without determining one another[47]. The Gibb's phase rule is given by $F = C - P + 2$, where F is the degrees of freedom in the system, C is the number of components in the system, and P is the number of phases in thermodynamic equilibrium. At constant pressure and temperature, the Gibb's phase rule can be rewritten as $F = C - P$.

The chemical potentials of atoms in a sample are variable when temperature and pressure are not held constant. Given that temperature and pressure are constant, when a homogeneous sample's composition lays within a single-phase region of a multi component phase diagram the chemical potential of the atoms in that sample can still change with changes in composition. However in an n-phase region of an n-component phase diagram (n being any integer number), the composition of each phase remains invariant with changes to the system's composition due to the Gibb's phase rule. To make up for the system's compositional change the relative amounts of each phase change. Because the compositions of each phase are fixed with regards to a system's changing composition, the chemical potentials of the atomic species in each phase are also fixed. Additionally the chemical potentials of each atomic species must be the same across all phases, or else the system wouldn't be in equilibrium[47]. Considering Mg_3Sb_2, the chemical potentials of Mg and Sb are linked by the formation energy of the Mg_3Sb_2 phase[6].

$$3\mu_{\mathrm{Mg}} + 2\mu_{\mathrm{Sb}} = \mu(\mathrm{Mg_3Sb_2}) \tag{1.3}$$

Where $\mu(\mathrm{Mg_3Sb_2})$ is the formation energy/formula unit of Mg_3Sb_2. Bounds of the chemical potentials of the constituent elements are set by the formation of metallic Mg and Sb.

$$\mu_{\mathrm{Mg}} \leq \mu(\mathrm{Mg}\ \mathit{metal}) \tag{1.4}$$

$$\mu_{\mathrm{Sb}} \leq \mu(\mathrm{Sb}\ \mathit{metal}) \tag{1.5}$$

Combing equations 1.3, 1.4, and 1.5 we can also obtain the upper bounds for the chemical potentials of the atomic species.

$$\mu_{\mathrm{Sb}} \geq \frac{1}{2}\mu\left(\mathrm{Mg_3Sb_2}\right) - \frac{3}{2}\mu\left(\mathrm{Mg}\ metal\right) \tag{1.6}$$

$$\mu_{\mathrm{Mg}} \geq \frac{1}{3}\mu\left(\mathrm{Mg_3Sb_2}\right) - \frac{2}{3}\mu(\mathrm{Sb}\ metal) \tag{1.7}$$

Equations 1.3- 1.7 are generally true for finding the bounds of the chemical potentials of atomic species in a phase, and require reference chemical potentials for magnesium metal and antimony metal. These references can either be taken computationally, from electronic structure calculations giving the total energy of an elemental phase at 0K, or experimentally from databases with thermodynamic data at specified conditions[6].

In Mg_3Sb_2 there are two phase-spaces in which the compositions of the system's phase are locked with changing composition, Mg_3Sb_2 in equilibrium with Mg, and Mg_3Sb_2 in equilibrium with Sb. These fixed compositions come with fixed chemical potentials, which allow us to determine the chemical potentials of the target phase in relation to its impurity phase. For example in the case of Mg_3Sb_2 in equilibrium with Mg, the chemical potentials become $\mu_{\mathrm{Mg}} = \mu(\mathrm{Mg}\ metal)$ and $\mu_{\mathrm{Sb}} = \frac{1}{2}\mu\left(\mathrm{Mg_3Sb_2}\right) - \frac{3}{2}\mu(\mathrm{Mg}\ metal)$, assuming antimony's solubility in magnesium is negligible. This provides one extremum for values of chemical potentials, with the other being in the two-phase region of Mg_3Sb_2 in equilibrium with Sb. This means at compositional extremums of a compound; one can determine the extremums

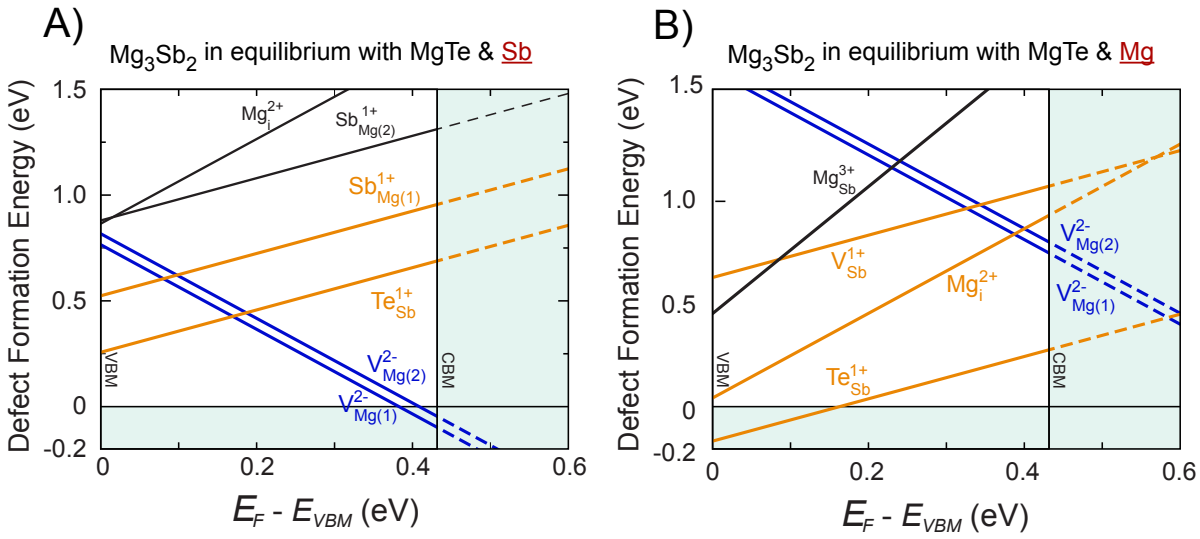

Figure 1.5: Modified from Ohno et al.[7] (A) Defect Formation energy diagram of Mg_3Sb_2 in equilibrium with Sb and MgTe (B)Defect Formation energy diagram of Mg_3Sb_2 in equilibrium with Mg and MgTe

of chemical potentials of its atomic species. This in turn determines the extremums of defect formation energies, and ultimately extremums in obtainable carrier concentration.

1.2.3. Interpreting Defect Formation Energy Diagrams

Figure 1.5 shows a defect formation energy diagram for Te doped Mg_3Sb_2 in the cases where it is Sb rich and Mg rich. The y axis intercept is the enthalpic contribution to the formation energy of each defect species and gives the defect formation energy at the valence band maximum. Lines are labeled with their defect type and relative charge with positive defects (electron producing/Fermi level increasing) having positive slopes and negatively charged defects (hole producing/Fermi level reducing) having negative slopes. A line crossing the x-axis can be interpreted as the defect forming spontaneously at that

Fermi energy because it has no energy penalty to pay. Because the material is effectively unstable at this Fermi energy, the Fermi energy will be pinned at some point before this value. Furthermore if the formation energy of the defect you are using to dope the material (Te_{Sb}^{1+}) goes above the formation energy of a one that compensates the charge of your dopant (V_{Mg}^{2-}), the Fermi energy is pinned somewhere before that crossing[7]. The differences between the Mg rich and Sb rich defect formation energy diagrams comes from the change in chemical potentials required for Mg_3Sb_2 and MgTe to be in equilibrium with either elemental Mg and Sb. This difference is large enough to determine whether Te doping can change the Fermi level enough to degenerately dope the material into the conduction band. The take away from these plots to an experimentalist working in synthesis is there is a better chance of doping Mg_3Sb_2 n-type if there is excess Magnesium in their nominal composition.

1.2.4. Experimentally Controlling Defects

Binary semiconductors such as the III-Vs or II-VIs are often referred to as line compounds because the variance in composition these compounds can tolerate while remaining a single phase is too small to show on a typical binary phase diagram. In reality however, "strict" line compounds do not exist because at elevated temperatures entropy will dictate some level of point defects exist, which will allow for some finite phase width to any material[48;49;50]. One may be tempted to ask if such a small changes in composition can meaningfully affect the properties of a material. It is important to remember that when dealing with semi-conductors very small deviations in composition (ppm levels) can affect carrier concentration and formation energies of point defects.

From a synthetic perspective a range of these single-phase compositions within a line compound may not be accessible due to a number of factors e.g. accuracy of balances, purity of starting material, vapor pressure of materials being reacted, ect. However, any line compound will have two unique compositions available to an experimentalist, on either side of the line.

1.2.4.1. Phase Boundary Mapping. Determining on which side of the line or "phase space" a material resides in is not always a trivial task and can get even more difficult as the number of components in a system increases. One way of determining which phase space a sample resides in is by looking at the impurity phases that exist with powder diffraction or energy dispersive spectroscopy (EDS). However, often experimentalists create samples with nominal composition equal to the phase they are attempting to synthesize leaving any impurity phases below the detection limit of a standard lab x-ray or EDS. While this may allow for a sample to be deemed "pure" it gives no information on the phase space or chemical potential space that material resides in.

Furthermore, if impurity phases are known and the samples is in thermodynamic equilibrium then the Gibb's phase Rule can be used to determine whether the main phase's composition is invariant. If a samples number of phases equal the number of components in the sample any new sample made in this phase space will continue to have the same chemical potentials, defect formation energies, and finally carrier concentrations. Even with no knowledge of defect energies, by mapping various phase spaces around the target single-phase region, an experimentalist can determine the range in which a compound can be doped[7;51]. One should note that changing the nominal composition while still remaining in a multi-phase region can still change samples properties by altering the

amount of its secondary phase created, but the carrier concentration of each constituent phase remains the same.

1.2.4.2. Saturation Annealing. Another option of experimentally controlling defect concentrations in a material is through saturation annealing. Saturation annealing, like phase boundary mapping, is an experimental route for setting the atomic chemical potentials in a material. In saturation annealing, rather than relying on secondary phases within a sample to affect the atomic chemical potentials, an equilibrating medium outside of the sample is used. This has the obvious benefit that secondary phases, which can affect property measurements and are impossible to create in single crystal samples, need not be present in a sample.

In a saturation anneal a sample and equilibrating media are placed in a sealed container and heated to a sufficient temperature that allows for mass transport such that atomic species within the sealed system are in equilibrium in each phase. The sample and equilibrating media being annealed need not be in physical contact with one another as long as a sufficiently high vapor pressure of the atomic species are reached to ensure that sufficient mass transport for equilibrium is reached.

1.3. The Role of Defects in Thermoelectric Materials

Point defects play a large role in the properties of nearly any material. Specifically considering electronic transport, substitutions, interstials, and vacancies in minute quantities (approximately less than 1 atomic percent) can play a significant role in changing a material's Fermi-level and thereby carrier concentration. Tuning a material's carrier concentration has implications in fields relating to semi conductors such as: solid-state

lighting, transparent conducting oxides, photovoltaics, topological insulators, and thermoelectrics. For the purpose of this work I will be referring to minute additions of point defects for the purpose of shifting a materials fermi-level as doping.

In the field of thermoelectrics, tuning a material's carrier concentration is a sometimes difficult, but very important design problem. Its importance lies in the thermoelectric figure of merit zT, which is given by $zT = \alpha^2\sigma T/\kappa$, where α is the seebeck coefficient, σ is the electrical conductivity, κ is the thermal conductivity, and T is temperature. A material's seebeck coefficient decreases with increasing carrier concentration, whereas its electrical conductivity increases with increasing carrier concentration. This makes control over a materials carrier concentration crucial in order to extract its optimum zT [52].

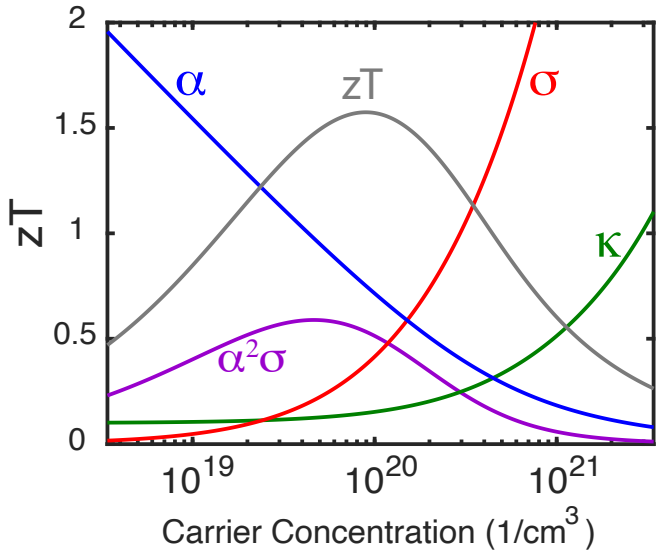

Figure 1.6: Simulated zT, seebeck coefficient (α), electrical conductivity (σ),thermal conductivity (κ), and power factor ($\alpha^2\sigma$) vs carrier concentration for a material where a single parabolic band is involved in transport. Note how the coefficients that make up the numerator of zT respond in opposite ways to changes in carrier concentration.

Point defects can be utilized for more than tuning a materials carrier concentration. When the concentration of point defects is increased to larger levels (approximately greater than one atomic percent), point defects can fundamentally alter a material's bonding and the way it transports heat and electricity. For the purpose of this paper I will be referring to large concentrations of substitutional point defects added for purposes other than shifting a materials fermi-level as alloying.

In order to discuss if a material's properties are helped or hurt by alloying substitutional point defects, it is useful to introduce the materials dimensionless quality factor: $B = \frac{k_B^2}{e}\frac{(2m_e k_B)^{3/2}}{3\pi^2\hbar^3}\frac{\mu_0(\frac{m_s^*}{m_e})^{3/2}}{\kappa_L}T^{5/2}$ in which k_B is boltzmann's constant e is the charge of an electron, m_e is the mass of an electron , $\hbar$ is reduced planck's constant, T is temperature, m_s^* is the seebeck effective mass, μ_0 is the intrinsic mobility, and κ_L is the lattice thermal conductivity. Frequently the term $\mu_0(m_s^*/m_e)^{3/2}$ is referred to as the weighted mobility[53]. A materials quality factor can be thought of as a fermi-level independent form of zT, and can be used to predict a material's zT if its fermi level were set to a different value. In this equation all terms but the weighted mobility $\mu_0(m_s^*/m_e)^{3/2}$ and lattice thermal conductivity κ_L are constants for a given temperature. These two values can be solved given some assumptions (deformation potential scattering, roughly parabolic bands, single band transport) with the experimental inputs of Seebeck coefficient, conductivity, and thermal conductivity.

Alloying has been demonstrated as a practical way to do band engineering in thermoelectrics, which aims to change the bonding and dispersion of electrons in a material to seek more advantageous electronic properties (increase $\mu_0(m_s^*/m_e)^{3/2}$). Additionally, in alloyed materials, scattering times in both electrons and phonons are usually decreased,

as larger concentrations of point defects disrupt the periodic potential, position, and mass of the atoms on the lattice. This means point defects can increase or decrease a material's zT depending upon how the electrical $\mu_0(m_s^*/m_e)^{3/2}$) and thermal (κ_L) properties of this material are affected by alloying.

First principles[54] and empirical models[55] (such as quality factor) can often predict very large zTs in materials, which may be difficult, or even impossible to realize due to native defects in the material that effectively forbid its Fermi-level from going above or below a certain value. For example, David Singh and David Parker had predicted the $CaAl_2Sb_2$ type Zintl compound Mg_3Sb_2 to be a good n-type thermoelectric in 2013[56]. However, experimentalists struggled to dope its Fermi level to desired levels due to charged vacancies on the octahedrally coordinated magnesium site counteracting any elemental substitution elsewhere that could donate an electron[7]. These charge compensating defects, sometimes called killer defects, exist in many materials and limit a material's potential applications as a semiconductor. The secret to eventually doping Mg_3Sb_2 n-type came from engineering and an eventual understanding of these charge-compensating defects[57].

This thesis is structured around the theme of defects in Zintl materials. Chapter 2 and 3 are primarily concerned with different methodologies on controlling aliovalent defects in materials that affect the Fermi-level in a material. In Chapter 2 I discuss the technique of phase boundary mapping and apply it to check for bounds of obtainable carrier concentration in ZnSb. In chapter 3 I discuss the saturation annealing technique for setting atomic chemical potentials in Te doped $Mg_3Sb_{1.5}Bi_{0.5}$, which allows for the creation of large grained material. Chapter 4 is again focused on defects that change the carrier concentration in a $Yb_{14}Mg_{1-x}Al_xSb_{11}$, but instead of focusing on how to methodologically

obtain those defects I show on how changing the experimental carrier concentration can provide insights into the band structure and its effects on transport. Chapter 5 shows how alloying type isovalent defects can be used to alter the band structure in the Zintl solid solution $CaZn_{1-x}Mg_xSb_2$. Finally Chapter 6 looks again at $Mg_3Sb_{1\cdot 5}Bi_{0.5}$, but this time focuses on the scattering effects of substituting isovalent Yb for Mg.

CHAPTER 2

Controlling Defects I: Phase Boundary Mapping Sn Doped ZnSb

This chapter contains content being prepared for submission in a journal. Once accepted permission will be requested.

2.1. Introduction

ZnSb has long been studied as a thermoelectric material with publications dating back to at least the 1950s[58]. While sometimes referred to as an electron poor framework semiconductor due to a crude valence counting of Zn ([Ar]3d104s2) and Sb ([Kr]4d105s25p3) resulting in only 7 valence electrons[59], ZnSb can be explained through Zintl Formalism. When the crystal structure is more closely analyzed it becomes apparent that there exist two antimony sites that share close proximity. Furthermore, the charge density distribution map conducted by Song et al.[59] shows electron density between these two antimony sites indicating the formation of a bond. When this Sb-Sb diamer is considered the formula unit of ZnSb can be rewritten as 2 Zn^{2+} and $[Sb{-}Sb]^{4-}$ to more clearly show balanced valence counting.

In 2011 Böttger et al.[10] studied Cu ($Zn_{1-x}Cu_xSb$) and Sn ($ZnSb_{1-x}Sn_x$) doped ZnSb achieving a maximum carrier concentration of 8×10^{18} ($1/cm^3$) with a zT of 0.3. While this figure of merit wasn't remarkable, this study also performed a single parabolic band analysis of their data indicating a zT = 0.75 at 700 K was theoretically obtainable if the material's p-type carrier concentration was increased to 2×10^{19} ($1/cm^3$). Since this

study, there have been numerous follow up doping studies claiming zT$\geq$ 1[60][61][62][63], though achieving this zT consistently has been a challenge. These studies have claimed different routes to this high zT ranging from: multi-atom doping strategies[64][62], arguing precipitate formation was impacting their materials properties[63][60], or that thin film effects were enhancing the materials thermoelectric performance[61]. While many of these papers focus on the scattering effects these dopants and precipitates have on the properties of their samples, there has been little relatively little discussion on the role carrier concentration is having on their samples, or why in some cases similar processing and strategies have lead to different carrier concentrations and properties in different studies and sometimes within the same study[62][64].

2.2. Method: Phase Boundary Mapping

To better understand the role intrinsic defects play on the carrier concentration of ZnSb we decided to conduct a phase boundary mapping study using a 2015 phase diagram investigation to check the achievable carrier concentration in our material with a single external dopant (Figure 2.1)[8]. While other studies have introduced multi atom doping strategies(e.g. Cu+Zn+Cd¸+Ag doping), we chose only to look only at Sn to limit our experimental variables. Four compositions were chosen that resided within the four 3-phase spaces in equilibrium with ZnSb at 400°C (Fig. 3 and Table 1). Other than choice in nominal composition, the same procedure done by Bottger et al.[10] was performed.

At a fixed temperature and pressure, the existence of three distinct phases present in a three-component sample indicates a sample's atomic chemical potentials are set and

invariant. This means that in any two samples with the same phases present, the concentration and type of defects present in each phase should theoretically be the same. This is not to say that two samples with the same phases present in different amounts will have exactly the same properties, but rather that a sample's composition residing in an invariant point of a phase diagram represents an extremum in atomic chemical potentials. Furthermore, as long as impurity phases remain relatively small in volume fraction compared to the phase of interest, significant changes in a property between two chemical potential extremums are more likely to be attributed to changes in chemical potential rather than from any compositing effect of a secondary phase.

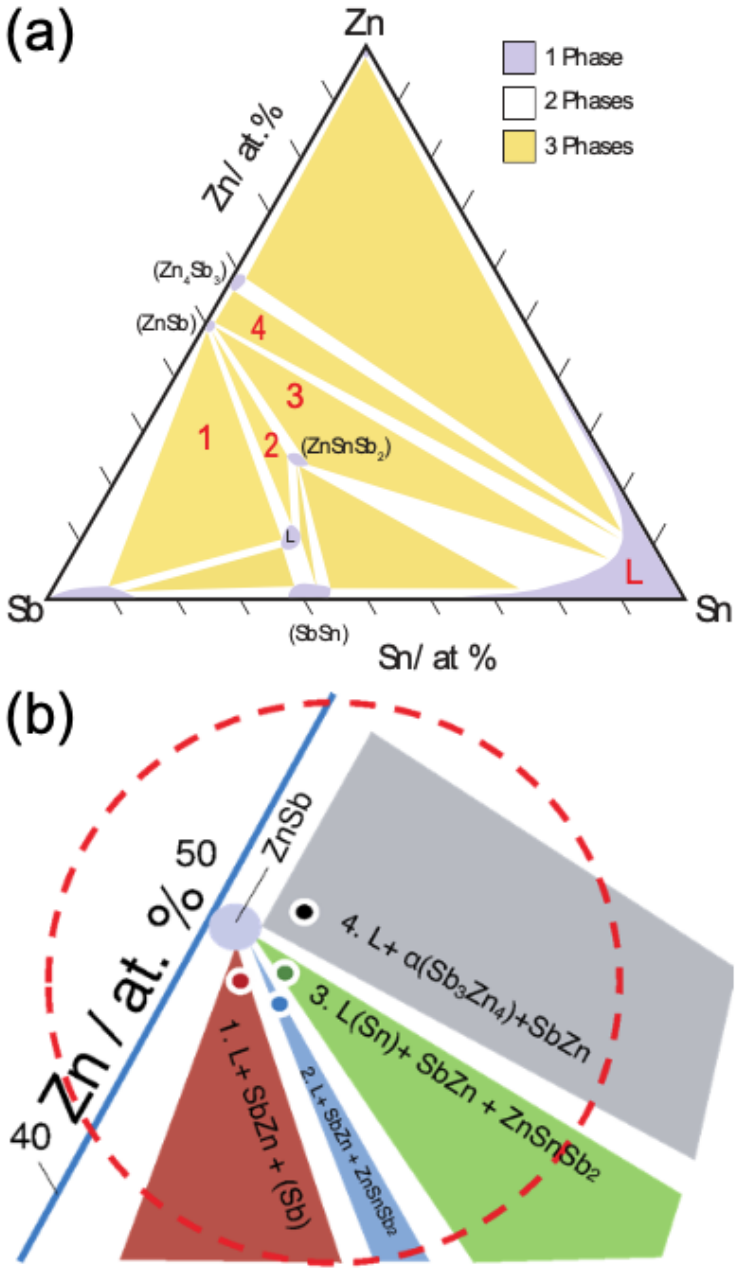

Figure 2.1: Modified from C Wang. et al.[8]. (a) Experimental isothermal phase diagram of the Sn-Zn-Sb system at 400 °C. (b) Zoomed in section of Sn-Zn-Sb isothermal phase diagram showing the nominal stoichiometry compositions made. Additionally, these phase spaces are labeled by numbers going counter clockwise and for the sake of brevity will be referred to by their number.

2.3. Results

X-ray diffraction data in Figure 2.3 verifies the invariance of each sample's chemical potential based on the presence of two impurity phases. Furthermore the nominal compositions chosen produce expected secondary phases based on the phase diagram reported from Wang et al.[8] seen in Table 2.1.

Thermoelectric transport measurements including hall carrier concentration(Figure 2.2), resistivity (Figure 2.4A), Seebeck coefficient(Figure 2.4B), and thermal conductivity (Figure 2.4C) were performed on these samples. The electrical properties of all samples follow expected trends for degenerately doped p-type semiconductor. The Seebeck coefficient increases with increasing temperature indicating transport is dominated by holes, and the resistivity increases linearly indicating phonon scattering is likely dominant. The temperature dependence of thermal conductivity suggests that phonon scattering is the dominant scattering mechanism for lattice thermal conductivity as well. There is a noticeable hysteresis in many of the measured properties of the sample prepared in phase space 4. The hysteresis may be due to cracking, electrical contacts, or fluctuating solubilities of the constituent elements. It has been found that Zn is mobile in Zn-Sb compounds, even at room temperature[65].

While phase spaces 1-3 give carrier concentrations consistent with what Böttger found[10], the sample created in phase space 4 has a carrier concentration of 2.1×10^{19} $1/\mathrm{cm}^3$ approximately where Böttger predicted ideal thermoelectric properties. While instrument limitations brought on by the high vapor pressure of ZnSb prevented investigating temperatures where this zT is found, Shabaldin et al.[9] previously reported a zT$\approx$ 0.9 in ZnSn

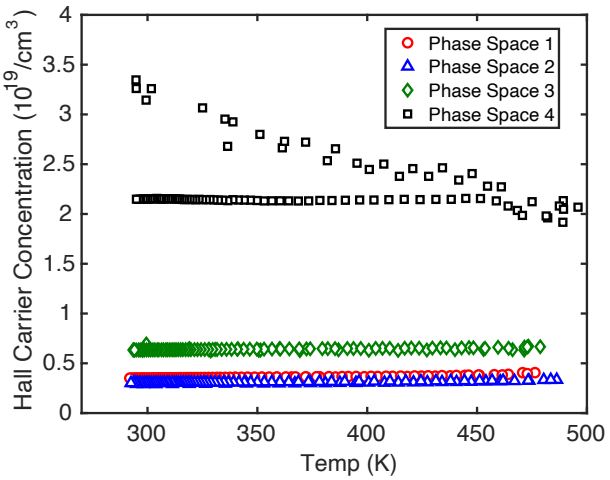

Figure 2.2: Hall Carrier Concentration for ZnSb samples synthesized and analyzed in this study. Notice the significant change in carrier concentration in phase space 4 compared to the other samples.

Table 2.1: Nominal Compositions of samples prepared, and impurity phases that should be present given by the 400 °C isothermal phase diagram.

Phase Space	Nominal Composition	1st Impurity Phase	2nd Impurity Phase
1	$Zn_{0.478}Sb_{0.504}Sn_{0.018}$	Sb	$L \xrightarrow[Quench]{} SnSb$
2	$Zn_{0.470}Sb_{0.497}Sn_{0.033}$	$ZnSnSb_2$	$L \xrightarrow[Quench]{} SnSb$
3	$Zn_{0.480}Sb_{0.490}Sn_{0.030}$	$ZnSnSb_2$	$L \xrightarrow[Quench]{} Sn$
4	$Zn_{0.5}Sb_{0.475}Sn_{0.025}$	Zn_4Sb_3	$L \xrightarrow[Quench]{} Sn$

doped ZnSb with a carrier concentration of 1.5×10^{19} $1/cm^3$. With our phase boundary mapping study we can offer a simple explanation based on atomic concentration and defects that can account for the different results in these studies.

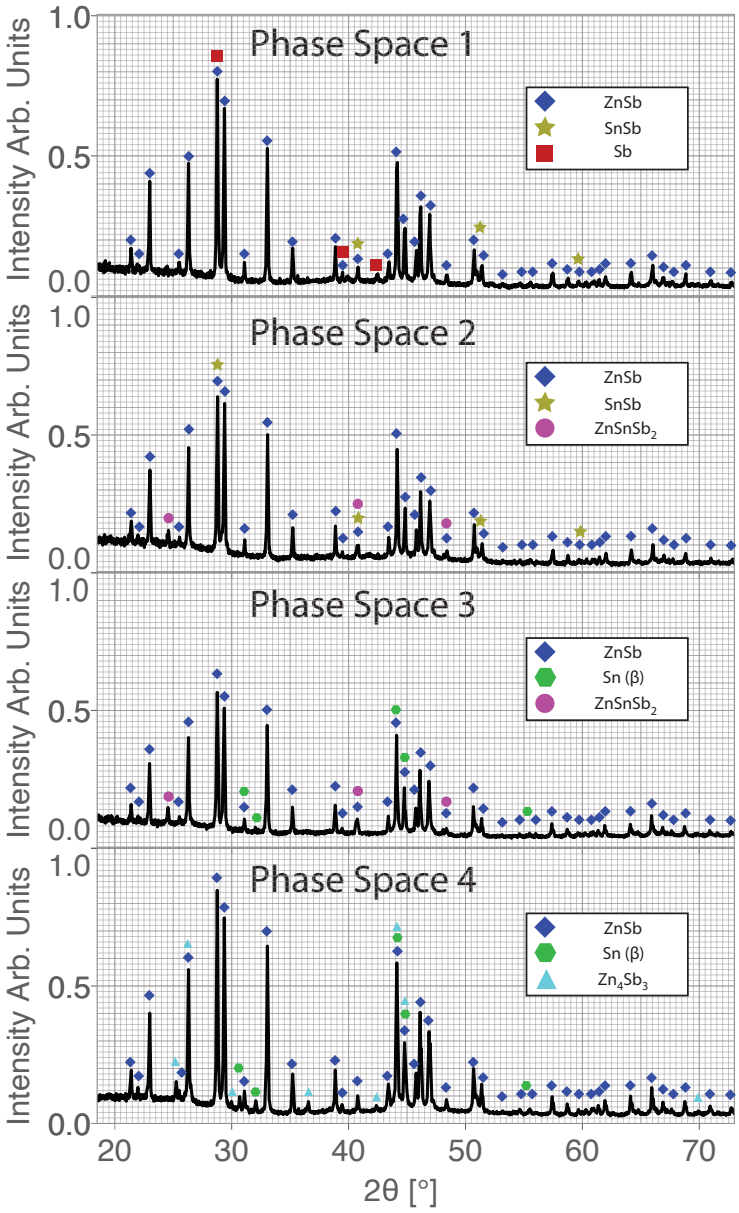

Figure 2.3: . Powder transmission XRD patterns of ZnSb made slightly off stoichiometrically for a phase boundary mapping study. Phase (A) Space 1 with nominal composition $Zn_{0.478}Sb_{0.504}Sn_{0.018}$ (B) Space 2 with nominal composition $Zn_{0.470}Sb_{0.497}Sn_{0.033}$ (C) Space 3 with nominal composition $Zn_{0.480}Sb_{0.490}Sn_{0.030}$ (D) Space 4 with nominal composition $Zn_{0.500}Sb_{0.475}Sn_{0.025}$

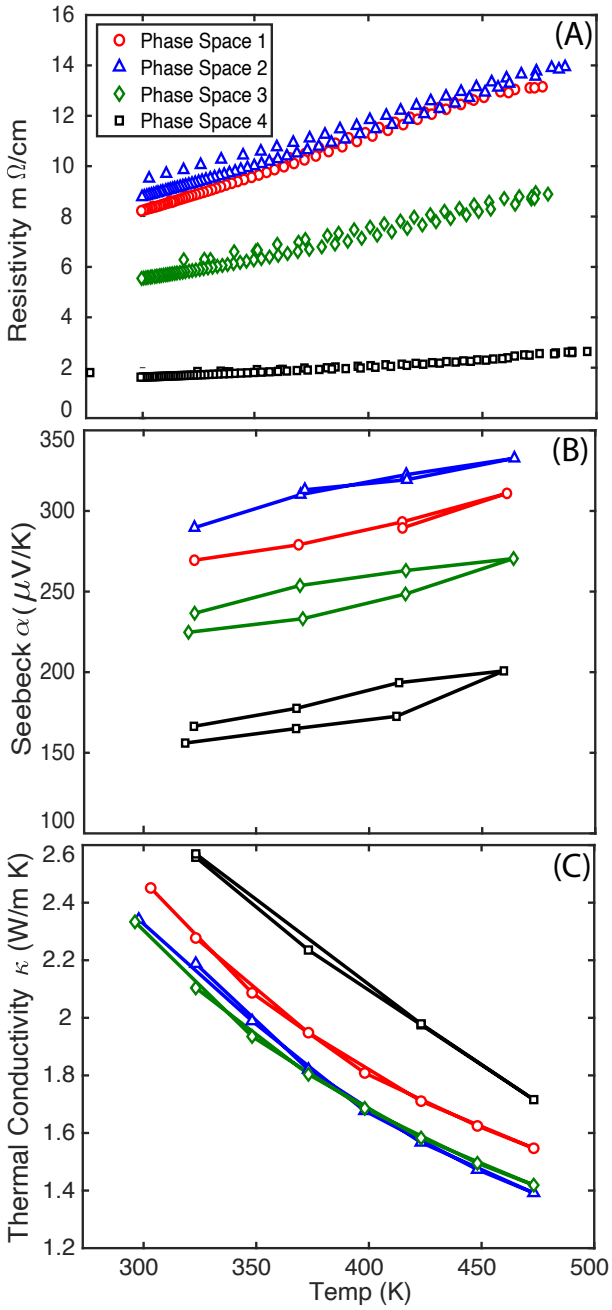

Figure 2.4: Transport data for samples made in a phase boundary mapping study of Sn doped ZnSb. (A) resistivity vs temperature, (B) seebeck coefficient vs temperature, (C) thermal conductivity vs temperature

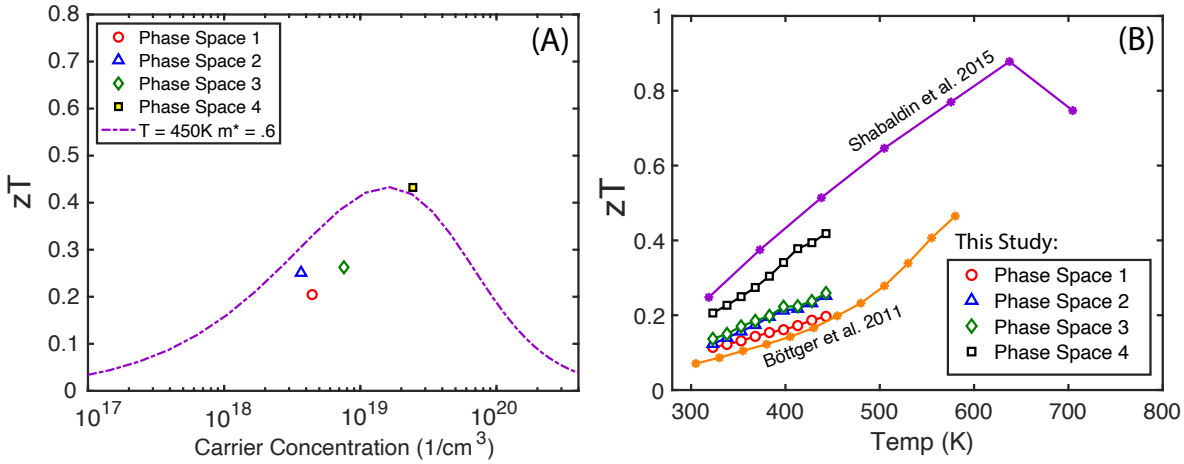

Figure 2.5: (A) zT vs carrier concentration plot. (B) zT vs temperature for samples made here compared to the current highest zT for Sn doped ZnSb made by Shabaldin et al.[9] and the highest zT recorded by Bottger et al.[10] in their study of Sn doped ZnSb. Higher temperatures weren't measured for these samples because ZnSb begins to sublime very rapidly at temperatures above 500 K. By comparing (A) and (B) we can draw conclusions about which phase space each of the studies resided in.

2.4. Discussion

Our phase boundary mapping study shows the phase space 4, where the atomic chemical potentials are highest for Zn and Sn and lowest for Sb, is where the largest carrier concentration is found. The low chemical potential of Sb disqualifies the idea that anion vacancies were contributing to limiting p-type carrier concentration as the Sb vacancy defect formation energy would be lowest in phase space 4. Additionally the high chemical potential of Zn disqualifies the previous claims that Zn vacancies are creating high levels of holes as Zn vacancies would be suppressed in phase space 4 compared to phase space 1, 2, or 3.

A possible reason for phase space 4's high carrier concentration is found by considering the Sn on Sb defect (Sn_{Sb}^{1-}), which would be most energetically favorable when the

chemical potential of Sb is set low and that of Sn is set high. This idea is commensurate with what Shabaldin et al.[9] found in adding excess Zn and Sn lead to increasing carrier concentration, whereas increasing only the Sn content lead to a decreasing carrier concentration. Additionally this phase boundary mapping study suggests Böttger's synthesis procedure lead to a systematic loss of Zn compared to Sb[10]. A plausible explanation for this is Zn has a higher vapor pressure than Sb does. This means samples considered to be nominally ZnSb might in reality be slightly Zn poor, which would make a Sn doped sample reside in either phase space 1 or 2.

A defect formation energy diagram published by L. Bjerg et al.[66] claimed that intrinsic defects would not be largely affected by the phase space a composition resided in, due to the low formation energy of ZnSb. This conclusion when compared to this experimental study highlights the importance in choice of elemental reference energies when calculating defect energies[67].

Figure 2.5A shows the zT vs carrier concentration plot using the material's quality factor and effective mass extracted from the sample residing in phase space 4. This analysis indicates that a sample with $n_H \approx 21/\text{cm}^3$ is optimally doped, in agreement with the previous study[10]. Figure 2.5B compares the zT's of samples in this study to those in Shabaldin et al.[9] and Bottger et al.[10].

2.5. Conclusion

In conclusion, a phase boundary mapping study of Sn doped ZnSb was conducted to probe the experimental limits of atomic chemical potential and determine the dopability in ZnSb. This study determined that Zn Sn rich compositions have the highest carrier

concentration of $n_H = 2 \times 10^19$ 1/cm^3. This result provides insights into previous discrepancies in the literature surrounding the doping limits of Sn doped ZnSb and indicates that a maximum zT near 1 is possible if made in the right phase space.

2.6. Detailed Methods

2.6.1. Sample Preparation

Samples of $Zn_{0.478}Sb_{0.504}Sn_{0.018}$, $Zn_{0.470}Sb_{0.497}Sn_{0.033}$, $Zn_{0.480}Sb_{0.490}Sn_{0.030}$, and $Zn_{0.5}Sb_{0.475}Sn_{0.025}$ were loaded in to evacuated quartz ampules heated to 800°C in a furnace for 24 hours then quenched in water. Samples were then ball milled for 1 hour (SPEX 8000 Series Mixer/Mill) under Ar atmosphere to pulverize the material. Densification was carried out in an induction heated rapid hot-press [68] under a flowing argon atmosphere within a $\frac{1}{2}$ in diameter high-density graphite die (POCO) by hot pressing at 45 MPa at 350°C for 1 hour. Densified pellets were then loaded into evacuated quartz ampules and annealed for 1 week at 400 °C and then water quenched.

2.6.2. Sample Characterization

X-ray diffraction was performed on polished pellets using a STOE STADI MP with pure Cu Kα 1 radiation in reflection geometry. Densities of samples were measured geometrically and then confirmed with the Archimedes Principle. Resistivity and Hall coefficients were measured concurrently using a van der Pauw technique with pressure-assisted molybdenum contacts equipped with a 2T magnet [18]. Thermal diffusivity measurements were taken with a Netzsch LFA 457 under purged flowing argon, and the thermal conductivity was calculated using heat capacity using Dulong petit. Seebeck coefficient were

measured under dynamic high vacuum with a homebuilt system using Chromel-Nb thermocouples[17]. All samples were investigated in pellet form with Seebeck and thermal diffusivity measured out of plane and resistivity and Hall coefficient being measured in the in-plane direction.

CHAPTER 3

Controlling Defects II: Saturation Annealing Te Doped $Mg_3Sb_{1.5}Bi_{0.5}$

(This chapter contains content reproduced with permission from Advanced Material, DOI: 10.1002/adma.201902337.)

3.1. Introduction

Recently, n-type Mg_3Sb_2-based compounds were discovered with a promising peak $zT \approx 1.6$ at 700 K spurring great interests in related compounds[57;13;12]. However, low zT due to the grain boundary scattering at low temperature (300 K to 500 K) not only makes the material uncompetitive at low temperature but also reduces its performance at high temperatures[16]. Based on a previous study[16], it was estimated room for >60% improvement of zT at room temperature if the effects of grain boundaries were entirely eliminated. While hot-pressing at elevated temperatures (*e.g.* 800°C) has been demonstrated to increase the average grain size[14] and therefore zT, further grain growth through long-term heat treatment has been limited as the loss of Mg prohibits the n-type dopability of the compounds[7].

In this work, further grain growth is achieved through a novel annealing procedure in the presence of Mg-vapor (Fig. 3.2) which preserves the heavily doped n-type properties of the materials. Mg-vapor annealing can significantly improve the performance of a sample at low temperature by increasing its average grain size. In particular, a 800°C-sintered

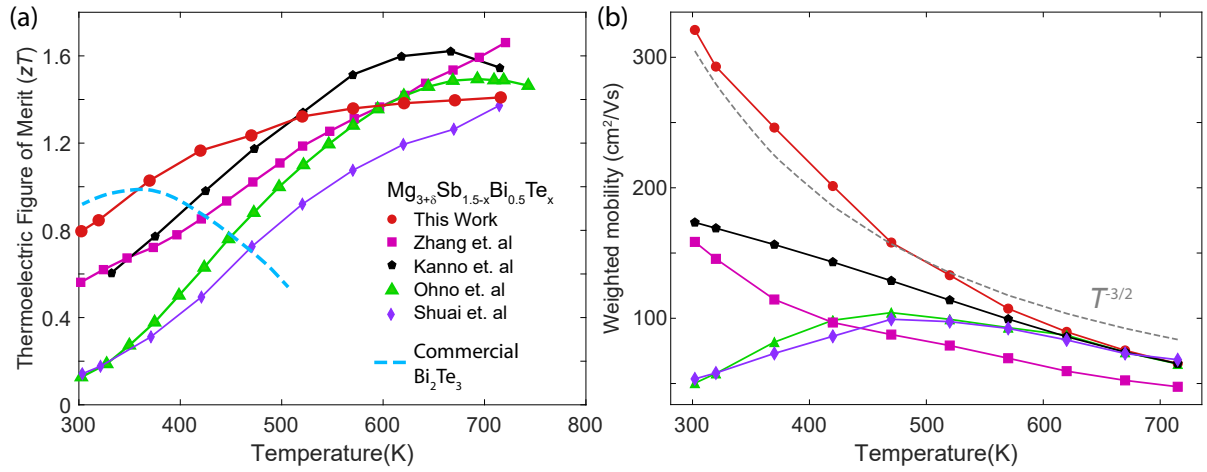

Figure 3.1: (a) Temperature dependent zT and (b) Weighted mobility[11] (calculated using electrical conductivity and Seebeck coefficient) of $Mg_{3+\delta}Sb_{1.49}Bi_{0.5}Te_{0.01}$ annealed for 65 hours in Mg vapor in comparison to similar compositions found in literature[12;13;14;7] and n-type Bi_2Te_3[15]. Note that the electrical conductivity and Seebeck coefficients used here are all measured in a ZEM-3 for the purpose of comparison (see Figure. 3.8).

Te-doped $Mg_{3+\delta}Sb_{1.5}Bi_{0.5}$ reaches a $zT \approx 0.8$ at 300 K after long-term annealing (*e.g.* $\approx$ 65 hours, see Fig. 3.1(a)) which is comparable to commercial thermoelectric material used at room temperature (n-type Se-alloyed Bi_2Te_3). This high zT is due to the sample's high weighted mobility (Fig. 3.1(b)), which characterizes its potential power factor[11]. In addition, the Hall mobility reaches 170 cm^2/Vs (Figure. 3.7), which is the highest among all reported data for n-type $Mg_3Sb_{1.5}Bi_{0.5}$.

Table 3.1: Hall mobility μ_H at 300 K of the annealed 800°C-sintered sample and data from the literature.

Ref.	Kanno[14]	Zhang[12]	Ohno[7]&Shuai[13]	This work
$\mu_H(cm^2/Vs)$	109	45	$\approx$20	170

3.2. Method: Magnesium-vapor Anneal

Annealing has long been a strategy for improving the electrical mobility in materials, which can be due to several different mechanisms: reduction of defects (vacancy, interstitial, dislocation), grain growth, and grain boundary modification. etc.[69;70;71;72;73]. Conventional annealing of thermoelectric materials is typically done in a vacuum sealed fused-quartz container to prevent oxidation. For n-type Mg_3Sb_2, however, this method is not applicable due to the reaction between Mg and quartz to form Magnesium silicates or MgO. Even the use of an open crucible (*e.g.* metal foil or vitreous carbon – Al_2O_3 will also react with Mg) will not suffice because of the significant vapor pressure of Mg which will quickly react with SiO_2. The loss of Mg promotes the formation of Mg vacancies V_{Mg}^{2-}, which serves as electron killers and effectively eliminates the n-type charge carriers in the samples[7].

In this work, we develop an unconventional technique (Fig. 3.2) which preserves the n-type properties of Mg_3Sb_2-based compounds throughout the annealing process. In this technique , hot-pressed pellets are placed into a MgO crucible together with Mg turnings (elemental Mg). MgO was choosen for the crucible because it has no sub-oxides and therefore wouldn't react with the sample, Mg vapor or Mg metal. The crucible was then loaded into a graphite susceptor which was heated up to the target temperature via an induction heater. Due to the fact Mg forms no stable carbides, a Mg vapor pressure can be maintained inside the crucible and in equilibrium with the annealing sample.

The Mg vapor present as a secondary phase during the Mg-vapor anneal, is necessary to maintain high n-type carrier concentration in Mg_3Sb_2-based materials. Without the

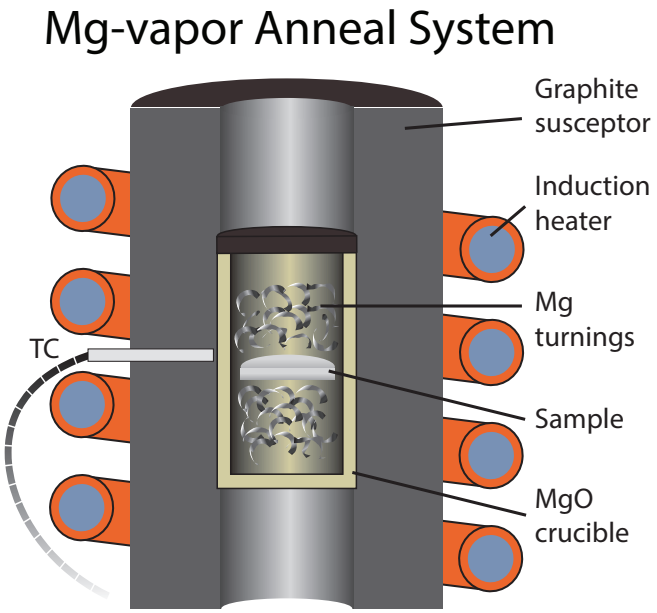

Figure 3.2: Schematic of the Mg-vapor annealing system. The sample pellet and Mg turnings are put in a MgO crucible. The crucible is loaded into a graphite susceptor, which is heated up to the target temperature (*e.g.* 600°C) via an induction heater.

presence of Mg vapor during a 600°C anneal, degenerate n-type samples become non-degenerate p-type. A similar effect has been observed in our previous work[74], in which we showed the depletion of n-type charge carriers in Te-doped $Mg_{3+\delta}Sb_{1.5}Bi_{0.5}$ over time when the sample was held under dynamic vacuum at 450°C. The effect was attributed to the preferential sublimation of Mg, which lead to the creation of electron neutralizing Mg vacancy point defects.

When these intrinsic samples are then annealed in the presence of Mg vapor, their degenerate n-type charge carrier concentration returns, confirming that preferential sublimation of Mg is the cause of the aforementioned reduction of carrier concentration. Additionally, Te-doped samples that are intentionally made Mg deficient and non-degenerate

(low charge carrier concentration) can even be put into a Mg-excess degenerate state via a Mg vapor anneal (*e.g.* 1 hour at 600°C).

Fig. 3.3 shows the effect of short-term Mg-vapor anneal on the Seebeck coefficient. The Te-doped Mg_3Sb_2 sample was made nominally slightly Sb-excess/Mg-poor (*i.e.* $Mg_{3-\delta}Sb_2$) and therefore was p-type initially[7]. The sample was annealed in Mg vapor for 1 hour and became degenerately doped n-type afterward. This result demonstrates that a Mg-vapor anneal provides an environment that reduces the Mg vacancies concentration and favors the n-type properties of Mg_3Sb_2-based compounds. This shows excess Mg in a sample's nominal composition is not necessary to achieve n-type conduction as long as Mg vacancies are controlled via some other method.

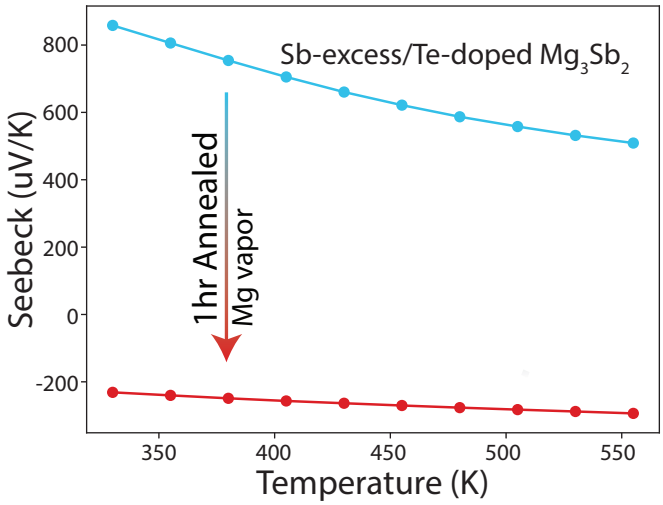

Figure 3.3: Transition of Te-doped Mg_3Sb_2 from the p-type, non-degenerate (blue curve) to n-type, degenerate (red curve) semiconductor after Mg-vapor anneal.

3.3. Results

3.3.1. Transport Properties

A significant enhancement of electrical conductivity at low temperatures was discovered in the $Mg_{3+\delta}Sb_{1.49}Bi_{0.5}Te_{0.01}$ samples after long-term Mg-vapor anneal (Fig. 4.1(a)). Pellets with different initial grain sizes were prepared via different sintering conditions (*i.e.* at 600°C for 1 hour and at 800°C for 20 minutes). In each condition, a pair of pellets were pressed at the same time in the same instrument, with one as the control sample and the other for annealing at 600°C for 65 hours. For both conditions, annealed samples show higher electrical conductivities compared to the un-annealed control ones.

In particular, the conductivity of the 800°C-sintered sample follows a $T^{-3/2}$-trend, which indicates a phonon (deformation potential) scattering mechanism dominating even at room temperature. The unchanged Seebeck (Fig. 4.1(b)) suggests that the Fermi level of the sample is unaltered, and therefore the improvement of conductivity should be attributed to the reduction of detrimental grain boundary scattering. Due to the phonon (deformation potential) scattering temperature dependence of mobility (Fig. 3.1(b)), additional annealing would likely not continue to improve the electrical mobility of our 800°C-sintered and annealed sample.

3.3.2. Grain Size Measurement

Electronically, the region near a grain boundary can be more resistive than the bulk due to the disorder and off-stoichiometry at the boundary[75;76]. Decreasing the density of grain boundaries, as well as reducing their resistance are two potential explanations for the improvement of low temperature electrical conductivity shown in Fig. 4.1(a).

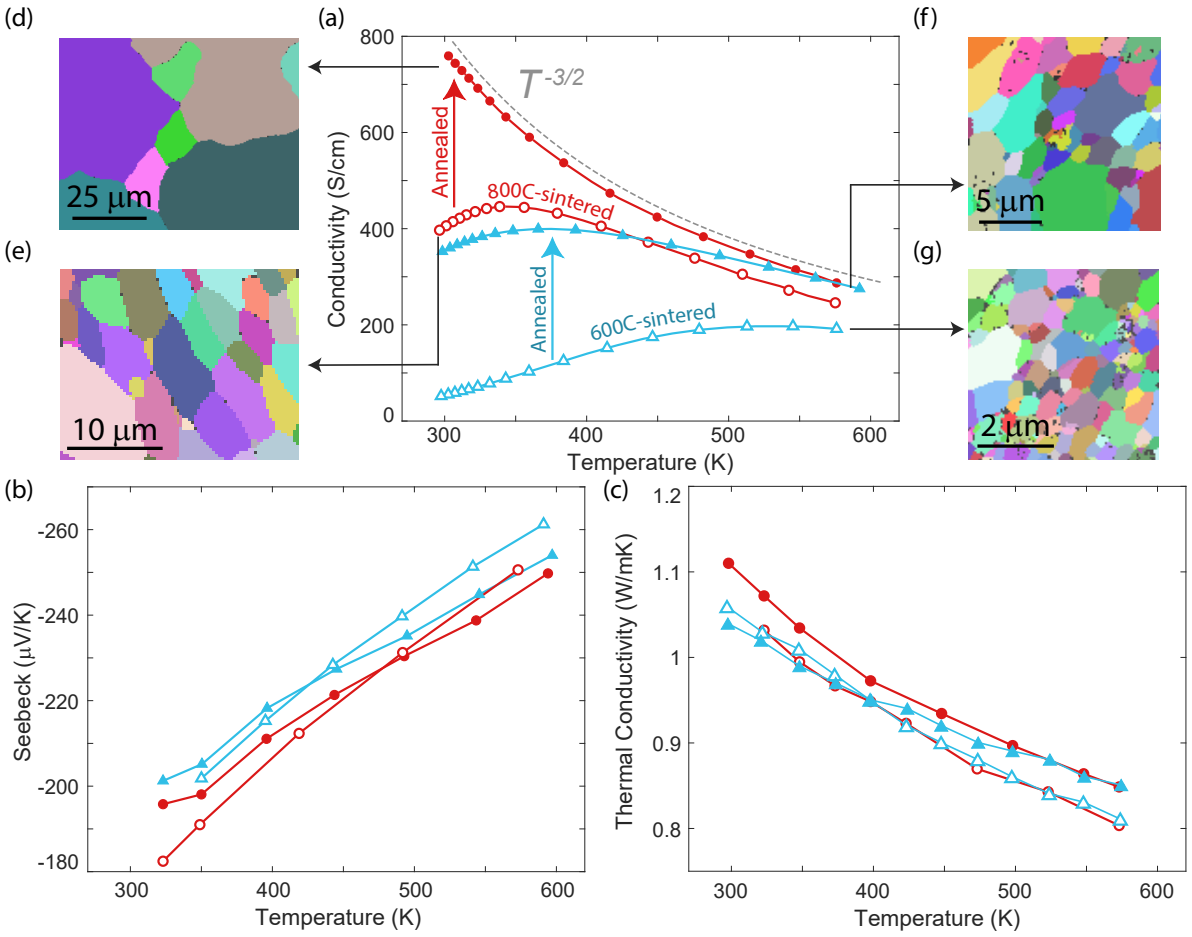

Figure 3.4: (a)-(c) Transport properties of the annealed (solid markers) and control (open markers) $Mg_{3+\delta}Sb_{1.49}Bi_{0.5}Te_{0.01}$ Both the 800°C-sintered (red-circles) and the 600°C-sintered samples(blue-triangles) show an improved conductivity after 65-hour Mg-vapor anneal. The annealed 800°C-sintered sample (red closed circle) shows a $T^{-3/2}$-trend as predicted by phonon (deformation potential) scattering. The negligible change of Seebeck coefficient and thermal conductivity is consistent with our previous study assuming a grain boundary scattering[16]. (d)-(g) Corresponding EBSD maps of the samples. Grain growth observed in the annealed samples suggests the improved conductivity in (a) is due to the reduction of grain-boundary density.

Experimentally, the average grain sizes before and after anneal can be measured via electron backscatter diffraction (EBSD).

Measurable grain growth in the annealed samples can be seen through the comparison of EBSD maps (Fig. 4.1(d)-(h)). The grain sizes of the un-annealed samples (*i.e.* $< 1\ \mu m$ for the 600°C-sintered, and $\approx 10\ \mu m$ for the 800°C sintered) is consistent with the values reported in the literature[14], whereas the annealed samples have grain size significantly larger than the un-annealed counterparts (*i.e.* $\approx 5\ \mu m$ for the 600°C-sintered, and $>$ 30 μm for the 800°C sintered).

3.4. Discussion

3.4.1. Implication of charge transport

The annealed samples' enhanced electrical conductivity and unchanged Seebeck coefficient after grain growth supports the conclusion that grain boundary scattering is significant in Mg_3Sb_2-based materials[16]. Because a sample's measured Seebeck coefficient is dominated by its bulk electrical properties (*e.g.* density-of-states and Fermi level)[11], when the transport mechanism of the bulk grains changes, the Seebeck coefficient should also change correspondingly. Based on this argument, other hypotheses for why the electrical conductivity increses with temperature in some n-type Mg_3Sb_2, such as point-defect scattering or ionized-impurity scattering[13;77], would predict a change of bulk properties and therefore a change of Seebeck coefficient. In addition, these hypotheses do not explain the enhanced performance witnessed in samples with large grain sizes[14]. We therefore conclude that the reduction in low-temperature zT observed must be due to the highly-resistive grain boundaries.

Table 3.2: Eutectic melting temperatures between Mg - Mg_3Sb_2 [1;2;3;4] and Mg - Mg_3Bi_2 [5;2;3], and the pseudo-eutectic melting temperature between Mg - $Mg_3Sb_{1.5}Bi_{0.5}$. The pseudo-eutectic initial melting temperature of the alloyed compound was measured through differential thermal analysis in this work (Figure 3.6).

$Mg_3(Sb_{1-x}Bi_x)_2$	x=0	0.25	0.5	0.7	1
T_{Eut}(°C)	629 ± 2	602 ± 5	584 ± 5	570 ± 5	552 ± 2

3.4.2. Hypothesis of the Grain-growth Mechanism

The grain growth witnessed in annealed samples could be associated with a pseudo-eutectic liquid that forms at the grain boundary, and dramatically increases atomic diffusion during annealing.[78] This liquid is called pseudo-eutectic (like in the Al - Mg_2Si pseudo-binary[79;80]) instead of eutectic because it does not meet the strict criteria of being a single point in ternary space where four phases are in equilibrium at a single temperature.[81;82] Furthermore, the term pseudo-eutectic is used to differentiate the liquid that we witness from a congruently melted liquid formed entirely from the $Mg_3Sb_{1.5}Bi_{0.5}$ alloy, which would only occur at a much higher temperature.

The pseudo-eutectic temperature is assumed to be the temperature of initial melting measured by DTA as, and changes with Sb/Bi ratio as shown in Table 3.2. The Mg - Mg_3Sb_2 eutectic has been reported at 88 at.%[4] and 90 at.%[2] of Mg. The Mg - Mg_3Bi_2 eutectic has been reported at 87 at.%[5], 82 at.%[2] and 86 at.%[4] of Mg. Therefore, we estimate the pseudo-eutectic composition should be found at approximately at 85 ± 5 at.% of Mg. The Te-doped $Mg_{3+\delta}Sb_{1.5}Bi_{0.5}$ samples presented here are annealed with extra Mg at a temperature where there is likely to be some liquid phase, which would increase grain growth.[78] A quick non-equilibrium re-solidification of this melt should lead

to some compositional segregation of the Sb/Bi ratios in solid-solution, which is called coring[81;82].

3.5. Conclusion

In conclusion, we demonstrate an unconventional method for annealing n-type Mg_3Sb_2-based compounds in Mg vapor which preserves their n-type properties during grain growth. We observed that long-term annealing results in a significant enhancement in the electron mobility, which is attributed to a reduction in grain boundary scattering as the grain size increased. Adding this annealing processing step to $Mg_{3+\delta}Sb_{1.49}Bi_{0.5}Te_{0.01}$ material results in a $zT = 0.8$ at 300 K allowing it to compete with commercial n-type thermoelectric materials.

3.6. Detailed Methods

3.6.1. Sample preparation

We sealed magnesium turnings (99.98 %, Alfa Aesar), antimony shots (99.9999 %, 5N Plus), and Te shot (99.999 %, 5N Plus) into stainless-steel vials according to stoichemetric ratios in an argon-filled glove box.The nominal composition we used for all ball milled samples in this study was $Mg_{3.01}Sb_{1.49}Bi_{0.5}Te_{0.01}$. Elements were mechanically alloyed by high energy-ball milling with a high-energy mill (SPEX 8000D) for two hours. The processed powder was loaded into a graphite die with half inch diameter and pressed by an induction heating rapid hot press[83] for 60 minutes at 873 K or 20 minutes at 1073 K and 45 MPa under argon gas flow.

3.6.2. Annealing process

Hot-pressed pellets were placed into a magnesium oxide crucible (25 mm diameter, 25 mm height). Magnesium turnings (99.98 %, Alfa Aesar) are added such that both sides of the pellet are in contact with Mg turnings. The crucible was loaded into a graphite die and covered by a piece of graphite foil and graphite spacer to create a quasi-isolating environment for the pellet. The graphite die was heated up by a induction heater to 873 K under argon gas flow.

3.6.3. Measurement of crystal grain sizes

Electron backscattering diffraction (EBSD) maps were obtained using a scanning electron microscope (Quanta650FEG) equipped with a detector (Oxford Instruments Nordlys).

3.6.4. X-Ray Diffraction Measurement

X-Ray diffraction on the pelletized was carried out on a Stoe STADI-MP in reflection geometry using pure Cu K1α radation. From XRD There appears to be no detectable impurity phase in any of the samples tested for this study. The narrowing of peaks in the annealed samples is likely due to micro-strain being reduced in the annealed samples.

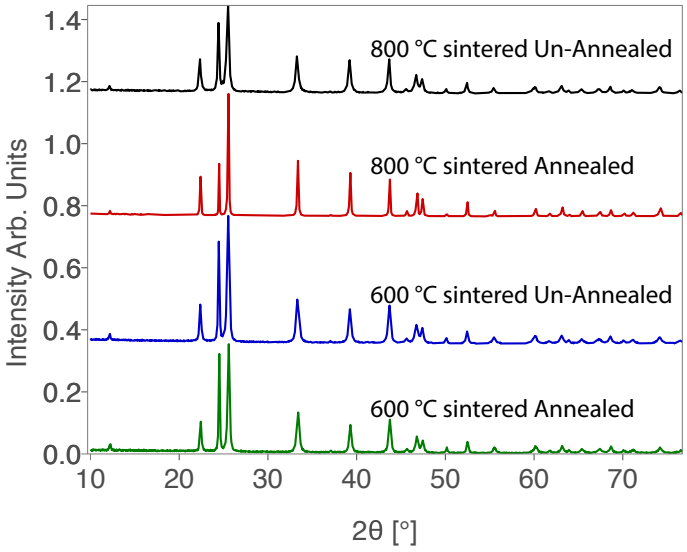

Figure 3.5: Cu K1α x-ray diffraction in reflection geometry of pelletized samples sythesized for this study. All samples had a composition of $Mg_{3.01}Sb_{1.49}Bi_{0.5}Te_{0.01}$, but underwent different processing steps.

3.6.5. Differential thermal analysis

Differential Thermal Analysis (DTA) was carried out in a Netzch Jupiter F3. A balled milled samples of $Mg_{0.75}(Sb_{0.75}Bi_{0.25})_{.25}$ was sealed in a carbon coated quartz vials and ramped to 750 °C at a rate of 10 °C/min. The sample was then cooled at a rate of 10 ° to room temperature. The pseudo-eutectic onset of melting temperature between Mg & $Mg_3Sb_{1.5}Bi_{0.5}$ was measured through differential thermal analysis (DTA). Fig.3.6 shows the onset of melting in ball milled powder with composition $Mg_{0.75}(Sb_{0.75}Bi_{0.25})_{0.25}$.

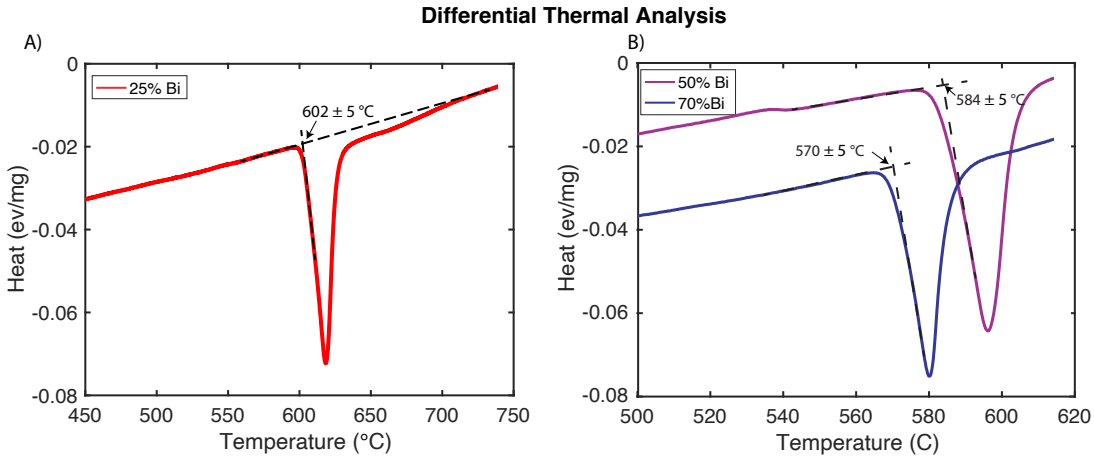

Figure 3.6: Differential Thermal Analysis data for ball milled powder of $Mg_{0.75}(Sb_{0.75}Bi_{0.25})_{0.25}$, $Mg_{0.75}(Sb_{0.5}Bi_{0.5})_{0.25}$ and $Mg_{0.75}(Sb_{0.3}Bi_{0.7})_{0.25}$ during heating.

3.6.6. Measurements of transport properties

Electrical and thermal transport properties were measured from 323 to 573 K. The electrical resistivity and Hall coefficient measurements were determined using the 4-point probe Van der Pauw technique with a 0.8 T magnetic field under high vacuum[18]. The Seebeck coefficients of the samples were obtained using chromel-Nb thermocouples by applying a temperature gradient across the sample to oscillate between ±5 K[17]. Thermal conductivity was calculated from the relation $\kappa = DdC_p$, where D is the thermal diffusivity measured with a Netzsch LFA 457 laser flash apparatus, d is the geometrical density of the material (see Table. 3.3) and C_p is the heat capacity at constant pressure. C_p the compounds were calculated via the polynomial equation proposed by Agne *et al.*[84].

For the purpose of comparison, we measured the electrical transport properties (*i.e.* conductivity and Seebeck coefficient) on an ULVAC ZEM-3, as shown in Fig. 3.8 in the

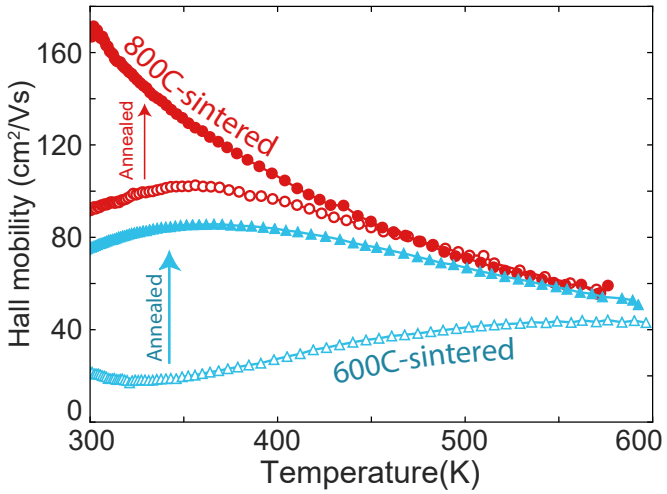

Figure 3.7: Hall mobility of the annealed (red color) and control (blue color) $Mg_{3+\delta}Sb_{1.5}Bi_{0.5}Te_{0.01}$ Both the 800°C-sintered (empty circle marker) and the 600°C-sintered samples show an improved conductivity after 65-hour Mg-vapor anneal.

SI. ZEM data is used for to compare zT's and weighted mobilities of our samples and literature (Fig. 3.1).

Table 3.3: Geometrical density d of the samples sintered at different temperatures with and without annealing. Theoretical estimate of the density of $Mg_3Sb_{1.5}Bi_{0.5}$ is calculated from densities of the two end members assuming a linear relation(*i.e.* 4.02 g/cm^3 for Mg_3Sb_2 and 5.84 g/cm^3 for Mg_3Bi_2, data from the Inorganic Crystal Structure Database).

T_{sinter}	600°C		800°C		Theo.
d (g/cm^3)	pristine	anneal	pristine	anneal	≈4.5
	4.51	4.45	4.49	4.48	

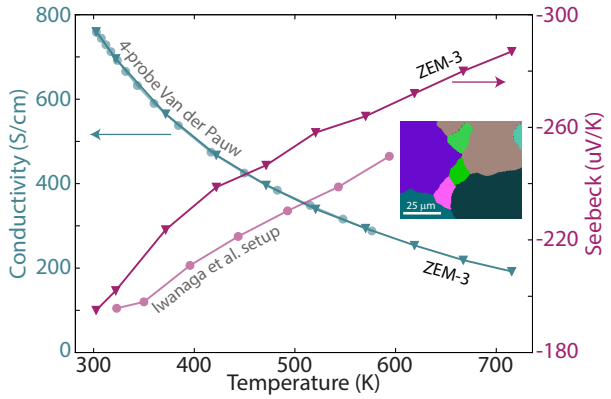

Figure 3.8: Electrical conductivity (cyan, left axis) and Seebeck coefficient (purple, right axis) of the annealed 800°C-sintered sample. The conductivity from ZEM-3 (cyan triangles) shows similar trend as our measured through Van der Pauw measurement (cyan circles), whereas the Seebeck coefficient from ZEM-3 (purple triangles) is larger than the measurement setup designed by Iwanaga et al.[17] at high temperatures, which may be due to the cold-finger effect[18].

CHAPTER 4

Using Defects to Probe a Band Structure: $Yb_{14}Mg_{1-x}Al_xSb_{11}$

This chapter contains content being prepared for submission in a journal. Once accepted permission will be requested.

4.1. Introduction

$Yb_{14}MnSb_{11}$ has received much attention since the thermoelectric properties were first reported because of a high thermoelectric figure of merit (zT) at high temperatures (800 – 1273 K).[52;85;86;87]. After synthetic optimization, the zT has become 300 % larger than NASA's legacy p-type Si1-xGex (x 0.5) material employed in radioisotope thermoelectric generators for space missions (RTG).[88;85;86]. With the recent increase in efficiency of $Pr_{3-x}Te_4$, the high temperature n-type material, improving the efficiency of this high temperature p-type material further becomes imperative for an overall efficient RTG.[89] Recently, the thermoelectric properties of the isostructural $Yb_{14}MgSb_{11}$ have been shown to have a higher average zT from 800 – 1273 K without the detrimental increase to electrical resistivity from the spin-disorder arising from Mn.[90] Improving the zT of $Yb_{14}MSb_{11}$ type materials can reduce the cost of RTGs and allow larger payloads on future NASA missions. The complex unit cell (Figure 1) of $Yb_{14}MnSb_{11}$ can be described as consisting of Yb cations, $MnSb_4$ isolated tetrahedra, Sb_3 linear units and isolated Sb anions which lead to an ultra-low thermal conductivity that plays a role in the realization of a large zT.

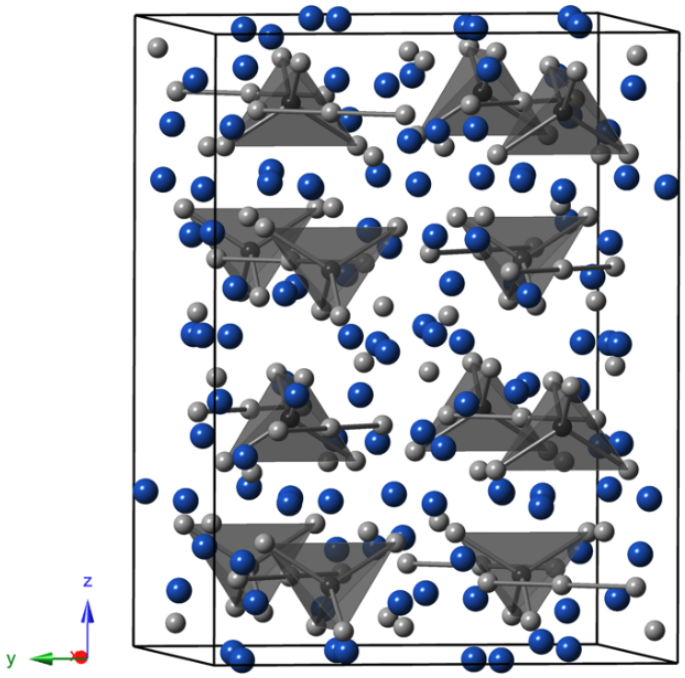

Figure 4.1: The unit cell of $A_{14}MPn_{11}$ (A = Yb; M = Mg; Pn = Sb). A atoms are indicated by blue spheres, MPn_4 are indicated by dark grey tetrahedra, Sb atoms are grey, and Sb_3 linear units are shown as bonded grey atoms.

Experimentalists often use a single parabolic band model (SPB, effective mass model) [91;11] to predict and improve the thermoelectric transport properties of a material. Seebeck, electrical conductivity, and Hall effect data are used to calculate a material's effective mass m* (Seebeck derived DOS (density-of-states) mass), Hall mobility μ_H, and charge carrier concentration n_H as if the electron transport was coming from a single parabolic band. SPB analysis has guided the optimized doping of half-Heuslers ($Hf_{0.65}Zr_{0.35}Ni_{1-z}Pt_zSn_{0.98}Sb_{0.02}$), clathrates ($Ba_8Ga_{16}Ge_{30}$), and $Mo_3Sb_{7-x}Te_x$ [92;93;94;95] However, unexpected changes in the band structure and scattering with doping can lead to changes in the experimentally calculated m*, which can point out deviations from

SPB or simple phonon scattering. Many well-known thermoelectric systems such as: ($Bi_{2-x}Sb_xTe_3$[96] ,$Bi_2Te_{3-x}Se_x$[97], $PbTe_{1-x}Se_x$[98] , $La_{3-x}Te_4$[99], $CoSb_3$[100], $Mg_2Si_{1-x}Sn_x$[101]) have multiple electronic bands that contribute to electron transport which were discovered by noticing systematic changes in DOS m* with alloying or doping.

SPB analysis has been used as a method for improving $A_{14}MPn_{14}$ (A = alkaline earth, Yb, Eu; M = Mn, Mg, Zn; Pn = group 15) materials with mixed results[102]. In a study detailing the $Yb_{14}Mn_{1-x}Al_xSb_{11}$ solid solution, the slope of the samples' Seebeck coefficients changed as expected from a constant m* as the carrier concentration was altered[19]. However, this study could not explain why the Seebeck coefficient of differently doped samples appear to converge near room temperature instead of the expected 0 K for a SPB semiconductor with constant m*. Hu et al.[87] Hu, 2019 277 and Kunz Wille et al.[103] have also shown the experimental DOS effective mass of $A_{14}MPn_{11}$ generally increases with increasing temperature suggesting a deviation from SPB.

Also anomalous, the thermal conductivity of $Yb_{14}MnSb_{11}$[87], $Yb_{14}MgSb_{11}$[104], $Sr_{14}MgSb_{11}$[105], and $Eu_{14}MgSb_{11}$[105] and other doped compositions of $Yb_{14}MnSb_{11}$ have an unexplained increase from 300 to 600 K. At 300 K, $Yb_{14}MnSb_{11}$ is above its Debye temperature[106], so the lattice thermal conductivity is expected to decrease proportionally as 1/T if Umklapp scattering dominates phonon transport, or temperature independent if diffuson[107] dominated. This would imply the increase must come from the electronic portion of thermal conductivity, yet an estimation of the electronic thermal conductivity results in a decreasing trend with increasing temperature[86;104;105;108] . A similar low temperature increase in thermal conductivity is also unexplained in $RE_{3-x}Te_4$ (RE = Nd, La)[109], SnTe[110], Ag_9AlSe_6[111], and Eu_9CdSb_9[112].

Herein using a combination of expiramental and computaional methods the abnormal transport behavior in $Yb_{14}MnSb_{11}$ type materials is studied. Experimentally $Yb_{14}MgSb_{11}$ was chosen to study over $Yb_{14}MnSb_{11}$ as the former compound lacks spin disorder scattering, thus reducing an external variable when analyzing its transport. As shown in section 4.2.1, the band structure near the valence band maximum of $Yb_{14}MgSb_{11}$ and $Yb_{14}AlSb_{11}$ do not change substantially other than the placement of the material's Fermi-level with the aliovalent defect Mg_{Al}^{1+}. This makes studying the transport of the $Yb_{14}Mg_{1-x}Al_xSb_{11}$ solid solution an experimental way to probe the band structure of $Yb_{14}MgSb_{11}$ at various Fermi-levels, which can provide insights into the material's anomalous temperature dependency. Using experimental and computational data, we build a three-band model, composed of two valence bands and one conduction band, that attributes the anomalous transport behavior in $Yb_{14}Mg_{1-x}Al_xSb_{11}$ to a highly degenerate secondary band and show the carrier concentration dependence on zT is opposite of what SPB predicts.

4.2. Results and Discussion

4.2.1. DFT Band Structures

The computed band structures of $Yb_{14}MgSb_{11}$ and $Yb_{14}AlSb_{11}$ present remarkably similar features at the level of the valence bands involved in transport Figure 4.2 (AB). In both compounds, the valence band maximum (VBM) is at Gamma (Γ) which is singly degenerate (Nv = 1). Both band diagrams display additional conducting states that are past the initial valence band at Γ with the energy offset (E_{offset}) between the VBM and the next valence band (VB2) and which are very much alike in the two compounds ($E_{offset,Mg}$ = 0.315 eV, $E_{offset,Al}$ = 0.295 eV,) which is stylized in Figure 4.2 (C). The corresponding

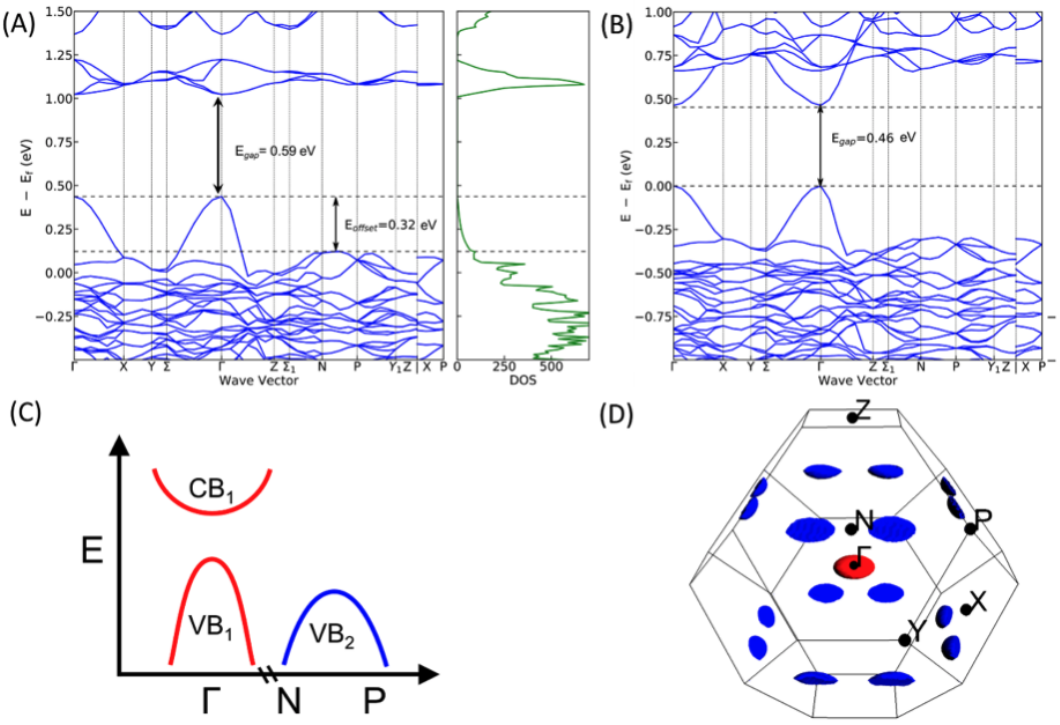

Figure 4.2: (A) DFT band structure and density of states for $Yb_{14}MgSb_{11}$. (B) DFT band structure for $Yb_{14}AlSb_{11}$. (C) A schematic of the simplified model used to model transport for this solid solution, $Yb_{14}Mg_{1-x}Al_xSb_{11}$. (D) Fermi surface of VB1 and VB2 between N P, and Γ.

pocket of the Fermi surface (Figure 4.2 (D) is at a low symmetry position between N-P which gives it a high valley degeneracy, Nv = 8 (each pocket is on the Bragg planes of the Brillouin zone so that 16 half-pockets are shown). The calculated band gap between the two compounds changes by a small amount from $E_{gap,Mg} = 0.586$ eV to $E_{gap,Al} = 0.463$ eV. The band structures also show that as Al is substituted by Mg, bands are filled, reducing the carrier concentration, and moving the Fermi level up. For low x ($Yb_{14}Mg_{1-x}Al_xSb_{11}$), there will be holes deep into the valence band indicating that samples with a larger carrier concentration or lower x will have more access to VB2.

4.2.2. Synthesis of Metal to Insulator Solid Solution

Figure 4.3A shows lattice parameters of $Yb_{14}Mg_{1-x}Al_xSb_{11}$ vs. Al concentration. With the exception of x = 0.1, as Al is substituted into the structure a systematically increases and c decreases. Overall, the volume of the unit cell systematically decreases as a function of increasing x. The powder X-ray diffraction patterns for $Yb_{14}Mg_{1-x}Al_xSb_{11}$ (x = 0.0, 0.1, 0.3, 0.5, 0.7, 0.9, 1.0) are provided (section **??**) and indicate good phase purity.

Figure 4.3B shows carrier concentration and Hall mobility vs nominal Al fraction at 600 K. $Yb_{14}Mg_{1-x}Al_xSb_{11}$ initially increases and then systematically decreases with added Al as expected. At low x, the doping efficiency of Al is lower than expected. The lower than expected carrier concentration by about 63% could be due to the experimental uncertainty of the Hall measurement or indicate the presence of a compensating Yb valence or intrinsic defect manifestation. $Yb_{14}MgSb_{11}$ has been shown to contain Yb^{3+} and intermediate valent Yb by XANES, magnetic and heat capacity studies[113;114].$Yb_{14}ZnSb_{11}$, with the smallest unit cell reported to date and high carrier concentration, shows intermediate valent Yb[113;114]. In the case of $Yb_{14}Mg_{1-x}Al_xSb_{11}$, the smaller unit cell and disorder added with the solid solution may initially increase the tendency for intermediate valency until the carrier concentration is diminished[114;103;115]. The addition of an extra electron from Al may be adjusting the amount of Yb^{3+} in the case of low x, buffering the system with intermediate valent Yb until $x \approx 0.5$, thereby reflecting a lower than expected carrier concentration at low x. Intrinsic acceptor defects could also be playing a role at low Al concentrations leading to the inconsistent trend.

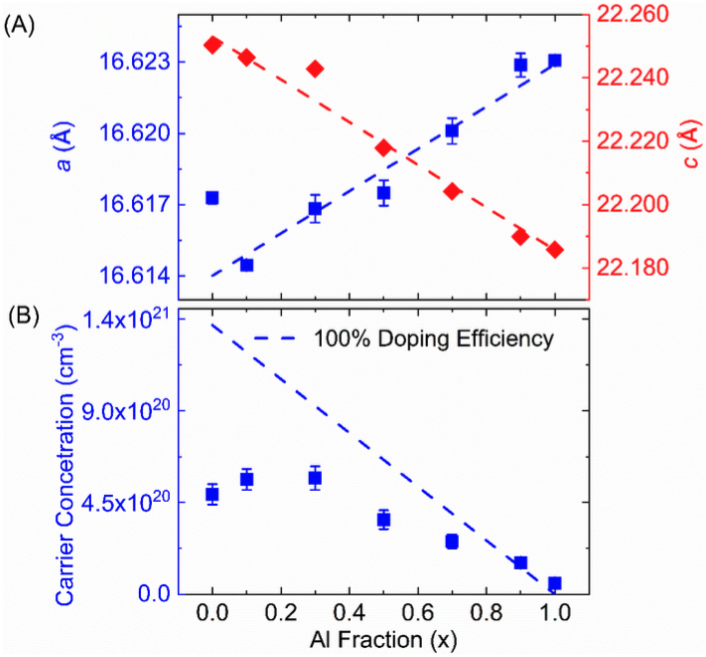

Figure 4.3: (A) Nominal Al fraction (x) in $Yb_{14}Mg_{1-x}Al_xSb_{11}$ vs a and c. As x increases the a lattice parameter decreases and the c lattice parameter increases leading to an overall contraction in unit cell volume. (B) Carrier concentration vs nominal Al fraction, x, at 600 K for $Yb_{14}Mg_{1-x}Al_xSb_{11}$. Carrier concentration and mobility are correlated in a similar but opposite manner as x increases, as expected.

4.2.3. Transport

The experimental Seebeck and resistivity temperature dependent measurements are compared to the simulated Seebeck and resistivity in Figure 4.4. A model consisting of two valence bands and one conduction band was used to describe transport in our system. Experimentally, the Hall carrier concentrations of all compositions, x, are approximately constant until bipolar conduction appears at higher temperatures. To compare experimental data to our model we plot different fixed carrier concentrations in the range of what is experimentally observed. Looking at the modeled output data one can see the

addition of a second valence band can cause the crossing of the Seebeck coefficient in x = 0.1 vs x = 0.5 (n 3×10^{20} vs n 6×10^{20} in Figure 4.4) observed experimentally. This behavior, also seen in the $Yb_{14}Mn_{1-x}Al_xSb_{11}$ solid solution[19], cannot be explained from transport arising from a single parabolic band and occurs due to the way the selection functions for electrical conductivity and Seebeck coefficient (VB1, VB2, Figure 4.2B&C) sample differently the states from each band as a function of carrier concentration and temperature.

Another way of visualizing the impact the second valence band has on thermoelectric transport is through a Pisarenko plot (Figure 4.5A), which shows the relationship between the carrier concentration and Seebeck coefficient of a material. At 400K the large increase in the DOS from the 2nd valence band (VB2) compared to only having the 1st valence band (VB1) results in the increase in Seebeck coefficient that peaks around $10^{21} cm^{-3}$ carriers. At low temperatures and carrier concentrations, a single parabolic band can well describe the transport properties of this solid solution. However, at higher temperatures the Fermi-Dirac distribution is broader and samples this higher DOS band, resulting in Seebeck coefficients larger than what a single parabolic band model would predict as seen in Figure 4.5A&B. Additionally, at higher carrier concentrations the Fermi-level of the material is pushed down closer to the band edge of VB2 (Figure 4.2B), thereby making the Fermi-Dirac distribution more likely to select those states. Analyzing the transport arising from these two bands as if it were coming from a single band, done in an effective mass analysis, would result in the resulting DOS effective mass increasing with increasing temperature and carrier concentration. This increase in effective mass with temperature and carrier concentration is what previous experimental studies[116;103] have reported for

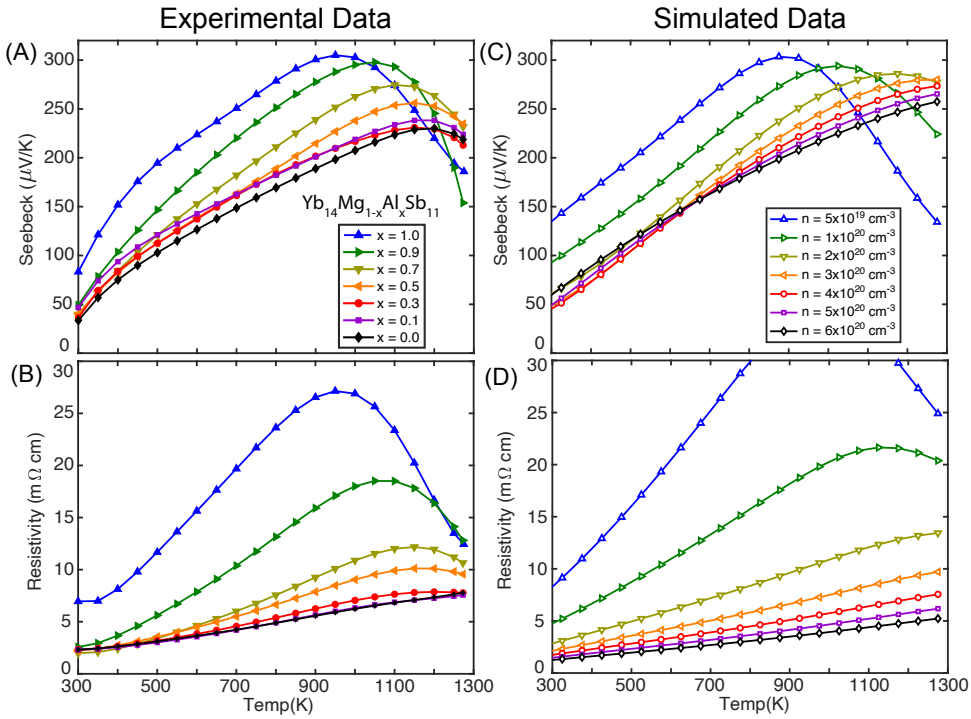

Figure 4.4: Seebeck coefficient (A) and resistivity (B) vs temperature for experimental data $Yb_{14}Mg_{1-x}Al_xSb_{11}$ (x = 0.0, 0.1, 0.3, 0.5, 0.7, 0.9, 1.0) compared to the simulated Seebeck coefficient (C) and resistivity (D) arising from the three-band model (see SI for details). The simulation was generated with a fixed carrier concentration. As Al fraction increases, the turnover in Seebeck coefficient and resistivity occurs at a lower temperature because of increased hole concentration. Note how the simulation shows the Seebeck coefficient of differently doped samples cross one another at 600 K. This behavior which has previously been unexplained is witnessed in the experimental data as well as the previous solid solution study of $Yb_{14}Mn_{1-x}Al_xSb_{11}$[19].

different compounds of the $A_{14}MPn_{11}$ structure and is seen in Figure 4.5B. A typical SPB model would predict Seebeck decreases as a function of carrier concentration, but as seen in Figure 4.5B our multiple-band model predicts the observed retention or increase of Seebeck with increasing carrier concentration. As a result, the Seebeck can be increased without increasing electrical resistivity leading to the maximum power factors $\left(PF = \frac{S^2}{\rho}\right)$ at x = 0.1 and 0.3 (Figure 4.5C).

As the composition of the solid solution is varied from the $Yb_{14}MgSb_{11}$ end member to $Yb_{14}AlSb_{11}$ the carrier concentration decreases, and the Fermi-level is moved closer to the conduction band. This can explain why $Yb_{14}AlSb_{11}$ experiences a maximum in Seebeck and resistivity at a lower temperature than other samples and then is followed in successive order by samples with increasing Mg content. At elevated temperatures, where the Fermi-Dirac distribution is very broad, the least doped material will be the first to have states from the conduction band (CB,Figure 4.2C) sampled thereby activating minority carriers. The experimental band gap calculated from the Goldsmid and Sharp expression ($E_g = 2eS_{max}T_{max}$) does not significantly change as a function of composition and is very close to the computed DFT value for $Yb_{14}MgSb_{11}$ ($E_{gap} = 0.586$ eV), which supports the change in the onset of bipolar conduction is due to doping[117].

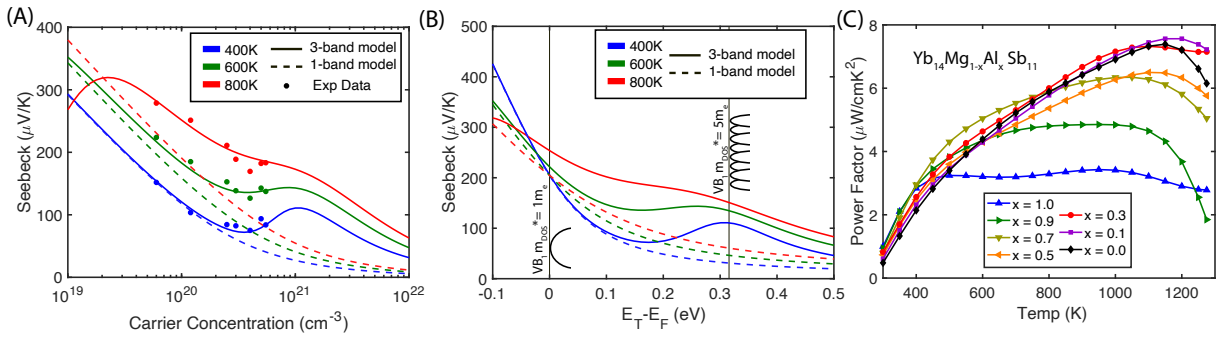

Figure 4.5: (A) Pisarenko plot for samples made in this study. Points are measured values 400K (blue), 600K (green), and 800K (red). The dashed lines give the relationship between Seebeck coefficient and carrier concentration for a material with a single parabolic band with an effective mass of 1me at these temperatures. The solid lines give the relationship between Seebeck coefficient and carrier concentration for a material with two valence bands offset in energy by 0.315 eV with the same intrinsic mobility but different masses (VB1: m*= 1me, VB2: m* = 5 me) and (B) Seebeck coefficient vs Fermi level relative to the band edge of the first valence band at 400K (blue), 600K (green), and 800K (red) for a single parabolic band (dashed lines) and the three-band (solid lines) model described in this paper. Notice the local maximum in Seebeck that results close to the band edge of the second valence band (VB2) (C) Power factor vs temperature for $Yb_{14}Mg_{1-x}Al_xSb_{11}$(x = 0.0, 0.1, 0.3, 0.5, 0.7, 0.9, 1.0).

4.2.4. Multi-Band Effect on Thermal Conductivity

The temperature dependence of thermal conductivity (Figure 4.6A) of the highly doped samples is rather unusual, though similar behavior has been reported in other $A_{14}MPn_{11}$ materials[104;86]. At intermediate temperatures (600 – 900 K) the reduction in thermal conductivity with increasing temperature can be explained via additional phonon scattering. The high temperature behavior (900 K) increase with increasing temperature can be explained with bi-polar conduction, while the low temperature increase (300 – 600 K) in thermal conductivity has been previously misattributed to lattice thermal conductivity[19]. We can now attribute the low temperature increase to electronic effect arising from

the second valence band (VB2, Figure 4.2C). This is qualitatively seen in the simulated electronic thermal conductivity (Figure 4.6B), which as carriers are excited from the first valence band to the second valence band with increasing temperature there is a bipolar-like effect that occurs. (Appendix A, Model Inputs and Visualization). Unfortunately, the overall magnitude of the simulated electronic thermal conductivity is overestimated. This overestimation may have been caused because our model does not consider intervalley scattering, which can have an effect on lowering a material's Lorenz Number[118;119;120]. Therefore, while an accurate lattice thermal conductivity of this material cannot be calculated we can qualitatively explain the temperature dependence of the thermal conductivity. This multi-band model could also be used to explain the unexplained increase in thermal conductivity at low temperatures seen in $Re_{3-x}Te_4$ (Re = Nd, La)[109], SnTe[110], Ag_9AlSe_6[111],and Eu9CdSb9[112]. These phases have reported electronic structures, and while the effect the multiband nature of the electronic structures has on transport properties is acknowledged, an explanation for their low temperature thermal conductivity is not discussed and is most likely also affected by multiple bands. Understanding the impact of the multiband nature on the low temperature thermal conductivity ultimately helps design better thermoelectric materials.

4.2.5. Thermoelectric Performance

Samples' zTs vs carrier concentrations are plotted in Figure 4.7A compared to the three-band model described in this paper and a model that uses only a single parabolic band. The single parabolic band model was created using only the model parameters for the first valence band at Γ (VB1) and describes the low temperature behavior well. To create a

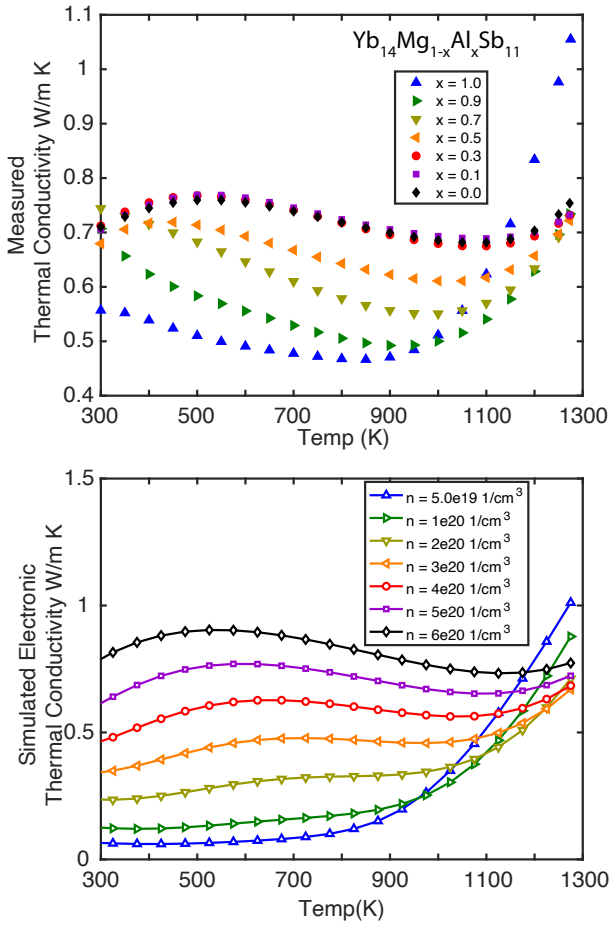

Figure 4.6: (A) Experimental thermal conductivity (κ_{tot}) vs temperature for $Yb_{14}Mg_{1-x}Al_xSb_{11}$ (x = 0.0, 0.1, 0.3, 0.5, 0.7, 0.9, 1.0), compared to (B) simulated electronic thermal conductivity. Note that at high doping levels the simulated electronic thermal conductivity displays the same increase vs temperature that the experimental data experiences. This behavior has previously been attributed to the material's lattice thermal conductivity but can be rationalized as a bipolar-like effect between the two valence bands. Currently, our model likely overestimates the magnitude of electronic thermal conductivity because intervalley scattering processes are not taken into effect.

more accurate estimation of zT vs carrier concentration we used the three-band electronic transport simulation described in this paper as well as a fixed lattice thermal conductivity of 0.3 W/mK. This estimation is reasonable given the complexity of the material's crystal

structure that likely leads the lattice thermal conductivity to be diffusion dominated[107]. We should note that while our model does not account for intervalley scattering, there is a rough canceling of errors as the significantly overestimated electronic thermal conductivity that is part of the denominator of zT, is offset by the slightly overestimated Seebeck coefficient and conductivity that forms the numerator. Based on Figure 4.7 one can surmise the second heavier valence band (VB2) has significantly better thermoelectric transport than the first band (VB1). While larger single band effective masses in materials are generally considered detrimental to a materials zT[121], the high degeneracy (Nv = 8) of the second valence band has the effect of splitting its states into multiple conducting pathways. This has the effect of reducing electron-phonon scattering that would normally be expected from a high DOS band[26]. Modeling the transport arising from only these three-bands suggest even higher zT's may be possible for $Yb_{14}MSb_{11}$ (M = Mn, Mg, Al) if a suitable dopant is found that can increase the carrier concentration of the material such as alkali metals or another +1 metal replacing Yb or Sn/Ge replacing Sb[122;123]. This is contrary to the conclusion reached using a single parabolic band model to analyze the $Yb_{14}Mn_{1-x}Al_xSb_{11}$ solid solution, in which the lower carrier concentration $Yb_{14}Mn_{0.2}Al_{0.8}Sb_{11}$ had the highest zT[19]. In this case an increase in spin disorder scattering from replacing Al with Mn likely obscured the benefits the 2nd valence band had at higher carrier concentrations[124]. In $Yb_{14}Mg_{1-x}Al_xSb_{11}$ series of samples, the x = 0.1 and 0.3 samples which have the highest carrier concentration and power factor also have the highest zT (Figure 4.7B).

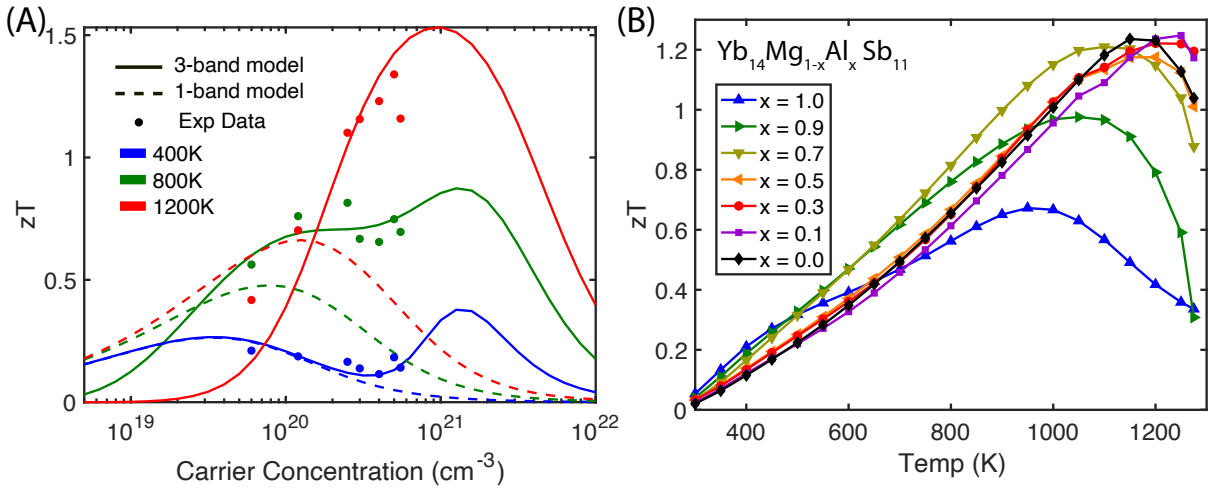

Figure 4.7: (A) zT vs carrier concentration for $Yb_{14}Mg_{1-x}Al_xSb_{11}$ (x = 0.0, 0.1, 0.3, 0.5, 0.7, 0.9, 1.0) compared to a model using a single parabolic band and the model described in this paper. While a single parabolic band model can describe low temperature data reasonably well, it completely fails at predicting the temperature dependent data and at instructing experimentalists the ideal carrier concentration to dope their materials. The work done in this paper suggests increasing the carrier concentration of $Yb_{14}MgSb_{11}$ could lead to even further enhancement in the material's zT. (B) Shows temperature dependent zT. The samples with the highest carrier concentration (x = 0.1 and 0.3) have the highest zT.

4.3. Conclusion

$Yb_{14}Mg_{1-x}Al_xSb_{11}$ (x = 0.0 0.1, 0.3, 0.5, 0.7, 0.9, 1.0) was synthesized by high energy mechanical milling and high temperature annealing. Using DFT guided semi-empirical modeling, we show a highly degenerate (Nv = 8) second valence band is responsible for the good electronic thermoelectric properties of $Yb_{14}Mg_{1-x}Al_xSb_{11}$. By considering the effects of this second band, we can explain the peculiar temperature dependency of thermal conductivity and carrier concentration dependence of Seebeck coefficient of the materials in this solid solution and can potentially apply our second band analysis to other promising thermoelectric materials. Using the multi-band model, we create a more

accurate prediction of the carrier concentration dependence of zT which shows increasing the carrier concentration of $Yb_{14}MSb_{11}$ (M = Mn, Mg, Al) could result in even better thermoelectric performance. Assuming the band structure of the $A_{14}MPn_{11}$ structure type holds across different compositions, this work opens a new strategy for optimization for zT improvements and could lead to groundbreaking thermoelectric performance.

4.4. Detailed Methods

4.4.1. Materials

Materials were manipulated in an argon-filled glove box under 1 PPM of water. Mg turnings (99+%, Strem Chemicals), Sb shot (99.999%, 5N Plus), fresh Yb filings (<2 mm) prepared using a large-toothed steel rasp from a Yb ingot (99.95%, Edge Tech) cleaned with a wire brush before use, and Al filings (<2 mm) prepared from Al shot (99.999%, Alfa Aesar) using a large-toothed steel rasp after arc-welding under argon to remove oxide and cleaning with a steel brush.

Mg_3Sb_2 Synthesis was adapted from literature[108]. 10 g of stoichiometric Mg and Sb were placed in a SPEX tungsten carbide grinding vial set (55 mL, 2 $\frac{1}{4}$ in. Diameter x 2 $\frac{1}{2}$ in. long) with three 10.75 g tungsten carbide balls. The vial was hermetically sealed with custom Viton O-rings and mechanically milled for an hour using a SPEX 8000D mixer/miller. 5 g of the clumpy black powder was removed using a chisel and placed in a 10 cm Ta tube which was sealed under Ar. The Ta tube was jacketed in a fused silica tube under vacuum and annealed at 800 °C for seven days. The result was a solid black ingot that was smashed out of the container using a hammer.

4.4.2. Sythesis

Synthesis was adapted from literature[86;108]. First, it was experimentally determined that the $Yb_{14}MgSb_{11}$ end member required 14.02Yb: 1.2Mg: Sb11 in order to obtain phase pure product. Next, it was determined that $Yb_{14}AlSb_{11}$ required 14.02Yb: 1.05 Al: Sb11 to obtain phase pure product. A linear fit ($y = -0.15x + 0.2$) where x = Al fraction y = Mg/Al excess was used to determine the excess Al/Mg at a given Al fraction (x) according to the formula $Yb_{14}Mg_{1-x}Al_xSb_{11}$ where 80% of the excess was Mg and 20% of the excess was Al. $Yb_{14}Mg_{1-x}Al_xSb_{11}$ was synthesized by placing $\frac{(1-x)+(y\times 0.8)}{3}$ Mg_3Sb_2, $11-(2\times\frac{(1-x)+(y\times 0.8)}{3})$ Sb and $(x+(y\times 0.2))$ Al in the hermetically sealed tungsten carbide milling setup described above with two 10.75 g tungsten carbide balls and mechanically milled for 15 minutes producing a fine black powder. 14.02Yb was added to the mixture and milled for 30 minutes resulting in black powder with some small chunks which was scraped out of the tungsten carbide vial with a chisel. 5 g of the powder was placed in a 7.5 cm Nb tube then arc-welded shut under an Ar atmosphere. The Nb tube was jacketed with a fused silica tube under vacuum and then placed in an alumina cup to ensure even heating. The samples were heated in a box furnace to 850 °C at a rate of 50 °C/hr and held at 850 °C for 96 hours then let cool to room temperature. The reaction vessels were opened inside a glovebox. The result was a fine black powder with some annealed chunks. A 100-mesh sieve was used to exclude any large pieces yielding 4 g of powder.

4.4.3. X-Ray Diffraction

Diffraction experiments were done using a Bruker D8 Eco Advance diffractometer operated at 40 kV and 25 mA at 298 K using Cu Kα radiation (λ = 1.5405). Data were collected

from 15° to 90° 2 at a 0.0194 ° step size. 2 wt.% Si powder (Fisher Scientific, 99.999%) was ground into the sample to ensure accurate lattice parameters. JANA 2006 software package was used for Rietveld refinement. Models for Rietveld refinement were generated from Si and $Yb_{14}MgSb_{11}$ crystallographic information files[104;125]. Sample height correction, manual background, and lattice parameters were fit first. A pseudo-Voigt function was used to generate the profile shape. E.S.D.s were multiplied by Berar's factor to give realistic values[126]. Mg-Al fraction was not refined because of similarity in Mg/Al X-ray scattering factors.

4.4.4. Sintering

3g of powder was loaded into a 12.7 mm diameter graphite die with graphite plungers and 12 sheets of graphite foil on each side to ensure air-free conditions and avoid having the sample stick to the plungers. The die was inserted into a Dr. Sinter-Lab Jr. SPS-2ll LX with a thermocouple inserted into a hole drilled in the side of the die. The material was initially cold pressed at 28 MPa (on the cross-section). During sintering sample was pressurized to 15 MPa (on the cross-section) for four minutes then the pressure was increased to 55 MPa (on the cross-section) over two minutes and held for the remaining 15 minutes. The sample was simultaneously heated from room temperature to 750 °C over five minutes then to 800 °C over one minute and held at 800 °C for fifteen minutes. The result was a 3 mm thick black/metallic puck that was cut into 1 mm thick disks for laser flash analysis (LFA), Hall effect and Seebeck coefficient measurements. Sample density was geometrically determined. All samples were >97% of crystallographic density.

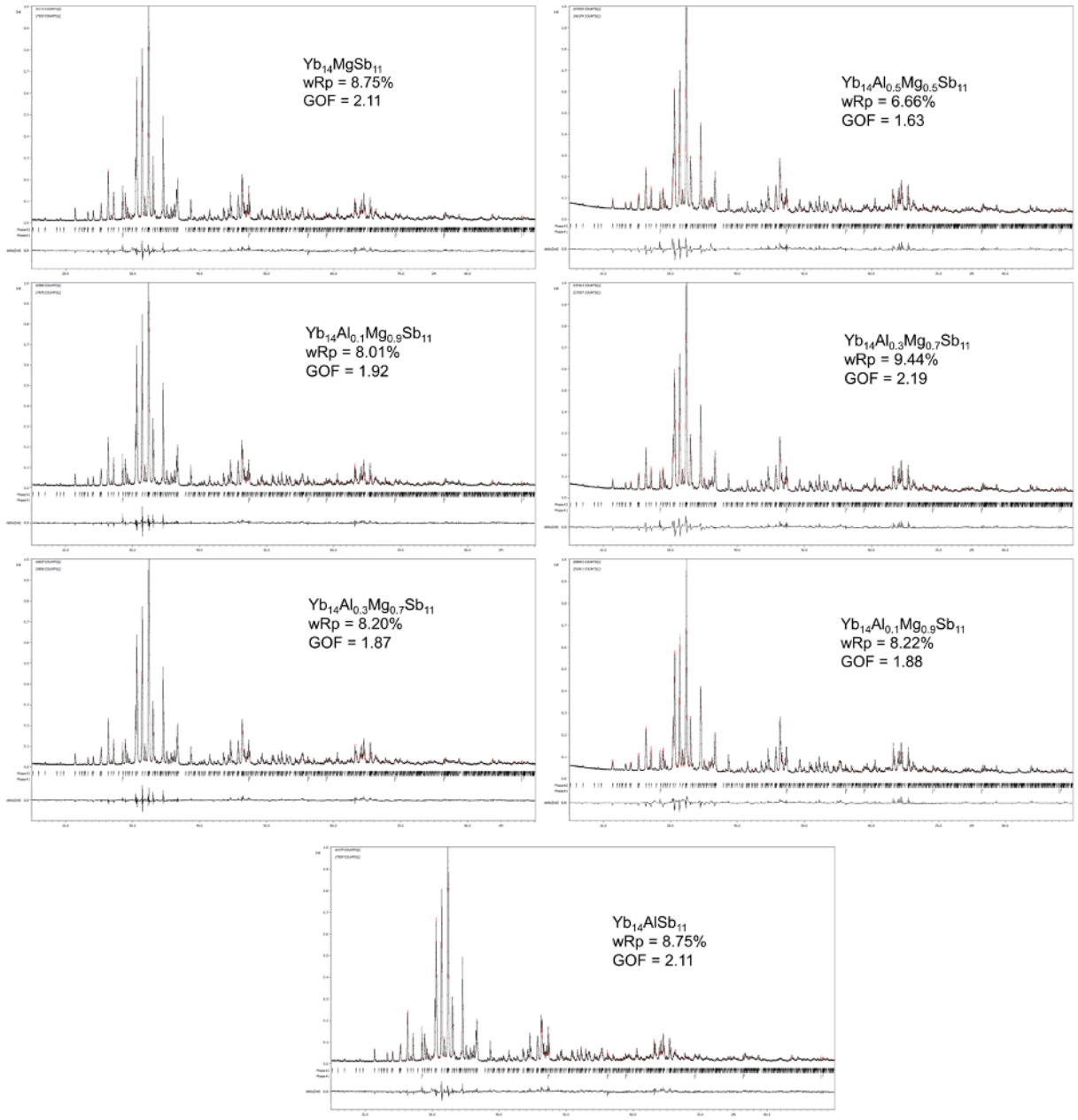

Figure 4.8: Rietveld refinement for $Yb_{14}Al_xMg_{1-x}Sb_{11}$ with data plotted in black, simulated data in red, and difference curve at the bottom. wRp and GOF are displayed in the image.

4.4.5. Transport Measurements

Thermal diffusivity was measured on 1 mm thick sintered pellets polished flat and parallel and sprayed with graphite to ensure laser absorption. A Netzsch LFA 457 laser flash system was used. Diffusivity data is shown in SI, Figure S8. Thermal conductivity was calculated using $\kappa = D\ x\ C_P\ x\ \delta$ where D is measured diffusivity and δ is the temperature adjusted density for $Yb_{14}MnSb_{11}$[127]. CP measurements on $Yb_{14}Mn_{1-x}Al_xSb_{11}$ single crystals grown from tin flux showed that the Cp was constant for samples of the composition x = 0.2 to x = 0.95 indicating that the M site in the $Yb_{14}MSb_{11}$ structure has minimal contribution to the heat capacity of $Yb_{14}MnSb_{11}$[128], so the Cp reported on sintered pellets of $Yb_{14}MnSb_{11}$ will be used[86].

Temperature-dependent Hall effect and resistivity measurements were done on flat and parallel sintered pellets using a custom instrument that employs the Van der Pauw method with tungsten contacts and a 0.8 T magnet under high vacuum[129]. A heating rate of 180 K/hr was used. For viewing ease and zT calculations data was fit with a sixth order polynomial.

The Seebeck coefficient was measured on sintered pellets using a custom-build instrument employing the light pulse method. Tungsten-niobium thermocouples were used[130]. As Al increases samples have a hysteresis in Seebeck and resistivity data, but not thermal conductivity data. When samples are polished and remeasured, the same data is unchanged.

4.4.6. Density Functional Theory

The electronic band structures were calculated within Density Functional Theory (DFT), using the Vienna Ab initio Simulation Package (VASP)[131;132] with the Perdew-Burke-Ernzerhof (PBE) generalized gradient approximation (GGA) functional and adopting the projector augmented-wave (PAW)[133;134] approach. The Yb pseudopotential has the 4f electrons frozen in the core (i.e. not as valence electrons). This was motivated by a previous XPS study, which indicated that Yb4f states in $Yb_{14}MnSb_{11}$ and $Yb_{14}ZnSb_{11}$ are below the Fermi level by more than 0.5 and 1 eV respectively[115]. We also performed some tests with the PAW Yb pseudopotential providing f electrons as valence electrons and applying different Hubbard U values on the f states. The typical U values used in previous work on other Yb antimonides52 lead to f states much lower than the valence bands confirming that f states could be neglected shown in figure S10. The primitive structures were relaxed until the forces are less than 0.01eV/A. During the relaxations and static runs, the wave functions were expanded on a plane-wave basis set up to an energy cutoff of 520 eV and the Brillouin zone was sampled using a 2×2×2 Monkhorst-Pack k-point grid. A non-self consistent field (NSCF) calculation on a 8×8×8 k-points grid was performed in order to calculate the DOS and the Fermi surface. Then, by using the BoltzTraP[135;136] software, the eigenvalues were interpolated on a 10 times denser grid to obtain the DOS, and on a 100 times denser grid to obtain the Fermi surface. Pymatgen[137;54] was used for post-processing such as plotting the band structure on the standard high symmetry k-point path[138] and the Fermi surface.

4.4.7. Multi-Band Model

For the modeled transport data, a three-band model was created using DFT inputs from $Yb_{14}MgSb_{11}$ for the band offsets between the two conduction bands ($E_{offset} = 0.315$ eV) as well as the band gap ($E_{gap} = 0.586$ eV). Additional inputs needed for this model are the intrinsic mobility and effective mass of each band. We find that the following parameters qualitatively describe the experimental data measured, however slight adjustments in these parameters would also likely suffice. The intrinsic mobility for each band was set at 25 cm^2/Vs at 300K and decreased proportionally to $T^{-1.5}$ with temperature. The DOS mass of the first valence band ($m*_{VB1}$) was set to 1me, the DOS mass of the second valence band ($m*_{VB2}$) was set to 5me, and the DOS mass of the conduction band ($m*_{CB}$) was set to 4me. For all simulated data the carrier concentration was kept fixed and the Fermi level was varied with temperature in order to ensure charge neutrality of the simulated sample[91]. We would like to point out that the features in the Seebeck coefficient and thermal conductivity vs temperature and doping level that this paper set out to investigate cannot be explained by a transport function of a single band, and require the two valence bands offset in energy to be accurately described.

CHAPTER 5

Using Defects to Alter a Band Structure: $CaZn_{2-x}Mg_xSb_2$

(This chapter contains content reproduced with permission from the Journal of Materials Chemistry A, DOI: 10.1039/C8TA02250J)

5.1. Introduction

P-type 1-2-2 Zintls have been shown to display high thermoelectric efficiencies[139;140;141;142;143;144;145;146;1 $CaZn_2Sb_2$ and $CaMg_2Sb_2$ both have the $CaAl_2Si_2$ structure type (Pm1) (Figure 5.1). Having isotypic crystal structure, these compounds very easily form solid solutions with one another. The structure can be described as having two-atom thick layers of an ionic substructure of $(Zn_2{-}xMgxSb_2)^{-2}$, where each Sb and Zn(Mg) atom is four-fold coordinated. Ca atoms separate these layers and are located in the octahedral interstices formed by Sb atoms[150].

Zhang et al. largely inspired this work where they laid out an approach to create valley degeneracy in a material by converging the energies of the p_x, p_y, and p_z valence band maximum in compounds of the $CaAl_2Si_2$ structure[20]. These different bands may each have a different mobility and effective mass that will affect transport in the material[21]. In $CaMg_2Sb_2$ the p_z band is above the p_x and p_y bands by approximately 0.13 eV, while in $CaZn_2Sb_2$ the p_x and p_y bands are above the p_z band by approximately 0.1 eV. Assuming linearly changing rigid bands and an inverse lever law relationship, we

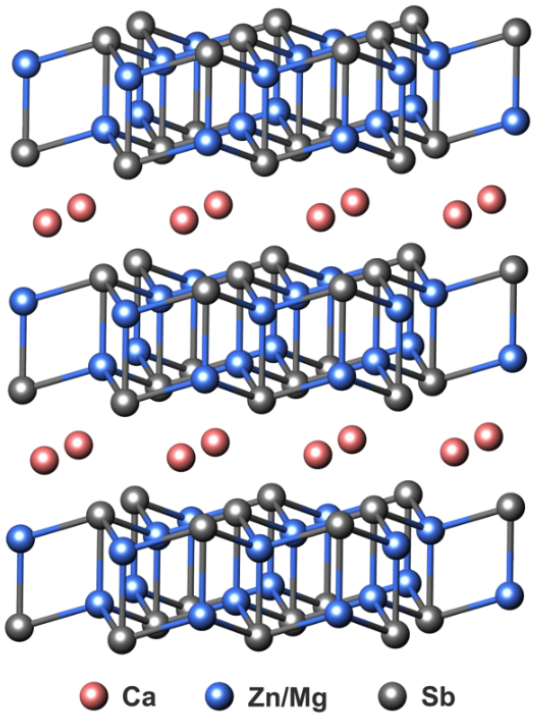

Figure 5.1: Crystal structure of $CaZn_{2-x}Mg_xSb_2$ with layers of anionic $(Zn_{2-x}Mg_xSb_2)^{-2}$ separated by Ca^{2+} cations.

determined convergence would occur around the composition $CaMg_{0\cdot 86}Zn_{1\cdot 14}Sb_2$ (Figure 5.2. Analyzing transport using a single parabolic band type model, we would expect the DOS effective mass of the converged sample to peak at a local maximum according to $(m_{DOS}{}^*)^{\frac{3}{2}} = N_V(m_b)^{3/2}$, with the masses of the samples on the zinc rich side of this sample decreasing to one value, and another value for samples on the magnesium rich side[55].

These offsets and band positions can change, and even flip, depending upon the calculation[151;143;20]. More specifically Zhang et al. reports $CaMg_2Sb_2$ to have a singly degenerate band with a higher energy than a doubly degenerate band at Γ at the valence

band maximum[20]. Meanwhile Singh et al. reports $CaMg_2Sb_2$ to have a doubly degenerate band with a higher energy than a singly degenerate band at Γ at the valence band maximum[56]. Furthermore a sample's physical properties measured at elevated temperatures may differ from DFT calculations run effectively at 0 K due to thermal expansion and phonons[152]. Therefore in addition to this predicted converged sample, samples of the end members and various compositions in between the solid solution were also synthesized and studied.

Herein we analyze our data using an effective mass model[55;153] and show that while we don't see a peak in effective mass, which would indicate converging bands, we do see an abrupt change, doubling the effective mass near the predicted composition. This indicates transport is changing from one set of band(s) on the Zn side to another on the Mg side. Additionally, we analyze the thermal conductivity of our samples with a modified Klemens model used by Yang et al.[154] and show samples are getting a boost in zT due to alloy scattering in the lattice thermal conductivity. Furthermore, we report the thermoelectric properties of $CaMg_2Sb_2$ for the first time and obtain a peak zT of 0.87 in the sample $Ca_{0\cdot 99}Na_{0\cdot 01}MgZnSb_2$ at 850 K.

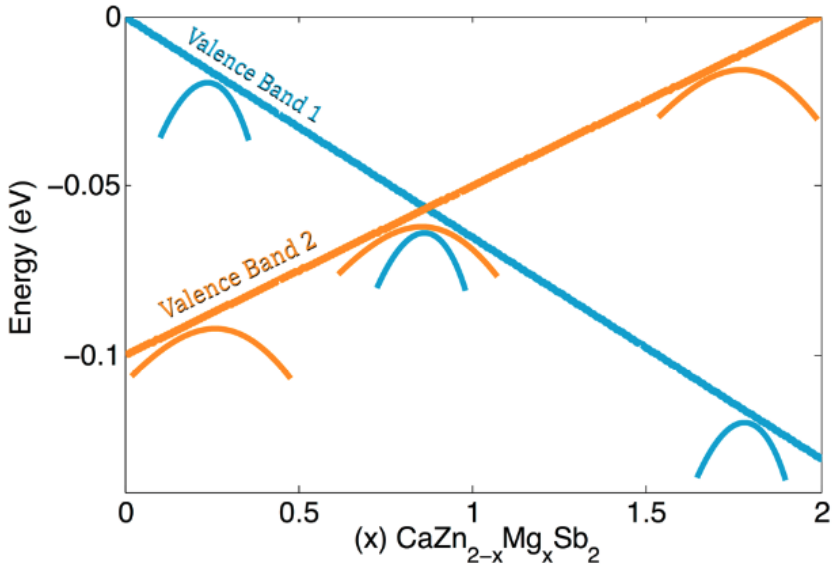

Figure 5.2: Visualization of the predicted energy offsets of the valence bands in the $CaZn_2Sb_2$−$CaMg_2Sb_2$ solid solution. Offsets in the end members were taken from Zhang et al.[20] and then linearly interpolated with changing composition.

5.2. Results

5.2.1. x-ray Diffraction

X-ray diffraction shows a solid solution was indeed obtained for all compositions tried with the lattice parameters linearly increasing as Mg substitutes Zn on the transition metal site (Figure 5.3). X-ray analysis further reveals there is no substantial impurity phase in our samples (Figure 5.4)).

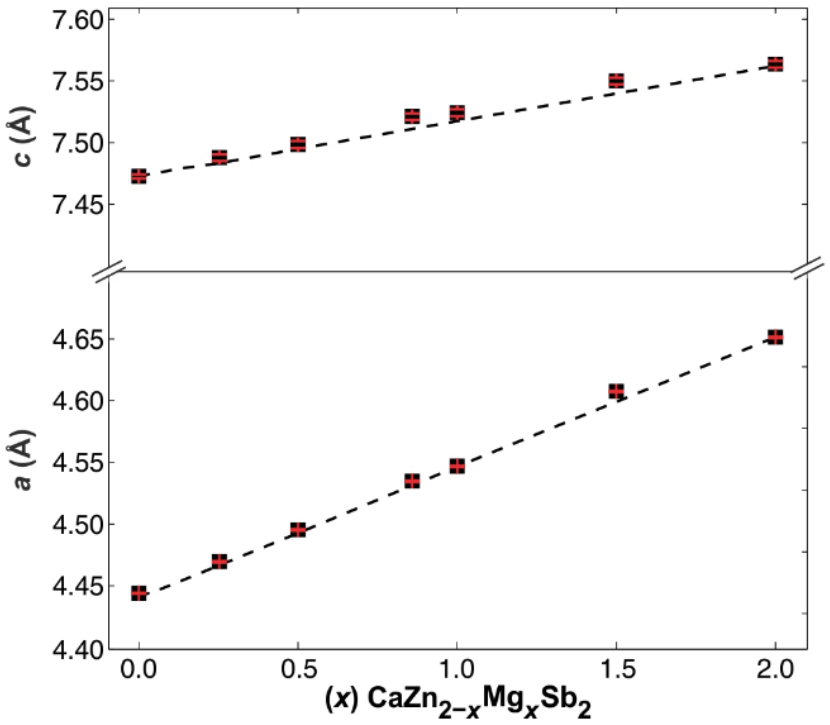

Figure 5.3: Lattice parameters a and c for compounds $CaZn_{2-x}Mg_xSb_2$ (x = 0, .25, .5, .86, 1, 1.5, 2) determined from x-ray diffraction analysis. The error is shown in red, and the dashed line is a guide to the eye. Note that the error in all samples is less than the point side of the data.

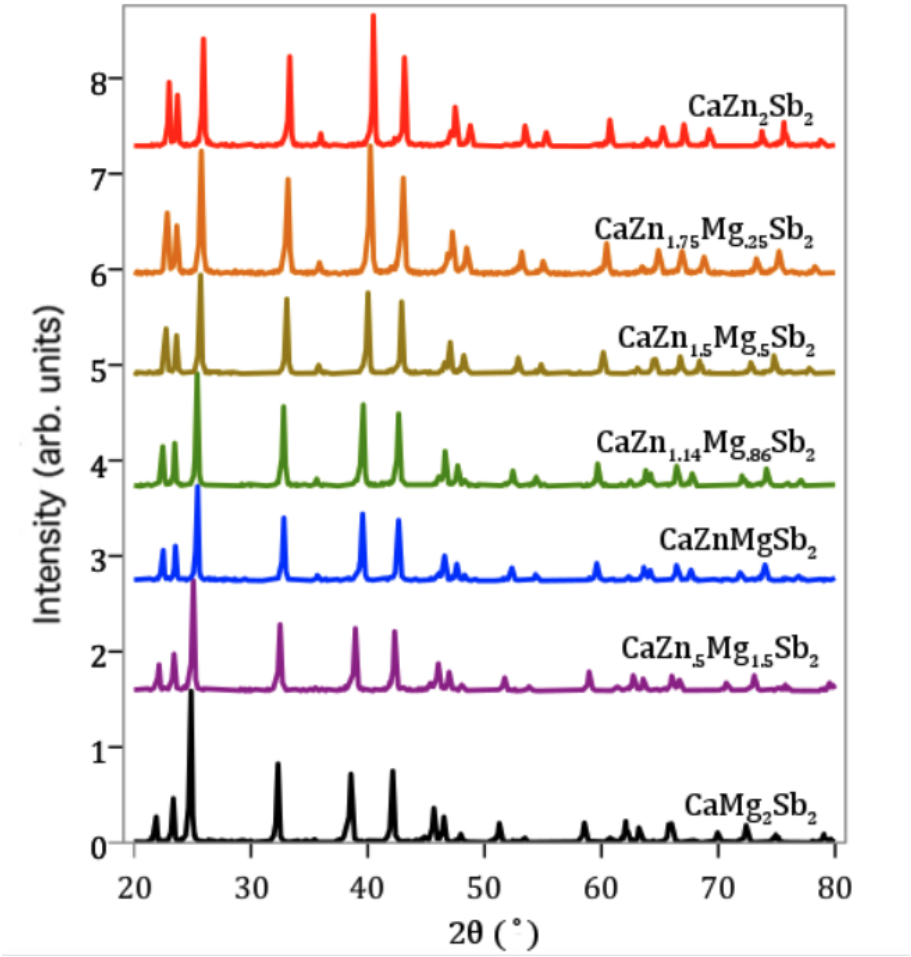

Figure 5.4: XRD patterns of $CaZn_{2-x}Mg_xSb_2$ samples. Peak shifting due to changing lattice parameter is linear with respect to composition in both the a and c axes.

5.2.2. Transport Results

From previous DFT studies we expect the band gap to widen as we substitute Mg on to the Zn site[151;139]. Samples without Na doping decrease in carrier concentration as Mg^{2+} substitutes Zn^{2+} widening the band gap and changing the sample from degenerately doped p-type at the Zn side to an intrinsic insulator on the Mg side (Figure 5.5). Seebeck coefficient and resistivity follow an expected trend; both increasing with the substitution of Mg for Zn. Samples with nominal composition $CaZn_{0.5}Mg_{1.5}Sb_2$ and $CaMg_2Sb_2$ were too resistive to measure in our hall measurement system. Therefore, Na was chosen as a p-dopant for samples whose carrier concentrations were less than optimal, because of its similar ionic radii to Calcium. Samples with nominal compositions $Ca_{0.99}Na_{0.01}Zn_{2-x}Mg_xSb_2$ were then created to degenerately dope all samples (Figure 5.6) in which an effective mass model[55] indicated doping was less than optimal.

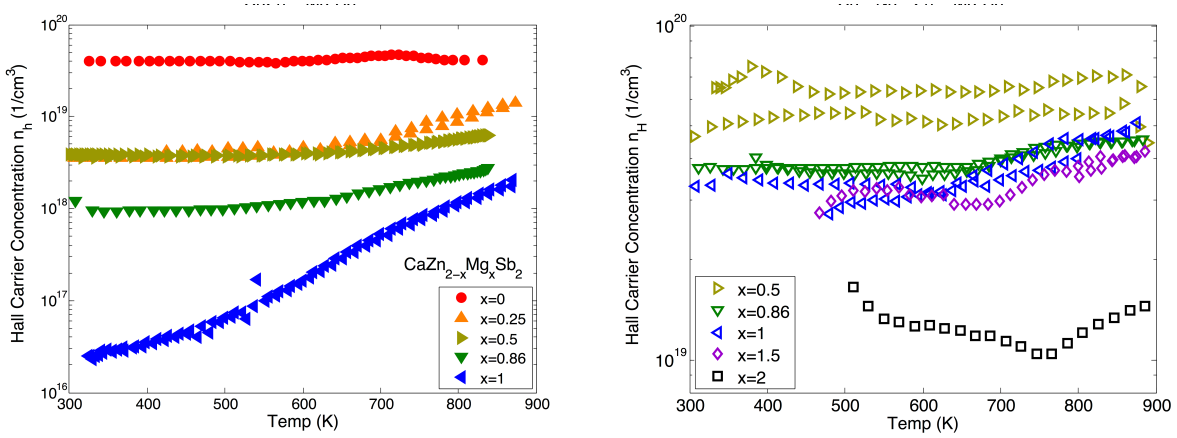

Figure 5.5: (a) Hall Carrier Concentration for compounds $CaZn_{2-x}Mg_xSb_2$ (x = 0, .25, .5, .86, 1) (b) Hall Carrier Concentration for compounds $Ca_{0.99}Na_{0.01}Zn_{2-x}Mg_xSb_2$ (x = .5, .86, 1, 1.5,2)

Substituting Mg on to the Zn site has the effect of lowering the mobility of samples (Figure 5.7). Displaying the temperature dependence of $T^{-3/2}$, the mobility data on the Zn rich-side of the solid solution is characteristic of deformation potential scattering. Moving to the Mg-rich side it appears some other type of scattering dominates at low temperatures but deformation potential scattering is still effective at higher temperatures. This low temperature behavior is likely due to grain boundary scattering seen in the related compound Mg_3Sb_2[155], though deserves further study. We attribute U shaped curve in sample $Ca_{0.99}Na_{0.01}Mg_2Sb_2$ to grain boundary scattering, with the decrease in resistivity at higher temperatures likely due to bipolar conductivity. The thermal conductivity of the two end member samples shows an expected higher thermal conductivity than samples that are solid solutions, primarily due to alloy scattering in the solid solution samples. Samples that are doped with Na show higher thermal conductivity than their un-doped counterparts due to the electronic portion of the thermal conductivity being larger.

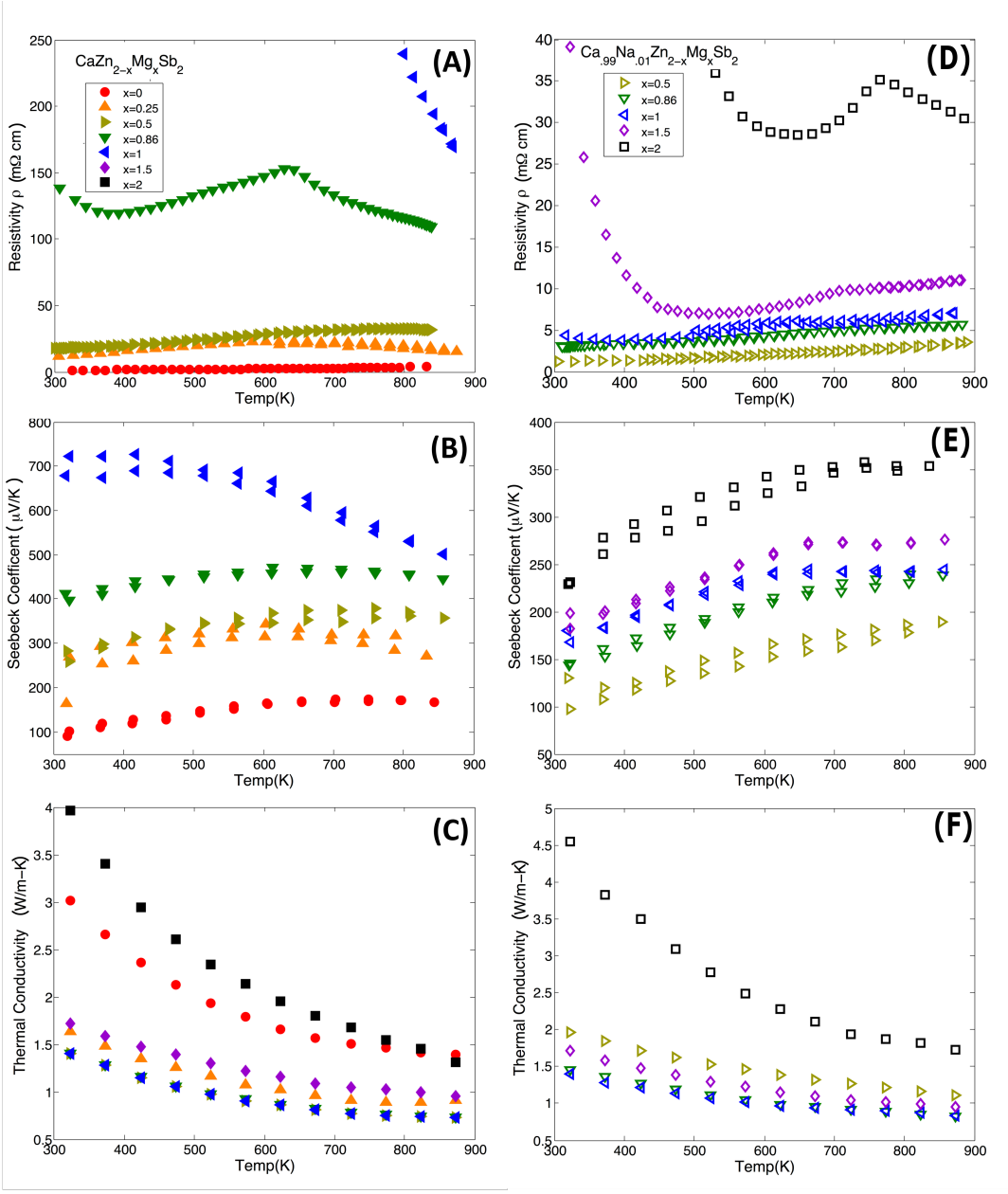

Figure 5.6: (a) Resistivity , (b) Seebeck, and (c) thermal conductivity data for undoped samples. (d) Resistivity , (e) Seebeck, and (f) thermal conductivity data for samples with 1% nominal Na substitution on the Ca site

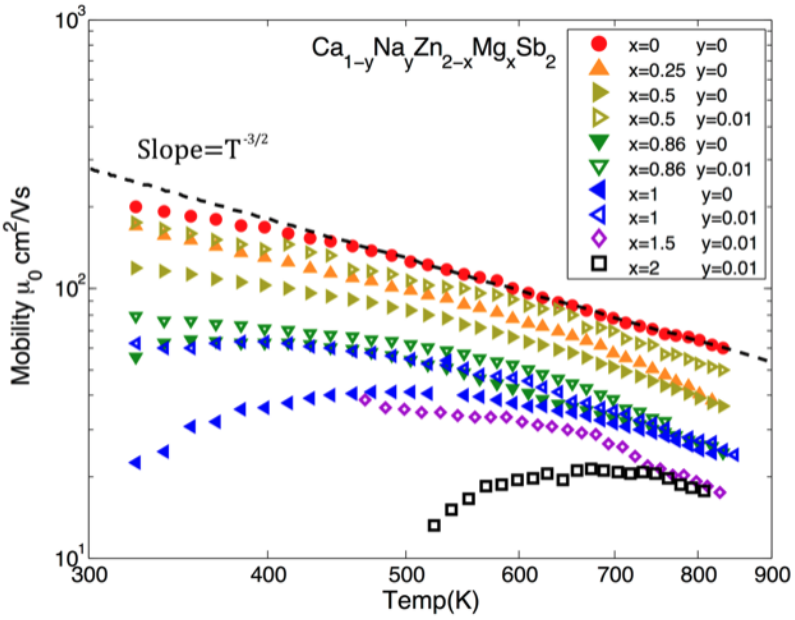

Figure 5.7: Mobility vs temperature for all samples measured. The addition of Mg onto the Zn site has the effect of decreasing mobility as well as changing its temperature dependence. At higher temperatures, most samples have a temperature dependent mobility characteristic of deformation potential scattering.

5.3. Discussion

5.3.1. Effective Mass Model

To analyze and compare the electronic properties of this data set we use an effective mass model (sometimes referred to as a single parabolic band model) at 600 K[55]. This temperature was chosen to compare data because it is before the onset of bipolar conduction for most samples, indicated by a flat carrier concentration and increasing Seebeck value with temperature. Furthermore, at 600 K most samples have a mobility that has a temperature dependence indicating deformation potential scattering allowing us to analyze all our data in a similar fashion (Figure 5.7). We should note grain boundary scattering

does not significantly affect a materials Seebeck, or hall coefficient. Therefore it is reasonable to extract a DOS effective mass from Mg rich samples using deformation potential scattering, even if the mobility's temperature dependence varies from $T^{-3/2}$.

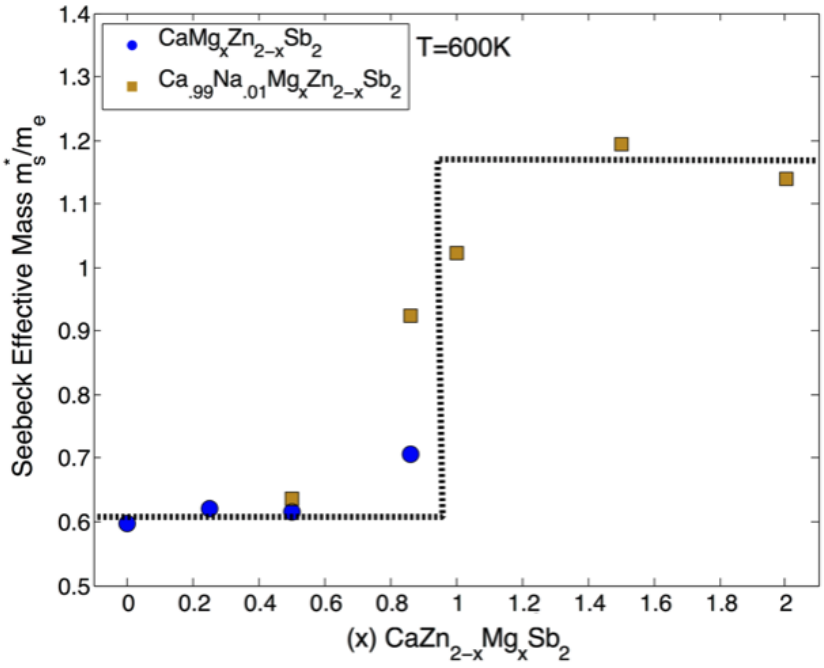

Figure 5.8: Seebeck effective mass[21] vs Mg content of samples at 600 K. While we do not see a maximum indicating band convergence, we do see a step function around the composition we expected convergence to appear indicating that transport is changing from one set of bands to another. The dashed line is a guide for the eye.

In this system, we expect Zn rich samples to have conduction from one band(s), and Mg rich samples get transport from a different band(s). At some intermediate composition, we expect the bands to cross creating a converged sample with transport from both sets of bands. Modeling this converged sample's bands as a single parabolic band would give an effective mass larger than non-converged samples that are more magnesium or zinc rich. While we do not see a local maximum in effective mass for a particular composition, such

as in Bi_2Te_3/Sb_2Te_3[96], our analysis does show effective mass acting as a step function with the Mg side having an effective mass roughly double the Zn side (Figure 5.8). This indicates that transport is indeed changing from one set of bands to another.

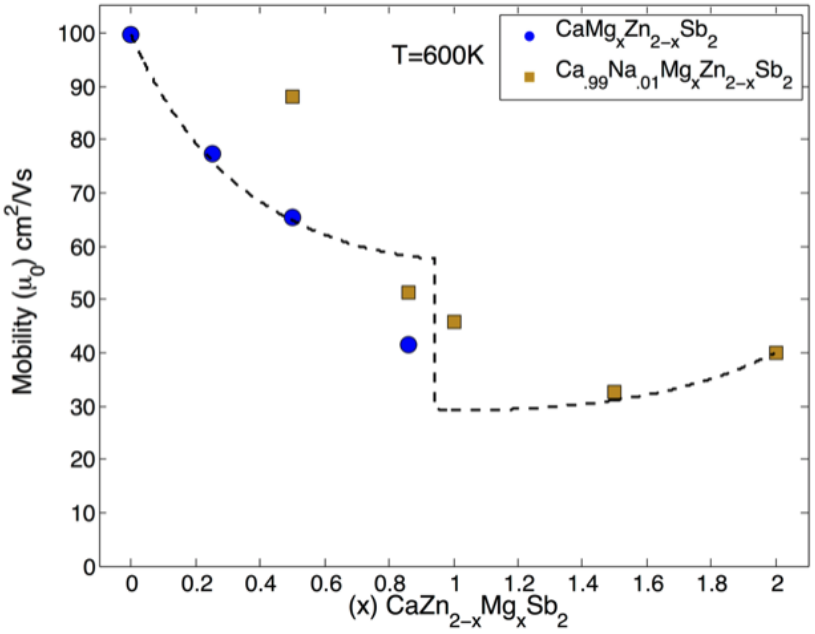

Figure 5.9: Mobility vs Mg content of different samples at 600 K. The data for $Ca_{0.99}Na_{0.01}Mg_2Sb_2$ was taken at 750K then adjusted back to 600K assuming only acoustic phonon scattering. The dashed line is a guide for the eye. The decrease in mobility is most likely due to alloy scattering.

Figure 5.9 shows mobility vs magnesium content for all samples at 600K. In this figure, we have adjusted the data point for $Ca_{0.99}Na_{0.01}Mg_2Sb_2$ in an attempt to compare all samples in a regime where grain boundary scattering does not dominate conduction. This was done by scaling the mobility data of $Ca_{0.99}Na_{0.01}Mg_2Sb_2$ at 750K by $(750K/600K)^{3/2}$ to estimate what the mobility would be at 600K if instead deformation potential scattering were to dominate. The trend in mobility can be described using a combination of alloy

and deformation potential scattering[155]. The trends can be qualitatively explained using a single deformation potential $\Xi = 10$ eV and the same scattering potential U = 0.5 eV for both the Zn-rich and Mg-rich samples if one assumes the bands of the Mg-rich material is doubly degenerate and the Zn-rich is a single band.

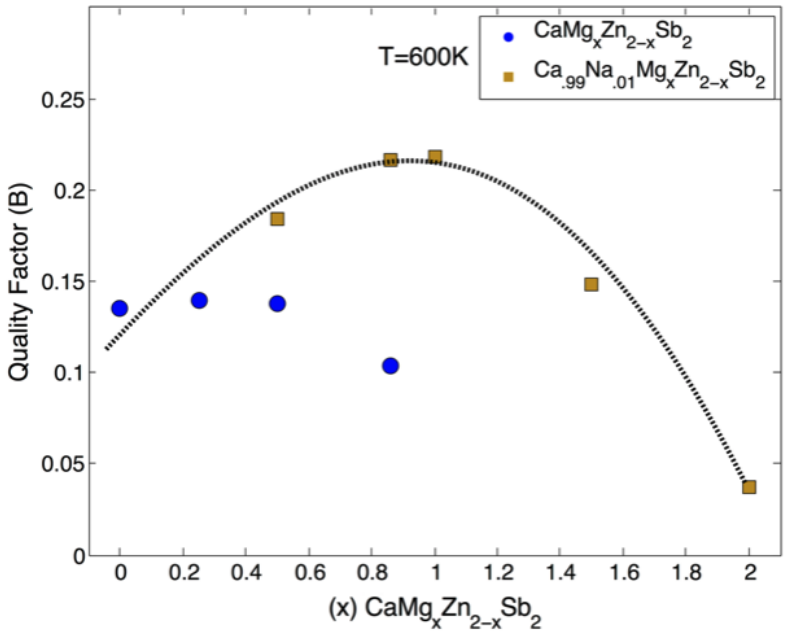

Figure 5.10: Quality factor vs Mg content of different samples at 600 K. Samples near the middle point of the solid solution get a boost in quality factor which is due to alloy scattering in the lattice thermal conductivity. The dashed line is a guide for the eye.

Lattice thermal conductivity does benefit from the solid solution with compositions close to half the Zn sites filled with Mg having the lowest thermal conductivity resulting in a unit-less quality factor[153;55]:

$$B = \frac{k_B^2}{e} \frac{(2m_e k_B)^{\frac{3}{2}}}{3\pi^2\hbar^3} \frac{\mu_0 \left(\frac{m_s^*}{m_e}\right)^{\frac{3}{2}} T^{\frac{5}{2}}}{\kappa_L} \tag{5.1}$$

that peaks around these compositions (Figure 5.10). Quality factor is a material metric that is independent of reduced chemical potential and therefore should be the same for samples of the same composition with different carrier concentrations. However our data shows that undoped samples with composition $CaZn_{1.14}Mg_{0.86}Sb_2$ and $CaZn_{1.5}Mg_{0.5}Sb_2$ have much lower quality factors than their doped counterparts. This is due to the weighted mobilities of these samples being different from their undoped counterparts.

Table 5.1: A comparison between the solid solutions end member's thermoelectric properties at 600K. Note how the larger effective mass and grain boundary scattering in the Mg containing compound hamper mobility. Furthermore zinc's atomic mass being double that of magnesium lowers the thermal conductivity, and overall helps boost the material's quality factor (B).

	$CaZn_2Sb_2$	$CaMg_2Sb_2$
$m_s^*(m_e)$	0.6	1.1
$\mu_0(cm^2/Vs)$	100	19
$\mu_0 * (\frac{m_s^*}{m_e})^{\frac{3}{2}}(cm^2/Vs)$	45	23
$\kappa_L(W/mK)$	1.3	2.4
B	0.135	0.037

5.3.2. Lattice Thermal Conductivity Modeling

To analyze the lattice thermal conductivities we use a model described by Yang et al.[154] based on the theory of Klemens and Calloway[156;157;158;159]. This model proposes a relationship between the lattice thermal conductivities of an alloyed sample ($\kappa_{L,alloy}$) and of a pure compound used in that alloy ($\kappa_{L,pure}$) when Umklapp and point-defect scattering are dominant.

$$\frac{\kappa_{L,alloy}}{\kappa_{L,pure}} = \frac{tan^{-1}(u)}{u} \tag{5.2}$$

$$u^2 = \frac{\pi^2 \theta_D \Omega}{h\nu^2} \kappa_L^D \Gamma_{expt} \tag{5.3}$$

Where u is a scaling parameter, θ_D is the Debye temperature, Ω is the average atomic volume per atom, h is Planck's constant, ν is the average speed of sound given by a weighted harmonic mean of the longitudinal and transverse speeds of sound, and Γ_{expt} is the experimental disorder scaling parameter. The experimental scaling parameter can be calculated by summing its mass Γ_M and strain Γ_S contributions. In this work, we assume the strain fluctuations are negligible compared to the mass difference of Mg and Zn. The mass disorder scaling parameter is given by weighted summation over all sub-lattice sites in the primitive unit cell:

$$\Gamma_M = \frac{\sum_{i=1}^{n} c_i \left(\frac{\bar{M}_i}{\bar{\bar{M}}}\right)^2 f_i^{k1} f_i^{k2} \left(\frac{M_i^1 - M_i^2}{\bar{M}_i}\right)^2}{(\sum_{i=1}^{n} c_i)} \tag{5.4}$$

where M represents mass, i is the indexed sub-lattice site, c_i is the relative degeneracy of the sub-lattice c, f_i^k is the occupational filling fraction of sub-lattice site i of atom type "k", $\bar{M}_i$ represents the average mass atomic mass of an atom on site i and is given by $\bar{M}_i = \sum_k f_i^k M_i^k$, $\bar{\bar{M}}$ is the average atomic mass of all atoms in the compound and is given

by $\bar{\bar{M}} = \frac{\sum_{i=1}^{n} c_i \bar{M}_i}{(\sum_{i=1}^{n} c_i)}$. In this study, since the metal atoms (Zn or Mg) tetrahedrally bonded to the anion constitutes most of the disorder, these formulas simplify as follows:

$$\bar{\bar{M}} = 1/5[M_1^{Ca} + \ \times M_2^{Zn}(1-x) + 2M_2^{Mg}(x) + 2M_3^{Sb}]$$

$$\Gamma_M = \frac{1}{5}\left[0 + c_2\left(\frac{\bar{M}_2}{\bar{\bar{M}}}\right)^2 f_2^{Zn} f_2^{Mg}\left(\frac{M_2^{Zn} - M_2^{Mg}}{\bar{M}_2}\right)^2 + 0\right]$$

$$\Gamma_M = \frac{1}{5}\left[2x(1-x)\left(\frac{M_2^{Zn} - M_2^{Mg}}{\bar{\bar{M}}}\right)^2\right]$$

Where x is the occupational fraction of Mg on the transition metal site. Therefore with only inputs of lattice thermal conductivity and speeds sound of the two end members compounds, the lattice thermal conductivities of alloy compositions given between can be predicted (Figure 5.11). The Debye temperature was calculated using the speed of sound by $\theta_D = \frac{h\nu_m}{k}$, where the Debye frequency is given by $\nu_m = \left(\frac{3\delta}{4\pi}\right)^{1/3} \nu_s$, h is Plank's constant, k is Boltzmann's constant, δ is number density of atoms, and ν_s is the average speed of sound.

Table 5.2: Speeds of sound for $CaZn_2Sb_2$ and $CaMg_2Sb_2$

	ν_T (m/s)	ν_L (m/s)	ν_S (m/s)
$CaZn_2Sb_2$	2094	3903	2476
$CaMg_2Sb_2$	2716	4330	3101

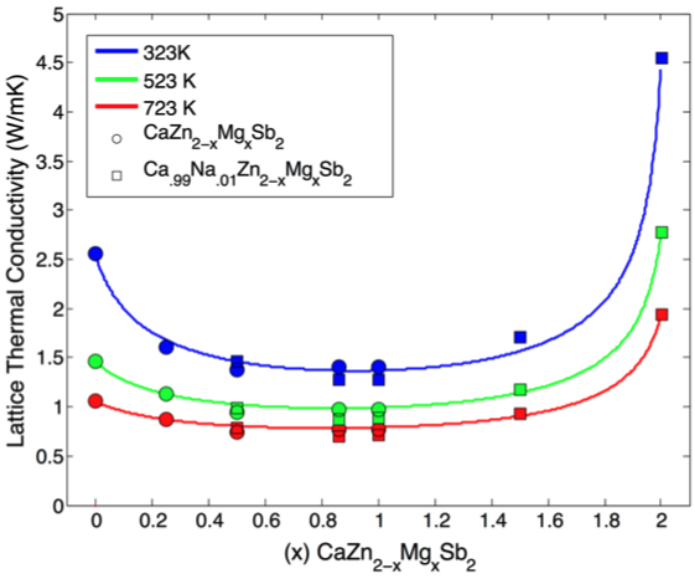

Figure 5.11: Lattice thermal conductivity vs Mg content. This shows a model based on simply the mass difference of the metals in the polyanionic layers can very accurately explain lattice thermal conductivity. Circles represent samples with nominal composition $CaZn_{2-x}Mg_xSb_2$. Squares represent samples with nominal composition $Ca_{0.99}Na_{0.01}Zn_{2-x}Mg_xSb_2$.

5.3.3. Thermomelectric Performance

Figure 5.12 shows the zT values of all the samples with respect to temperature. The samples with compositions of $Ca_{0.99}Na_{.01}Zn_{1.14}Mg_{0.86}Sb_2$ and $Ca_{0.99}Na_{0.01}ZnMgSb_2$ have the highest quality factors of all samples produced and correspondingly display the highest zT values. Using an effective mass model indicated that both samples were already optimally doped (Figure 5.13).

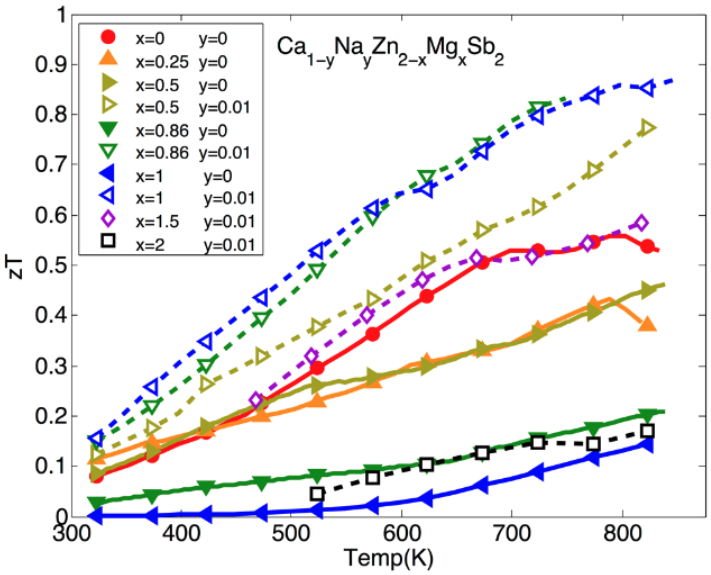

Figure 5.12: Thermoelectric figure of merit zT vs temperature for all the samples investigated.

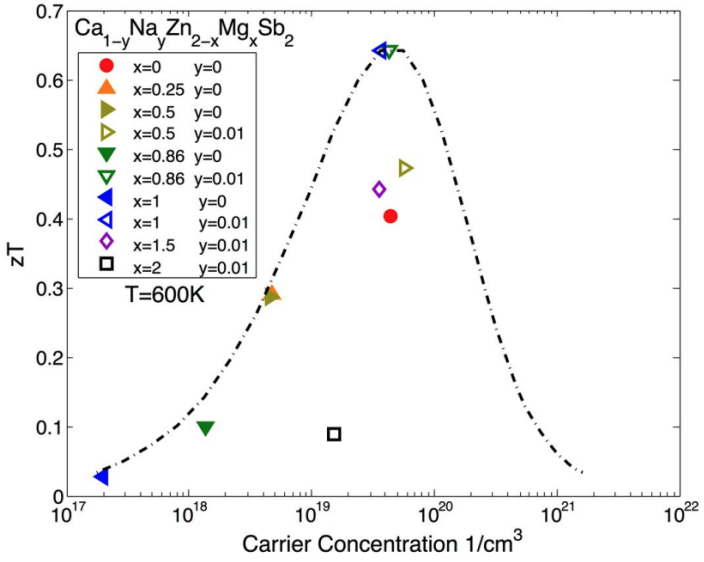

Figure 5.13: zT vs carrier concentration at 600 K for all samples measured. The calculated curve is based on the sample $Ca_{0.99}Na_{0.01}MgZnSb_2$ that has a dimensionless quality factor .218 and an effective mass of 1 m_e.

5.4. Conclusion

We prepared a number of solid solution of the Zintl compounds $CaZn_2Sb_2$ and $CaMg_2Sb_2$ crystallizing in the $CaAl_2Si_2$ structure. The thermoelectric properties of Na-doped $CaMg_2Sb_2$ were investigated for the first time in this study. An effective mass analysis finds a step like function with regards to composition, indicating transport is changing from one set of bands to another roughly at the composition $CaMgZnSb_2$. We find the sample with composition $Ca_{0.99}Na_{0.01}ZnMgSb_2$ has the highest zT of 0.87 at 575 at optimum carrier concentration and due to the low lattice thermal conductivity reached. Herein, we also demonstrate how a Klemens type model taking into account disorder on the transition metal site can explain the lattice thermal conductivities of the alloyed compositions.

5.5. Methods

5.5.1. Sample Preparation

Samples of Ca1-yNay Zn2-xMgxSb2 (x = 0, .25, .5, .86, 1, 1.5,2) (y = 0, .01) were prepared via a high-energy ball mill using stoichiometric ratios of bulk Ca dendrites (99.99 % Sigma-Aldrich), Zn shot (99.99% Alpha Aesar), annealed Mg slugs (99.95% Alpha Aesar), Sb shot (99.999% Alpha Aesar), and Na sticks (99% Alpha Aesar). Starting elements were cut into small pieces and loaded into a steel ball-milling vial with two $\frac{1}{2}$ inch and four $\frac{1}{4}$ inch stainless steel balls. All samples were milled using a SPEX Sample Prep 800 Series Mixer/Mill for 3 90-minute periods in between which the contents of the vial were scraped in an inert atmosphere in order to ensure elements were reacting homogenously. Samples were consolidated using an induction heated rapid hot-press 39 under a flowing argon atmosphere within a $\frac{1}{2}$ in diameter high-density graphite die (POCO) into pellets

approximately 2 mm in thickness. Samples were pressed at 350 °C for 30 minutes to ensure any elemental zinc was fully reacted and then 700°C for 90 minutes at a pressure of 45 MPa. Resulting Samples were found to have densities exceeding 95%. All Samples are metallically shiny and relatively stable under ambient conditions.

5.5.2. Sample Characterization

XRD was performed on polished pellets using a Rigaku Dmax Powder X-Ray Diffractometer (45kV, 40 mA, Cu Kα radiation) with reflection geometry. Density of the samples was measured using the Archimedes' principle. Electronic transport measurements were measured under dynamic high vacuum up to 875 K with a ramp speed of 75 K/h. Resistivity and hall coefficients were measured concurrently using the Van Der Pauw technique with pressure-assisted molybdenum contacts equipped a 2T magnet[18]. Thermal diffusivity measurements were taken with a Netzch LFA 457 under purged flowing argon up to 875K with a ramp speed of 75 K/h. Thermal conductivity was calculated estimating heat capacity with the Dulong-Petit law. Seebeck coefficients were measured under dynamic high vacuum up to 875 K with a homebuilt system using Chromel-Nb thermocouples[17]. All Samples were investigated in pellet form with Seebeck and thermal diffusivity being measured out of plane and resistivity and Hall coefficient being measured in plane direction. From the analysis of X-ray diffraction data, there appears to be no form of texturing or preferred orientation after pressing.

CHAPTER 6

Understanding Defects Effects on Electronic Scattering: $Mg_{3-x}Yb_xSb_{1.5}Bi_{.5}$

(This chapter contains content reproduced with permission from the Journal of Materials Chemistry A, DOI: 10.1039/C9TA11328B)

6.1. Introduction

Mg_3Sb_2 can be thought of as a special case of the layered $CaAl_2Si_2$ (AB_2X_2) Zintl phase crystal structure in which the A and B sites are both composed of Mg, which we'll refer to as Mg(1) and Mg(2) respectively[160]. The Mg(2) site is tetrahedrally coordinated with Sb and forms the B_2X_2 layer. The Mg(1) site forms the intralayer site and is octahedrally coordinated with Sb atoms. Though Mg_3Sb_2 can be visualized through the layered $CaAl_2Si_2$ structure, Zhang et al. carefully showed the "layered" term may not be appropriate. This is because the Mg(1) and Mg(2) sites have similar Bader charge and bond strength with Sb, making the calculated material properties isotropic[160].

While the term layered may not be apt for Mg_3Sb_2, the similar size and charges on Mg(1) and Mg(2) might play a role in why the material's electronic properties are unique within this crystal structure. Zhang et al. first pointed out that the conduction band minimum states of Mg_3Sb_2 are made out of Mg(1) s and Mg(2) s and p states[161]. Sun et al., took this a step further and showed that the highly degenerate U* band (Nv = 6) was made up of covalent interactions between the Mg(1) and Mg(2) atoms[162].

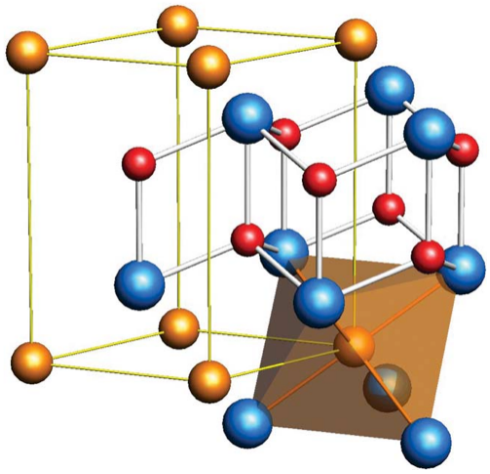

Figure 6.1: Crystal Structure of Mg_3Sb_2. Gold atoms represent the octahedrally coordinated Mg(1) atoms, red atoms represent the tetrahedrally coordinated Mg(2) atoms, and blue atoms represent Sb.

This interaction can be demonstrated from first principles electronic structure and crystal orbital Hamilton population (COHP) calculations (see Figure 6.2). The conduction band minima at the non high-symmetry U*-point lies in the Γ-A-L-M plane (see 2D Fermi-Energy contour plot in Figure 6.2b). The k-resolved COHP for the conduction band in this 2D plane reveals Mg (1)s - Mg(2)s as the dominant interaction in the vicinity of U*-point. These conduction band states exhibit a significant bonding interaction between 3s levels of Mg(1) and Mg(2) as indicated by the negative values COHP values (see blue regions in Figure 6.2) for states close to U*. Sun went on to show that changing the octahedral site to another atom such as Yb or Ca computationally resulted in a more ionic interaction between the octahedral atom and the Mg_2Sb_2 layer. In these XMg_2Sb_2 compounds the conduction band minimum is moved to the higher symmetry M point (Nv = 3), which has less band degeneracy[151;162;56].

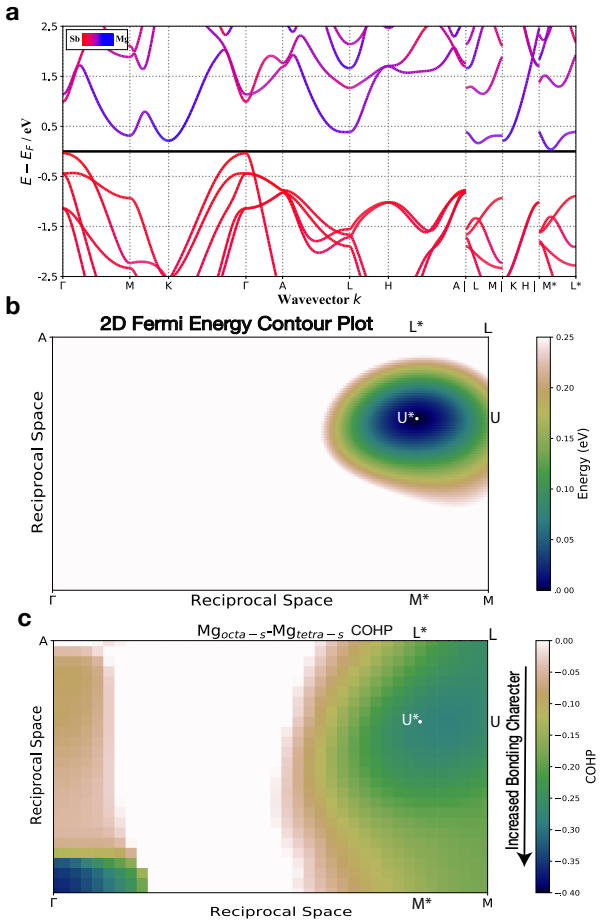

Figure 6.2: (a) Atom-projected electronic band structure of Mg3Sb2. (b) Band energy contour plot up to 0.25 eV inside the conduction band for Mg3Sb2 in the Γ-A-L-M plane of the reciprocal space. (c) The k-resolved projected COHP for the interaction between Mg_{octa} and Mg_{tetra} in Mg_3Sb_2. The color scale varies over the COHP range [-0.4,0] and saturating for positive values. This range of values was chosen to emphasize the presence of bonding interaction for states lying close to the conduction band minima.

Mg3Sb2 can form solid solutions with other compounds of the same crystal structure, with solubilities varying to differing degrees. Mg3Bi2 is commonly alloyed with Mg_3Sb_2 and is used to lower the material's lattice thermal conductivity and increase its weighted

mobility[163;164]. Besides studies with Bi, Sun et al. calculated the valley degeneracy of Mg_3Sb_2, could be increased by alloying Yb or Ca onto the octahedral Mg site, moving the conduction band at U* up slightly in energy to be aligned with the band at M[162].

Beyond this computational alloying study, there have been numerous papers published both computationally[165;166] and experimentally[167;161;168;169] testing the impact of different doping techniques. The main focus of which is the dopant's dopability (i.e. the maximum soluble amount of a dopant which donates charge carriers). However, in many of these dopant and alloying papers the type of states that make up the conduction band character is often overlooked. Disrupting these states can lead to additional short ranged potential scattering[170;171] or alloy scattering[26], decreasing the materials performance.

Herein we investigate the properties of $Mg_{3.125-x}Yb_xSb_{1.5}Bi_{0.5}Te_{0.01}$ and show a decrease in the mobility of the material as more Yb is added from disrupting the Mg(1)-Mg(2) interaction that make up the conduction band. Additionally, we show that this reduction can be well explained via an alloy scattering model. Finally, we show that while a sample's mobility is decreased, Yb alloying does benefit a sample's high temperature stability.

6.2. Results

6.2.1. X-Ray Diffraction

X-Ray Diffraction patterns for samples created of Mg_3Sb_2 alloyed with Bi and Yb and doped with Te are shown in Figure 6.3. From XRD we can identify no visible impurity phases. Figure 6.4 shows the lattice parameters obtained from diffraction pattern of samples, with the dashed line showing the lattice parameters expected assuming a weighted average contribution from the four compounds that make up the solid solution. Both a

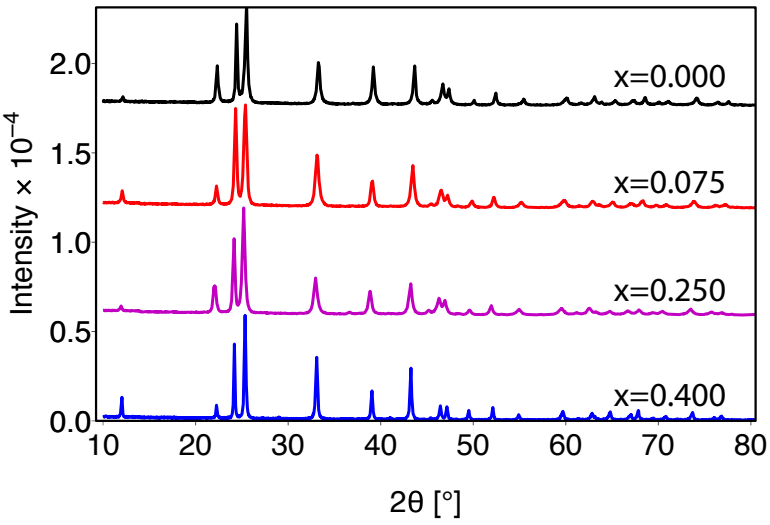

Figure 6.3: x-ray diffraction for $Mg_{3.125-x}Yb_xSb_{1.5}Bi_{0.5}Te_{0.01}$ samples.

and c rise linearly with increased Yb content up to x = 0.25, where beyond this composition the solubility of Yb into the structure has likely been exceeded. This is reflected by the x = 0.4 sample's lattice parameters deviating slightly from the predicted line. Based on this data we can assume a solid solution is obtained at least until composition x = 0.25.

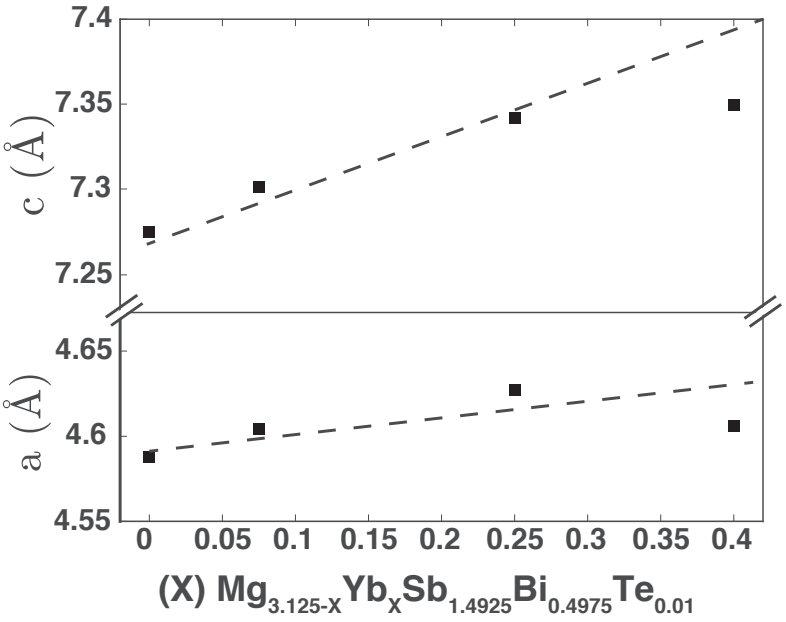

Figure 6.4: Lattice parameters a and c for $Mg_{3.125-x}Yb_xSb_{1.5}Bi_{0.5}Te_{0.01}$ samples determined from X-ray diffraction analysis. The dashed line is a projected lattice parameter given by a compositionally weighted fit of the lattice parameters of Mg_3Sb_2[22], Mg_3Bi_2[23], $YbMg_2Sb_2$[24], and $YbMg_2Bi_2$[25] taken from ICSD.

6.2.2. Transport

Table 6.1 shows how the Hall carrier concentration (defined as simply 1/RH, the Hall resistance) of Te doped Mg3Sb1.5Bi0.5 is reduced as Yb is alloyed in. Additionally, table 6.1 shows the Hall mobility and experimental density of states effective mass calculated from the Hall carrier concentration and Seebeck coefficient[91] for the samples that are unaffected by bipolar conduction. The x=0.2 and x=0.4 samples clearly show bipolar effects in both Seebeck and electrical conductivity so the actual free electron concentration is likely to be less than the measured nH) There is barely an increase in effective mass observed

to support the claim that adding Yb produces additional conducting states, however a benefit of these states to the materials' weighted mobility (Figure 4) is not seen.

Table 6.1: Hall (n-type) Carrier Concentrations (n_H), Hall Mobilities (μ_H), and density of states effective mass of samples $Mg_{3.125-x}Yb_xSb_{1.4925}Bi_{0.4975}Te_{0.01}$ created for this study measured at 400K.

x	$n_H(1/cm^3)$	$\mu_H(cm^2/Vs)$	$m^*_{DOS}(m_e)$
0.0	2.4E+19	90	1.1
0.075	2.3E+19	55	1.1
0.25	1.7E+19	20	
0.4	9E+18		

Thermoelectric transport studied (Fig. 6.5) follows a trend that is expected given the decreasing carrier concentration with Yb content. The Seebeck coefficient increases as Yb is alloyed is due to the reduction of carrier concentration, and the conductivity decreases. The thermal conductivity decreases with the addition of Yb, which is due in part to the reduction in the electronic portion of thermal conductivity. Additionally this decreasing trend can be attributed to a reduction in the lattice portion of thermal conductivity as Yb is added due to a reduction in speed of sound computationally predicted[162] as well as alloy scattering of phonons[154;172;156;159;157].

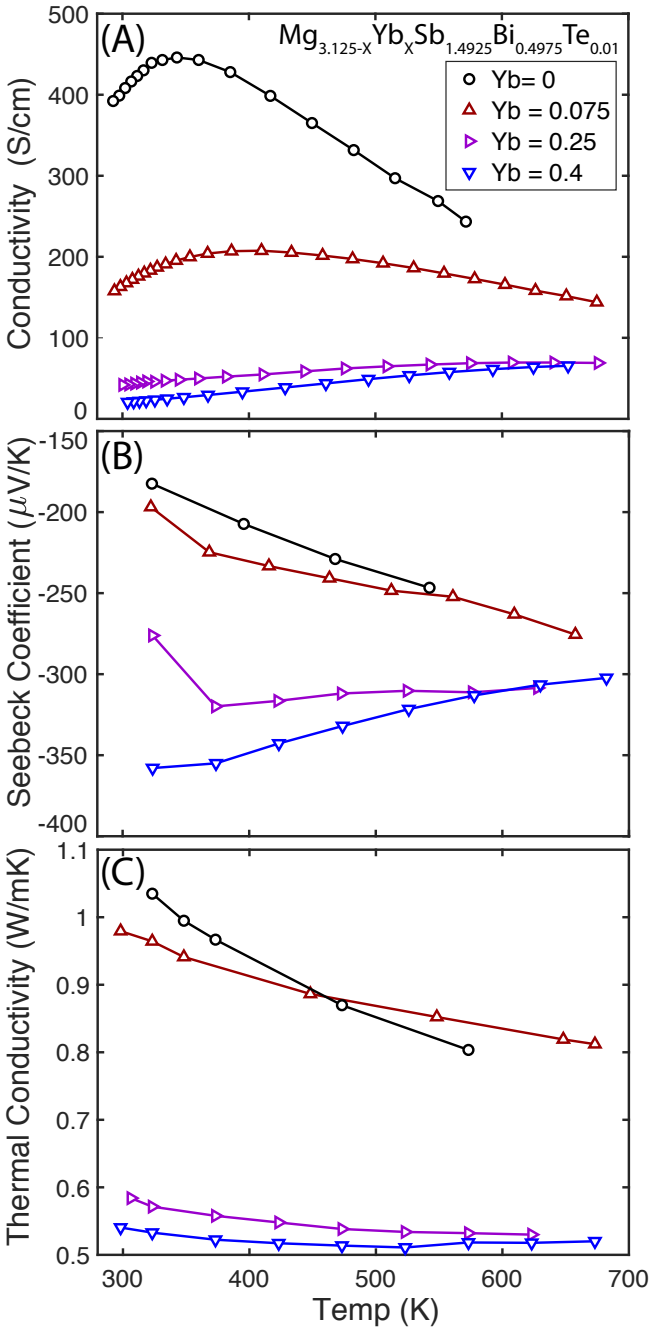

Figure 6.5: (A) Conductivity, (B) Seebeck coefficient, and (C) Thermal conductivity data for samples analyzed for this study.

6.3. Discussion

To compare transport in the samples we extracted the weighted mobility from a sample's Seebeck and conductivity data following[91;53;173]. Weighted mobility makes up the numerator of a materials quality factor and can be used to obtain a material's the peak power factor with changing carrier concentration[53]. As Yb is alloyed into the material we see a resulting decrease in its weighted mobility that follows the trend expected due to alloy scattering. As pointed out by Sun et al[162], the Mg(1) -Mg(2) interaction is important in the electronic states at the conduction band minimum in Mg_3Sb_2. This explains why disrupting the Mg(1) sites by replacing Mg with Yb has a large detrimental effect. This reduction in mobility is not seen[163;164] with alloying Bi on the anion site, which is expected because anions do not contribute much to the conduction band states.

To study the reduction in mobility in samples, an alloy scattering model is employed, which Wang et al. used to study the PbTe-PbSe alloy[26]. In this model we assume the total relaxation time of an electron is given by Matthiessen's rule such that:

$$\tau_{total}^{-1} = \tau_{pure}^{-1} + \tau_{alloy}^{-1}$$

Or equivalently:

$$\mu_{total}^{-1} = \mu_{pure}^{-1} + \mu_{alloy}^{-1}$$

Where the scattering time from an alloy takes the form:

$$\tau_{0(alloy)} = \frac{8\hbar^4}{3\sqrt{2}\pi\Omega x(1-x)U^2 m_b^{*3/2}(k_B T)^{1/2}}$$

In which Ω is the volume per atom, x is the concentration faction of the alloying atom, m_b^* is the density of states mass for a single band, and U is the alloy scattering potential.

While the initial compound is already an alloy of Mg_3Sb_2 and Mg_3Bi_2, we can separate Yb's contribution to alloy scattering by taking the 25% Mg3Bi2 as giving a "pure" weighted mobility. The reduction in weighted mobility due to alloy scattering therefore takes the form:

$$\mu_{w(alloy)} = \mu_{0(alloy)} \left(\frac{m^*_{DOS}}{m_e}\right)^{\frac{3}{2}} = \frac{8\hbar^4 N_v}{m_I^* 3\sqrt{2}\pi\Omega x(1-x)U^2 m_e^{*3/2}(k_B T)^{1/2}}$$

Where m^*_{DOS} is the density of states effective mass, m^*_I is the inertial effective mass and N_v is the degeneracy of the band(s) involved in transport. Using a $N_v = 6$ given by the degeneracy of the CB1 pocket, and using Zhang et al.'s calculated inertial masses isotropically averaged to 0.3 m_e[174] we find an alloy scattering potential of 2.2 eV gives a curve matching the experimental data at a range of different temperatures (Figure 6.6). The reduction of carrier concentration as Yb is alloyed into the crystal is likely from cation site vacancies in the crystal, which have the effect of lowering the Te dopability in the alloy. Pomrehn et al. showed in AZn_2Sb_2 (A = Ca, Sr, Eu, Yb) as the A site was changed the vacancy formation energy of the A site also changed, with $YbZn_2Sb_2$ being the most susceptible to the formation of vacancies[139]. While the compound studied here contained Mg instead of Zn, the experimental data suggests a similar effect might exist as Yb is alloyed into Mg_3Sb_2.

While the mobility of Mg3Sb2 was decreased with alloying Yb, long term hall tests (Figure 6.7) show adding Yb appears to increase its high temperature stability. We speculate this change is due to a reduction of the diffusivity of Mg within the material after adding the larger Yb atom as it is also observed in a La-doping study[74]. Regardless

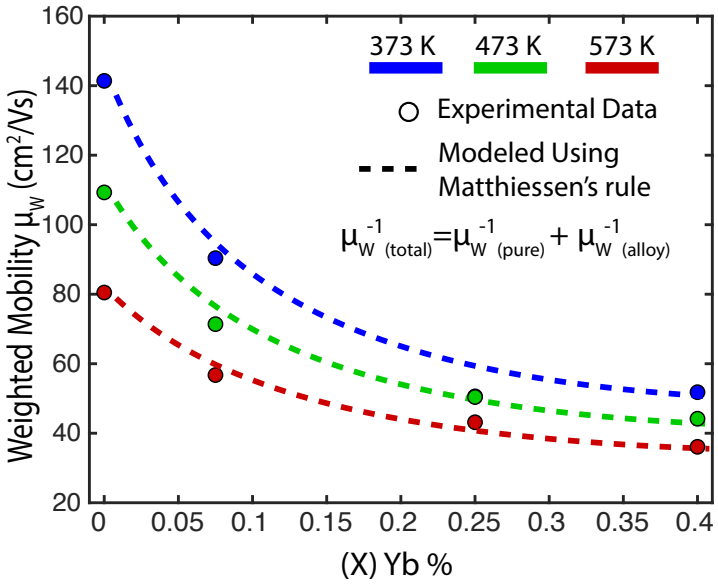

Figure 6.6: Weighted mobility (μ_W) of samples vs the Yb content at 373 K (blue), 473 K (green) , and 573 K (red). Experimental values are given by data points. An Alloy scattering model was employed to estimate the reduction in weighted mobility, (dashed lines). The alloy scattering potential term[26] U = 2.2 eV was used to estimate the reduction in weighted mobility.

of cause, this observed increased stability provides a possible route for Mg_3Sb_2 compounds to be used at higher temperatures.

The zT of the samples (Figure 6.8) follows the same trend as weighted mobility with the zT decreasing with increasing Yb alloying. Yb alloying does decrease the lattice thermal conductivities of the samples studied, which is good for thermoelectric performance. However this decrease is not substantial enough to overcome the decrease in mobility from disrupting the Mg(1)-Mg(2) interaction.

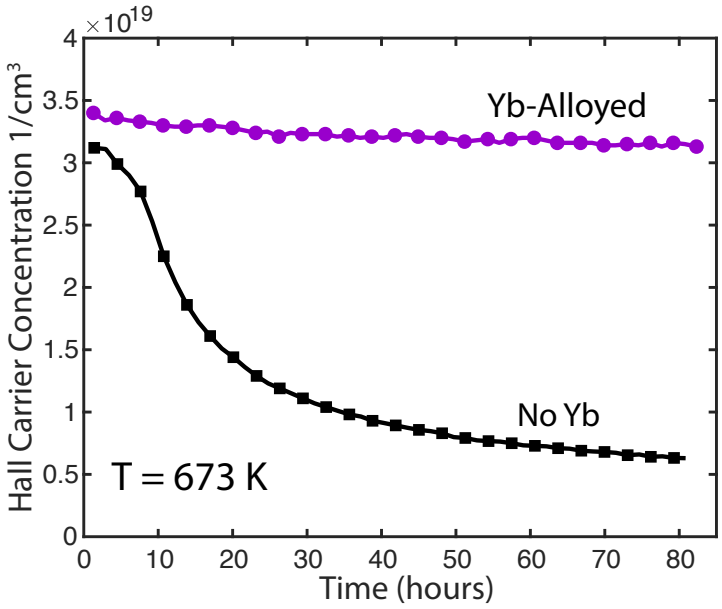

Figure 6.7: Time dependency of the Hall carrier concentration of a Yb alloyed sample (Yb0.75Mg3.05Sb1.4925Bi0.4975Te0.01) and a sample without Yb present (Mg3.125Sb1.4925Bi0.4975Te0.01) measured under dynamic vacuum that removed Mg vapor at 673 K.

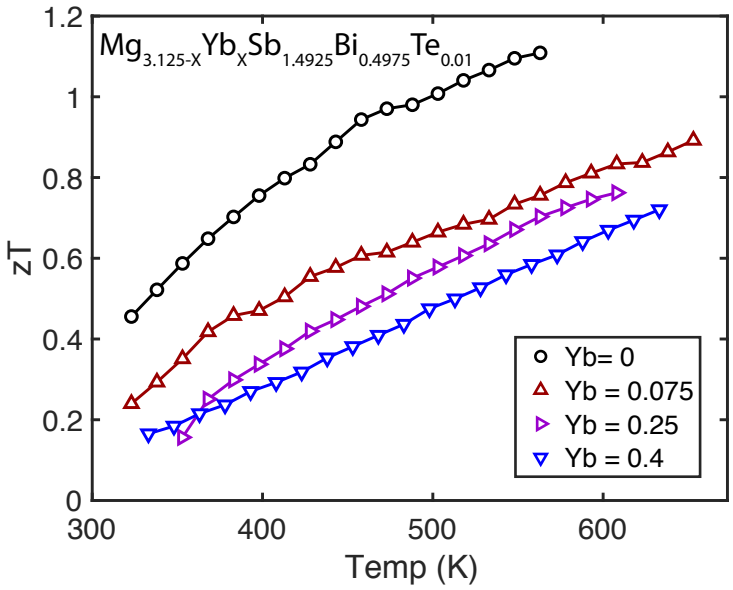

Figure 6.8: zT of samples Mg3.125-xYbxSb1.4925Bi0.4975Te0.01

6.4. Conclusion

In conclusion, alloying Yb on to the cation site of $Mg_{3.05}Sb_{1.4925}Bi_{0.4975}Te_{0.01}$ results in a reduction of the materials mobility due to alloy scattering. Alloying on the cation site appears to be detrimental not only because the conduction band is normally dominated by cations23 but also because Yb disrupts the Mg(1)-Mg(2) interaction that is responsible for locating the conduction band minimum at the high valley degeneracy point U*. Although we see a reduction of zT with Yb alloy, the high temperature stability of the material increases with its addition.

When we compare anion site alloying with cation site alloying the importance of the Mg(1)-Mg(2) interaction becomes even more clear. Both cation site alloying with Yb and anion site alloying with Bi decreases thermal conductivity, and both alloying cases are predicted to create a band convergence effect should improve the weighted mobility. However the cation-site disorder disrupts the Mg(1)-Mg(2) interaction much more strongly than the anion-site disorder. Thus alloying on the anion site, which is less effected by the additional scattering, can benefit from the lower thermal conductivity and band convergence, producing higher zT.

6.5. Methods

6.5.1. First Principles Calculations

The density functional theory (DFT) calculation[175]in this study were performed using Vienna ab initio simulation package (VASP)[176]. We have used PerdewBurke Ernzerhof (PBE) formulation of the exchange correlation energy functional derived under a gradient-generalized approximation (GGA)[134]. Plane-wave basis sets truncated at a constant

energy cutoff of 390 eV were used, as were Γ-centered k-point meshes with a density of 8000 k-points per reciprocal atom (KPPRA). All structures were relaxed with respect to cell vectors and their internal degrees of freedom until forces on all atoms were less than 0.1 eV/nm. The k-resolved crystal orbital Hamilton populations (COHPs) calculations were performed using the version 3.2.0 of the LOBSTER software.[177;178;179]

6.5.2. Sample Preparation

Samples of $Mg_{3.125-x}Yb_xSb_{1.4925}Bi_{0.4975}Te_{0.01}$ (x = 0, 0.075, 0.25, 0.4) were prepared via a high-energy ball mill using stoichemetric ratios of Mg turning (99.95% Alpha Aesar), Yb chunk (99.5% Alpha Aesar), Sb shot (99.999% 5N Plus), Bi shot (99.999% 5N Plus), Te shot (99.999 % 5N Plus). Excess Mg was used in all samples in order to suppress the formation of electron killing Mg vacancies. Starting elements were loaded into a steel ball milling vial in an argon dry glove box. Samples were then milled for 2 90-minute periods using a SPEX Sample Prep 800 Series Mixer/Mill. The powder from this milling process was consolidated using an induction heated rapid hot-press[68] under a flowing argon atmosphere within a $\frac{1}{2}$ inch diameter high-density graphite die (POCO) into pellets approximately 1.5 mm in thickness. Samples were pressed at 800 °C for 20 minutes at 45 MPa. Resulting samples were found to have densities exceeding 95% theoretical densities.

6.5.3. Sample Characterization

X-ray diffraction was performed on polished pellets using a STOE STADI MP with pure Cu Kα 1 radiation in reflection geometry, followed by scanning electron microscopy with

a Hitachi S-3400N-II . Densities of samples were measured geometrically and then confirmed with the Archimedes Principle. Resistivity and Hall coefficients were measured concurrently using a van der Pauw technique with pressure-assisted molybdenum contacts equipped with a 2T magnet[18]. Thermal diffusivity measurements were taken with a Netzsch LFA 457 under purged flowing argon, and the thermal conductivity was calculated using heat capacity from Agne et al[84]. Seebeck coefficient were measured under dynamic high vacuum with a homebuilt system using Chromel-Nb thermocouples[17]. All samples were investigated in pellet form with Seebeck and thermal diffusivity measured out of plane and resistivity and Hall coefficient being measured in the in-plane direction. The thermal stability of materials studied were measured via the change in Hall carrier concentration as a function of time at elevated temperatures[74].

CHAPTER 7

Conclusion and Future Prospects

I hope someone having read this work will have taken away that point defects studies can be used as a lens to ask fundamental questions about physics, chemistry, and material science. In the 2nd and 3rd chapter of this thesis I gave examples of how point defects can be controlled using equilibrium thermodynamics. Then in the 4th chapter I showed how changing the defect concentration in $Yb_{14}MgSb_{11}$ lead to a greater understanding of the unusual transport in the material and its relationship to the band structure. In the 5th chapter I gave an example of how point defects can change the band structure of $CaZn_2Sb_2$, with the observation of a rapid increase in the solid solutions effective mass as Mg was substituted onto the Zn site. Then finally in the 6th chapter I showed how alloying $YbMg_2Sb_{1.5}Bi_{0.5}$ and $Mg_3Sb_{1.5}Bi_{0.5}$ lead to a significant increase in electronic scattering that could be explained through the bonding states of that material.

Looking at this work done here and techniques developed there are a number of questions and follow up studies that clearly present themselves. First given the relatively new understanding of how to control defects with phase boundary mapping and saturation annealing, future scientist should take a second look at materials that were predicted to be excellent thermoelectric materials through ab initio models, but were ultimately found undopable in the lab. Choosing the right dopant and phase space can be aided by computationalists computing defect formation energy diagrams for experimentalists to utilize.

Saturation annealing presents an experimental method for turning off and on free electrons in the some materials such as Mg_3Sb_2 with relatively short anneals. This gives scientists a way to probe how the properties of a material change with and without free carriers. A follow up study I have already been involved in, but not discussed in this document, is is how having free carriers impacts the perceived lattice thermal conductivity of Mg_3Sb_2[180]. There are numerous other properties one could choose to look at though. For example, does the existence of free carriers change the bond strength in a material? One could potentially use the speed of sound or elastic modulus as a proxy to determine this. Do dislocations form more readily when the number of free carriers are increased in a material? One could look at ductility differences to get at this property. Does the sublimation rate of a material increase with the existence of free carriers? By adding free carriers, which increases the energy of the system, does the formation energy, which is related to a materials vapor pressure, increase? Of course I'm overlooking a number of subtleties and considerations when asking these questions, but having this tool to control a material's defect concentration and carrier concentration opens up a lot of doors for exploration.

Regarding the 4th chapter on $Yb_{14}MgSb_{11}$ there are still a number of questions that remain unawsered. For example why doesn't the carrier concentration and Zintl valence count for free carriers match in $Yb_{14}MgSb_{11}$ (Figure 4.3)? A possible explanation for this is the existence of intrinsic defects or change in valence states that compensate the expected electron count. This possibility could be explored with saturation annealing or phase boundary mapping to see if the material's carrier concentration, and therefore defect concentration changes. Another question regarding this compound is if higher

carrier concentrations are achievable and if these carrier concentrations lead to enhanced zT as our model predicts (Figure 4.7). Finally the the model that was developed for the electronic properties for $Yb_{14}MgSb_{11}$ predicts electronic thermal conductivities roughly equivalent to the material's total thermal conductivity (Figure 4.6). This implies that phonons in the material don't conduct heat or that we are in some way overestimating the material's electronic thermal conductivity. When looking through the literature this effect is surprisingly not uncommon, but has yet to have definitively been answered. When Weidemann and Franz were looking at the electrical and thermal conductivities of metals they arrived at a correlation between the total thermal conductivity and total conductivity. The theoretical relationship between how much heat and charge free electrons carry was later determined and found to quite closely match the correlation that Weidemann and Franz had noticed.[181] This would therefore imply that the phonons in metals carry a negligible amount of heat. While some have theorized electron phonon scattering decreases the phonon conductivity, or that electron-electron scattering decreases the actual Lorenz number in a material there hasn't been an experimental study that shows definitely what is occurring.

The final unanswered question I'll write comes form chapter 5 of this thesis. Initially the goal of this study was to create band convergence in a $CaZn_{2-x}Mg_xSb_2$ sample, which would have enhanced mobility and therefore higher zT. While this study did observe a switching of the bands, it did not show that the material's mobility increased. A possible reason for this is that the band extrema were located at the same k-point and therefore possibly more subject to scattering. A theoretical study of scattering rates would certainly

be useful to the thermoelectric community in order to determine when convergence is beneficial and when it is not.

References

[1] A. A. Nayeb-Hashemi and J. B. Clark, "The mg-sb (magnesium-antimony) system," *Bulletin of Alloy Phase Diagrams*, 1984.

[2] G. Grube, "Alloys of magnesium with cadmium, zinc, bismuth and antimony," *The Journal of Physical Chemistry*, vol. 10, pp. 587–592, 1906.

[3] E. Abel, O. Redlich, and F. Spausta, "Über das ternäre system blei-antimon-magnesiumantimonid," *Zeitschrift für anorganische und allgemeine Chemie*, vol. 190, no. 1, pp. 79–89, 1930.

[4] G. Grube, L. Mohr, and R. Bornhak, "Elektrische leitfähigkeit und zustandsdiagramm bei binären legierungen. 10. mitteilung. das system magnesium-wismut," *Zeitschrift für Elektrochemie und angewandte physikalische Chemie*, vol. 40, no. 3, pp. 143–150, 1934.

[5] A. A. Nayeb-Hashemi and J. B. Clark, "The bi-mg (bismuth-magnesium) system," *Bulletin of Alloy Phase Diagrams*, 1985.

[6] C. Freysoldt, B. Grabowski, T. Hickel, J. Neugebauer, G. Kresse, A. Janotti, and C. G. Van de Walle, "First-principles calculations for point defects in solids," *Reviews of Modern Physics*, vol. 86, no. 1, pp. 253–305, 2014.

[7] S. Ohno, K. Imasato, S. Anand, H. Tamaki, S. D. Kang, P. Gorai, H. K. Sato, E. S. Toberer, T. Kanno, and G. J. Snyder, "Phase boundary mapping to obtain n-type Mg_3Sb_2-based thermoelectrics," *Joule*, vol. 2, no. 1, pp. 141 – 154, 2018.

[8] C. Wang, Y. Xu, S. Yang, H. Jiang, J. Li, J. Zhu, S. Yang, and X. Liu, "Experimental determination of phase equilibria in the sn-zn-sb system," *Journal of Phase Equilibria and Diffusion*, vol. 36, no. 4, pp. 350–356, 2015.

[9] A. A. Shabaldin, L. V. Prokof'eva, P. P. Konstantinov, A. T. Burkov, and M. I. Fedorov, "Acceptor impurity of copper in znsb thermoelectric," *Materials Today: Proceedings*, vol. 2, no. 2, pp. 699–704, 2015.

[10] P. H. Michael Bottger, S. Diplas, E. Flage-Larsen, O. Prytz, and T. G. Finstad, "Electronic structure of thermoelectric zn-sb," *J Phys Condens Matter*, vol. 23, no. 26, p. 265502, 2011.

[11] A. F. May and G. J. Snyder, "Introduction to modeling thermoelectric transport at high temperatures," in *Materials, preparation, and characterization in thermoelectrics*, pp. 11–1, CRC Press, 2017.

[12] J. Zhang, L. Song, S. H. Pedersen, H. Yin, L. T. Hung, and B. B. Iversen, "Discovery of high-performance low-cost n-type Mg_3Sb_2-based thermoelectric materials with multi-valley conduction bands," *Nature communications*, vol. 8, p. 13901, 2017.

[13] J. Shuai, J. Mao, S. Song, Q. Zhu, J. Sun, Y. Wang, R. He, J. Zhou, G. Chen, D. J. Singh, and Z. Ren, "Tuning the carrier scattering mechanism to effectively improve the thermoelectric properties," *Energy & Environmental Science*, vol. 10, no. 3, pp. 799–807, 2017.

[14] T. Kanno, H. Tamaki, H. K. Sato, S. D. Kang, S. Ohno, K. Imasato, J. J. Kuo, G. J. Snyder, and Y. Miyazaki, "Enhancement of average thermoelectric figure of merit by increasing the grain-size of $Mg_{3.2}Sb_{1.5}Bi_{0.49}Te_{0.01}$," *Applied Physics Letters*, vol. 112, no. 3, p. 033903, 2018.

[15] "Marlow industries, private communication, unpublished,"

[16] J. J. Kuo, S. D. Kang, K. Imasato, H. Tamaki, S. Ohno, T. Kanno, and G. J. Snyder, "Grain boundary dominated charge transport in Mg_3Sb_2-based compounds," *Energy & Environmental Science*, vol. 11, no. 2, pp. 429–434, 2018.

[17] S. Iwanaga, E. S. Toberer, A. LaLonde, and G. J. Snyder, "A high temperature apparatus for measurement of the seebeck coefficient," *Review of Scientific Instruments*, vol. 82, no. 6, p. 063905, 2011.

[18] K. A. Borup, J. De Boor, H. Wang, F. Drymiotis, F. Gascoin, X. Shi, L. Chen, M. I. Fedorov, E. Müller, B. B. Iversen, and G. J. Snyder, "Measuring thermoelectric transport properties of materials," *Energy & Environmental Science*, vol. 8, no. 2, pp. 423–435, 2015.

[19] E. S. Toberer, C. A. Cox, S. R. Brown, T. Ikeda, A. F. May, S. M. Kauzlarich, and G. J. Snyder, "Traversing the metal-insulator transition in a zintl phase: Rational enhancement of thermoelectric efficiency in yb14mn1xalxsb11," *Advanced Functional Materials*, vol. 18, no. 18, pp. 2795–2800, 2008.

[20] J. W. Zhang, L. R. Song, G. K. H. Madsen, K. F. F. Fischer, W. Q. Zhang, X. Shi, and B. B. Iversen, "Designing high-performance layered thermoelectric materials through orbital engineering," *Nature Communications*, vol. 7, 2016.

[21] Z. M. Gibbs, F. Ricci, G. Li, H. Zhu, K. Persson, G. Ceder, G. Hautier, A. Jain, and G. J. Snyder, "Effective mass and fermi surface complexity factor from ab initio band structure calculations," *npj Computational Materials*, vol. 3, no. 1, p. 8, 2017.

[22] M. Martinez-Ripoll, A. Haase, and G. Brauer, "The crystal structure of -mg3sb2," *Acta Crystallographica Section B: Structural Crystallography and Crystal Chemistry*, vol. 30, no. 8, pp. 2006–2009, 1974.

[23] E. Wigner, "Zeitschrift fur physikalische chemie-abteilung b-chemie der elementarprozesse," *Aufbau der Materie*, vol. 19, pp. 203–216, 1932.

[24] F. Wartenberg, C. Kranenberg, R. Pocha, D. Johrendt, A. Mewis, R.-D. Hoffmann, B. D. Mosel, and R. Poettgen, "Neue pnictide im caal2si2-typ und dessen existenzgebiet/new pnictides with the caal2si2 type structure and the stability range of this type," *Zeitschrift für Naturforschung B*, vol. 57, no. 11, pp. 1270–1276, 2002.

[25] A. F. May, M. A. McGuire, D. J. Singh, R. Custelcean, and G. E. Jellison Jr, "Structure and properties of single crystalline camg2bi2, eumg2bi2, and ybmg2bi2," *Inorganic chemistry*, vol. 50, no. 21, pp. 11127–11133, 2011.

[26] H. Wang, A. D. LaLonde, Y. Pei, and G. J. Snyder, "The criteria for beneficial disorder in thermoelectric solid solutions," *Advanced Functional Materials*, vol. 23, no. 12, pp. 1586–1596, 2013.

[27] R. Hoffmann, "A chemist's view of bonding in extended structures," 1988.

[28] W. Kossel, "Über molekülbildung als frage des atombaus," *Annalen der Physik*, vol. 354, no. 3, pp. 229–362, 1916.

[29] G. N. Lewis, "The atom and the molecule.," *Journal of the American Chemical Society*, vol. 38, no. 4, pp. 762–785, 1916.

[30] R. Nesper, "The zintl-klemm concept–a historical survey," *Zeitschrift für anorganische und allgemeine Chemie*, vol. 640, no. 14, pp. 2639–2648, 2014.

[31] I. Langmuir, "The arrangement of electrons in atoms and molecules.," *Journal of the American Chemical Society*, vol. 41, no. 6, pp. 868–934, 1919.

[32] W. H. Bragg and W. L. Bragg, "The reflection of x-rays by crystals," *Proceedings of the Royal Society of London. Series A, Containing Papers of a Mathematical and Physical Character*, vol. 88, no. 605, pp. 428–438, 1913.

[33] S. Goldschmidt, R. R. Wolff, L. Engel, and E. Gerisch, "Über den abbau des ovalbumins durch hypobromit.(9. mitteilung über proteine.)," *Hoppe-Seyler´ s Zeitschrift für physiologische Chemie*, vol. 189, no. 5-6, pp. 193–217, 1930.

[34] W. Hume-Rothery, "Xxx. a note on the connexion between chemical valency, electron grouping, and crystal structure," *The London, Edinburgh, and Dublin Philosophical Magazine and Journal of Science*, vol. 3, no. 14, pp. 301–305, 1927.

[35] W. Hume-Rothery, "Xcv. the metallic state," *The London, Edinburgh, and Dublin Philosophical Magazine and Journal of Science*, vol. 4, no. 25, pp. 1017–1045, 1927.

[36] W. Hume-Rothery, "Viii. the crystal structures of the elements of the b sub-groups and their connexion with the periodic table and atomic structures," *The London, Edinburgh, and Dublin Philosophical Magazine and Journal of Science*, vol. 9, no. 55, pp. 65–80, 1930.

[37] E. Zintl and W. Dullenkopf, "Polyantimonide, polywismutide und ihr übergang in legierungen: 3. mitteilung über metalle und legierungen," *Zeitschrift für Physikalische Chemie*, vol. 16, no. 1, pp. 183–194, 1932.

[38] E. Zintl and G. Brauer, "Über die valenzelektronenregel und die atomradien unedler metalle in legierungen," *Zeitschrift für Physikalische Chemie*, vol. 20, no. 1, pp. 245–271, 1933.

[39] E. Zintl, "Intermetallische verbindungen," *Angewandte Chemie*, vol. 52, no. 1, pp. 1–6, 1939.

[40] U. Müller, "Polyanionic and polycationic compounds. zintl phases," *Inorganic Structural Chemistry*, pp. 116–138, 1991.

[41] R. Nesper, "Structure and chemical bonding in zintl-phases containing lithium," *Progress in solid state chemistry*, vol. 20, no. 1, pp. 1–45, 1990.

[42] G. Miller and S. Kauzlarich, "Chemistry, structure, and bonding of zintl phases and ions," *VCH, New York*, p. 1, 1996.

[43] M. Nikitin and S. Skipidarov, *Thermoelectrics for Power Generation: A Look at Trends in the Technology*. BoD–Books on Demand, 2016.

[44] E. S. Toberer, P. Rauwel, S. Gariel, J. Taftø, and G. J. Snyder, "Composition and the thermoelectric performance of β-zn4sb3," *Journal of materials chemistry*, vol. 20, no. 44, pp. 9877–9885, 2010.

[45] G. J. Snyder, M. Christensen, E. Nishibori, T. Caillat, and B. B. Iversen, "Disordered zinc in zn 4 sb 3 with phonon-glass and electron-crystal thermoelectric properties," *Nature materials*, vol. 3, no. 7, pp. 458–463, 2004.

[46] S. B. Zhang and J. E. Northrup, "Chemical potential dependence of defect formation energies in gaas: Application to ga self-diffusion," *Phys Rev Lett*, vol. 67, no. 17, pp. 2339–2342, 1991.

[47] D. R. Gaskell and D. E. Laughlin, *Introduction to the thermodynamics of materials*. Boca Raton, FL: CRC Press, Taylor Francis, sixth edition. ed., 2017.

[48] A. Einstein, "Revision of my work "planck's theory of radiation"," *Annalen Der Physik*, vol. 22, no. 4, pp. 800–800, 1907.

[49] W. Shockley and J. L. Moll, "Solubility of flaws in heavily-doped semiconductors," *Physical Review*, vol. 119, no. 5, pp. 1480–1482, 1960.

[50] D. G. Cahill and R. O. Pohl, "Lattice-vibrations and heat-transport in crystals and glasses," *Annual Review of Physical Chemistry*, vol. 39, pp. 93–121, 1988.

[51] S. Ohno, U. Aydemir, M. Amsler, J.-H. Pöhls, S. Chanakian, A. Zevalkink, M. A. White, S. K. Bux, C. Wolverton, and G. J. Snyder, "Achieving zt $>$ 1 in inexpensive zintl phase ca9 zn4+ x sb9 by phase boundary mapping," *Advanced Functional Materials*, vol. 27, no. 20, 2017.

[52] G. J. Snyder and E. S. Toberer, "Complex thermoelectric materials," *Nature Materials*, vol. 7, no. 2, pp. 105–114, 2008.

[53] G. J. Snyder, A. H. Snyder, M. Wood, R. Gurunathan, B. H. Snyder, and C. Niu, "Weighted mobility," *Adv Mater*, p. e2001537, 2020.

[54] A. Jain, S. P. Ong, G. Hautier, W. Chen, W. D. Richards, S. Dacek, S. Cholia, D. Gunter, D. Skinner, G. Ceder, and K. A. Persson, "Commentary: The materials project: A materials genome approach to accelerating materials innovation," *APL Materials*, vol. 1, no. 1, 2013.

[55] A. F. May and G. J. Snyder, "Introduction to modeling thermoelectric transport at high temperatures," *Materials, Preparation, and Characterization in Thermoelectrics*, pp. K1–K18, 2012.

[56] D. J. Singh and D. Parker, "Electronic and transport properties of zintl phase aemg2pn2, ae=ca,sr,ba, pn=as,sb,bi in relation to mg3sb2," *Journal of Applied Physics*, vol. 114, no. 14, 2013.

[57] H. Tamaki, H. K. Sato, and T. Kanno, "Isotropic conduction network and defect chemistry in $Mg_{3+\delta}Sb_2$-based layered zintl compounds with high thermoelectric performance," *Advanced Materials*, vol. 28, no. 46, pp. 10182–10187.

[58] M. V. V. Iordanishvili and E. K., "A.f. ioffe and origin of modern semiconductor thermoelectric energy conversion," *Proc. XVII Internatinoal Conference on Thermoelectrics (ICT 98)*, vol. 1, pp. 37–42, 1998.

[59] Song, *Review of Research on the Thermoelectric Material ZnSb*, book section Chapter 6. 2016.

[60] D.-B. Xiong, N. L. Okamoto, and H. Inui, "Enhanced thermoelectric figure of merit in p-type ag-doped znsb nanostructured with ag3sb," *Scripta Materialia*, vol. 69, no. 5, pp. 397–400, 2013.

[61] Z.-h. Zheng, P. Fan, J.-t. Luo, G.-x. Liang, P.-j. Liu, and D.-p. Zhang, "Enhanced thermoelectric properties of cu doped znsb based thin films," *Journal of Alloys and Compounds*, vol. 668, pp. 8–12, 2016.

[62] M. Fedorov, L. Prokof'eva, D. Pshenay-Severin, A. Shabaldin, and P. Konstantinov, "New interest in intermetallic compound znsb," *Journal of electronic materials*, vol. 43, no. 6, pp. 2314–2319, 2014.

[63] K. Valset, P. H. M. Böttger, J. Taftø, and T. G. Finstad, "Thermoelectric properties of cu doped znsb containing zn3p2 particles," *Journal of Applied Physics*, vol. 111, no. 2, 2012.

[64] M. I. Fedorov, L. V. Prokofieva, Y. I. Ravich, P. P. Konstantinov, D. A. Pshenay-Severin, and A. A. Shabaldin, "Thermoelectric efficiency of intermetallic compound znsb," *Semiconductors*, vol. 48, no. 4, pp. 432–437, 2014.

[65] E. Chalfin, H. Lu, and R. Dieckmann, "Cation tracer diffusion in the thermoelectric materials cu3mo6se8 and "β-zn4sb3"," *Solid State Ionics*, vol. 178, no. 5-6, pp. 447–456, 2007.

[66] L. Bjerg, G. K. H. Madsen, and B. B. Iversen, "Ab initio calculations of intrinsic point defects in znsb," *Chemistry of Materials*, vol. 24, no. 11, pp. 2111–2116, 2012.

[67] V. Stevanović, S. Lany, X. Zhang, and A. Zunger, "Correcting density functional theory for accurate predictions of compound enthalpies of formation: Fitted elemental-phase reference energies," *Physical Review B*, vol. 85, no. 11, p. 115104, 2012.

[68] A. D. LaLonde, T. Ikeda, and G. J. Snyder, "Rapid consolidation of powdered materials by induction hot pressing," *Review of Scientific Instruments*, vol. 82, no. 2, p. 025104, 2011.

[69] M. Warzecha, J. Owen, M. Wimmer, F. Ruske, J. Hotovy, and J. Hüpkes, "High mobility annealing of transparent conductive oxides," in *IOP Conference Series: Materials Science and Engineering*, vol. 34, p. 012004, IOP Publishing, 2012.

[70] J. Schultz, J. P. McHugh, and W. Tiller, "Effects of heavy deformation and annealing on the electrical properties of bi2te3," *Journal of Applied Physics*, vol. 33, no. 8, pp. 2443–2450, 1962.

[71] J. Bardeen, "Electrical conductivity of metals," *Journal of Applied Physics*, vol. 11, no. 2, pp. 88–111, 1940.

[72] T. Sekimoto, K. Kurosaki, H. Muta, and S. Yamanaka, "Annealing effect on thermoelectric properties of ticosb half-heusler compound," *Journal of alloys and compounds*, vol. 394, no. 1-2, pp. 122–125, 2005.

[73] T. Watanabe, "Grain boundary engineering: historical perspective and future prospects," *Journal of Materials Science*, vol. 46, pp. 4095–4115, Jun 2011.

[74] K. Imasato, M. Wood, J. J. Kuo, and G. J. Snyder, "Improved stability and high thermoelectric performance through cation site doping in n-type La-doped $Mg_3Sb_{1.5}Bi_{0.5}$," *Journal of Materials Chemistry A*, vol. 6, no. 41, pp. 19941–19946, 2018.

[75] W. Taylor, N. Odell, and H. Fan, "Grain boundary barriers in germanium," *Physical Review*, vol. 88, no. 4, p. 867, 1952.

[76] G. Pike and C. Seager, "The dc voltage dependence of semiconductor grain-boundary resistance," *Journal of Applied Physics*, vol. 50, no. 5, pp. 3414–3422, 1979.

[77] J. Mao, J. Shuai, S. Song, Y. Wu, R. Dally, J. Zhou, Z. Liu, J. Sun, Q. Zhang, C. dela Cruz, S. Wilson, Y. Pei, D. J. Singh, G. Chen, C.-W. Chu, and Z. Ren, "Manipulation of ionized impurity scattering for achieving high thermoelectric performance in n-type Mg_3Sb_2-based materials," *Proceedings of the National Academy of Sciences*, 2017.

[78] R. German, *Sintering: from empirical observations to scientific principles*. Butterworth-Heinemann, 2014.

[79] Z. Fan, Y. Wang, B. Zhou, and J. Zhang, "Equilibrium pseudobinary al–mg 2 si phase diagram," *Materials science and technology*, vol. 17, no. 5, pp. 494–496, 2001.

[80] C. Li, Y. Wu, H. Li, and X. Liu, "Microstructural formation in hypereutectic al–mg2si with extra si," *Journal of Alloys and Compounds*, vol. 477, no. 1-2, pp. 212–216, 2009.

[81] F. C. Campbell, *Phase diagrams: understanding the basics*. ASM international, 2012.

[82] W. D. Callister and D. G. Rethwisch, *Materials science and engineering: an introduction*, vol. 7. John Wiley & Sons New York, 2007.

[83] A. D. LaLonde, T. Ikeda, and G. J. Snyder, "Rapid consolidation of powdered materials by induction hot pressing," *Review of Scientific Instruments*, vol. 82, no. 2, 2011.

[84] M. T. Agne, K. Imasato, S. Anand, K. Lee, S. K. Bux, A. Zevalkink, A. J. Rettie, D. Y. Chung, M. G. Kanatzidis, and G. J. Snyder, "Heat capacity of Mg_3Sb_2, Mg_3Bi_2, and their alloys at high temperature," *Materials Today Physics*, vol. 6, pp. 83–88, 2018.

[85] S. R. Brown, S. M. Kauzlarich, F. Gascoin, and G. J. Snyder, "Yb14mnsb11: New high efficiency thermoelectric material for power generation," *Chemistry of Materials*, vol. 18, no. 7, pp. 1873–1877, 2006.

[86] J. H. Grebenkemper, Y. F. Hu, D. Barrett, P. Gogna, C. K. Huang, S. K. Bux, and S. M. Kauzlarich, "High temperature thermoelectric properties of yb14mnsb11 prepared from reaction of mnsb with the elements," *Chemistry of Materials*, vol. 27, no. 16, pp. 5791–5798, 2015.

[87] Y. Hu, G. Cerretti, E. L. Kunz Wille, S. K. Bux, and S. M. Kauzlarich, "The remarkable crystal chemistry of the ca14alsb11 structure type, magnetic and thermoelectric properties," *Journal of Solid State Chemistry*, vol. 271, pp. 88–102, 2019.

[88] J. P. Fleurial, "Thermoelectric power generation materials: Technology and application opportunities," *Jom*, vol. 61, no. 4, pp. 79–85, 2009.

[89] D. Cheikh, B. E. Hogan, T. Vo, P. Von Allmen, K. Lee, D. M. Smiadak, A. Zevalkink, B. S. Dunn, J.-P. Fleurial, and S. K. Bux, "Praseodymium telluride: A

high-temperature, high-zt thermoelectric material," *Joule*, vol. 2, no. 4, pp. 698–709, 2018.

[90] A. P. Justl, G. Cerretti, S. K. Bux, and S. M. Kauzlarich, "Hydride assisted synthesis of the high temperature thermoelectric phase: Yb14mgsb11," *Journal of Applied Physics*, vol. 126, no. 16, p. 165106, 2019.

[91] A. Zevalkink, D. M. Smiadak, J. L. Blackburn, A. J. Ferguson, M. L. Chabinyc, O. Delaire, J. Wang, K. Kovnir, J. Martin, L. T. Schelhas, T. D. Sparks, S. D. Kang, M. T. Dylla, G. J. Snyder, B. R. Ortiz, and E. S. Toberer, "A practical field guide to thermoelectrics: Fundamentals, synthesis, and characterization," *Applied Physics Reviews*, vol. 5, no. 2, 2018.

[92] E. S. Toberer, M. Christensen, B. B. Iversen, and G. J. Snyder, "High temperature thermoelectric efficiency inba8ga16ge30," *Physical Review B*, vol. 77, no. 7, 2008.

[93] K. Akai, T. Uemura, K. Kishimoto, T. Tanaka, H. Kurisu, S. Yamamoto, T. Koyanagi, K. Koga, H. Anno, and M. Matsuura, "First-principles study of semiconducting clathrate ba8al16ge30," *Journal of Electronic Materials*, vol. 38, no. 7, pp. 1412–1417, 2009.

[94] Xie, "Beneficial contribution of alloy disorder to electron and phonon transport in half-heusler thermoelectric materials," *Advanced Functional Materials*, vol. 23, no. 41, pp. 5123–5130, 2013.

[95] X. Shi, Y. Pei, G. J. Snyder, and L. Chen, "Optimized thermoelectric properties of mo3sb7xtex with significant phonon scattering by electrons," *Energy Environmental Science*, vol. 4, no. 10, pp. 4086–4095, 2011.

[96] H.-S. Kim, N. A. Heinz, Z. M. Gibbs, Y. Tang, S. D. Kang, and G. J. Snyder, "High thermoelectric performance in (bi 0.25 sb 0.75) 2 te 3 due to band convergence and improved by carrier concentration control," *Materials Today*, vol. 20, no. 8, pp. 452–459, 2017.

[97] I. T. Witting, F. Ricci, T. C. Chasapis, G. Hautier, and G. J. Snyder, "The thermoelectric properties of n-type bismuth telluride: Bismuth selenide alloys bi2te3xsex," *Research*, vol. 2020, pp. 1–15, 2020.

[98] Y. Pei, X. Shi, A. LaLonde, H. Wang, L. Chen, and G. J. Snyder, "Convergence of electronic bands for high performance bulk thermoelectrics," *Nature*, vol. 473, no. 7345, pp. 66–9, 2011.

[99] A. F. May, D. J. Singh, and G. J. Snyder, "Influence of band structure on the large thermoelectric performance of lanthanum telluride," *Physical Review B*, vol. 79, no. 15, 2009.

[100] Y. Tang, Z. M. Gibbs, L. A. Agapito, G. Li, H. S. Kim, M. B. Nardelli, S. Curtarolo, and G. J. Snyder, "Convergence of multi-valley bands as the electronic origin of high thermoelectric performance in cosb3 skutterudites," *Nat Mater*, vol. 14, no. 12, pp. 1223–8, 2015.

[101] H. Kamila, P. Sahu, A. Sankhla, M. Yasseri, H.-N. Pham, T. Dasgupta, E. Mueller, and J. de Boor, "Analyzing transport properties of p-type mg2si–mg2sn solid solutions: optimization of thermoelectric performance and insight into the electronic band structure," *Journal of Materials Chemistry A*, vol. 7, no. 3, pp. 1045–1054, 2019.

[102] L. Hu, T. Zhu, X. Liu, and X. Zhao, "Point defect engineering of high-performance bismuth-telluride-based thermoelectric materials," *Advanced Functional Materials*, vol. 24, no. 33, pp. 5211–5218, 2014.

[103] E. L. Kunz Wille, N. S. Grewal, S. K. Bux, and S. M. Kauzlarich, "Seebeck and figure of merit enhancement by rare earth doping in yb14-xrexznsb11 (x = 0.5)," *Materials (Basel)*, vol. 12, no. 5, pp. 731–743, 2019.

[104] Y. Hu, J. Wang, A. Kawamura, K. Kovnir, and S. M. Kauzlarich, "Yb14mgsb11 and ca14mgsb11—new mg-containing zintl compounds and their structures, bonding, and thermoelectric properties," *Chemistry of Materials*, vol. 27, no. 1, pp. 343–351, 2014.

[105] W. Tan, Z. Wu, M. Zhu, J. Shen, T. Zhu, X. Zhao, B. Huang, X. T. Tao, and S. Q. Xia, "A14mgbi11 (a = ca, sr, eu): Magnesium bismuth based zintl phases as potential thermoelectric materials," *Inorg Chem*, vol. 56, no. 17, pp. 10576–10583, 2017.

[106] Y. Wang, Y. J. Hu, S. A. Firdosy, K. E. Star, J. P. Fleurial, V. A. Ravi, L. Q. Chen, S. L. Shang, and Z. K. Liu, "First-principles calculations of lattice dynamics and thermodynamic properties for yb14mnsb11," *Journal of Applied Physics*, vol. 123, no. 4, pp. 045102–45112, 2018.

[107] M. T. Agne, R. Hanus, and G. J. Snyder, "Minimum thermal conductivity in the context of diffuson-mediated thermal transport," *Energy Environmental Science*, vol. 11, no. 3, pp. 609–616, 2018.

[108] C. J. Perez, X. Qi, Z. J. Chen, S. K. Bux, S. Chanakain, B. Li, K. Liu, R. Dhall, K. C. Bustillo, and S. M. Kauzlarich, "Improved power factor and mechanical properties of composites of yb14mgsb11 with iron," *ACS Applied Energy Materials*, vol. 3, no. 3, pp. 2147–2159, 2020.

[109] S. J. Gomez, D. Cheikh, T. Vo, P. Von Allmen, K. Lee, M. Wood, G. J. Snyder, B. S. Dunn, J.-P. Fleurial, and S. K. Bux, "Synthesis and characterization of vacancy-doped neodymium telluride for thermoelectric applications," *Chemistry of Materials*, 2019.

[110] S. Sarkar, X. Zhang, S. Hao, X. Hua, T. P. Bailey, C. Uher, C. Wolverton, V. P. Dravid, and M. G. Kanatzidis, "Dual alloying strategy to achieve a high thermoelectric figure of merit and lattice hardening in p-type nanostructured pbte," *ACS Energy Letters*, vol. 3, no. 10, pp. 2593–2601, 2018.

[111] W. Li, S. Lin, M. Weiss, Z. Chen, J. Li, Y. Xu, W. G. Zeier, and Y. Pei, "Crystal structure induced ultralow lattice thermal conductivity in thermoelectric ag9 alse6," *Advanced Energy Materials*, vol. 8, no. 18, 2018.

[112] N. Kazem, J. V. Zaikina, S. Ohno, G. J. Snyder, and S. M. Kauzlarich, "Coinage-metal-stuffed eu9cd4sb9: Metallic compounds with anomalous low thermal conductivities," *Chemistry of Materials*, vol. 27, no. 21, pp. 7508–7519, 2015.

[113] E. L. Kunz Wille, N. H. Jo, J. C. Fettinger, P. C. Canfield, and S. M. Kauzlarich, "Single crystal growth and magnetic properties of the mixed valent yb containing zintl phase, yb14mgsb11," *Chem Commun (Camb)*, vol. 54, no. 92, pp. 12946–12949, 2018.

[114] A. He, E. L. K. Wille, L. M. Moreau, S. M. Thomas, J. M. Lawrence, E. D. Bauer, C. H. Booth, and S. M. Kauzlarich, "Intermediate yb valence in the zintl phases yb14msb11 (m = mn, mg, zn): Xanes, magnetism, and heat capacity," *Advanced Materials (Submitted)*, 2020.

[115] A. P. Holm, T. C. Ozawa, S. M. Kauzlarich, S. A. Morton, G. Dan Waddill, and J. G. Tobin, "X-ray photoelectron spectroscopy studies of yb14mnsb11 and yb14znsb11," *Journal of Solid State Chemistry*, vol. 178, no. 1, pp. 262–269, 2005.

[116] Y. F. Hu, G. Cerretti, E. L. K. Wille, S. K. Bux, and S. M. Kauzlarich, "The remarkable crystal chemistry of the ca14alsb11 structure type, magnetic and thermoelectric properties," *Journal of Solid State Chemistry*, vol. 271, pp. 88–102, 2019.

[117] H. J. Goldsmid and J. W. Sharp, "Estimation of the thermal band gap of a semiconductor from seebeck measurements," *Journal of Electronic Materials*, vol. 28, no. 7, pp. 869–872, 1999.

[118] R. W. McKinney, P. Gorai, V. Stevanović, and E. S. Toberer, "Search for new thermoelectric materials with low lorenz number," *Journal of Materials Chemistry A*, vol. 5, no. 33, pp. 17302–17311, 2017.

[119] A. Putatunda and D. J. Singh, "Lorenz number in relation to estimates based on the seebeck coefficient," *Materials Today Physics*, vol. 8, pp. 49–55, 2019.

[120] M. Thesberg, H. Kosina, and N. Neophytou, "On the lorenz number of multiband materials," *Physical Review B*, vol. 95, no. 12, 2017.

[121] Y. Pei, A. D. LaLonde, H. Wang, and G. J. Snyder, "Low effective mass leading to high thermoelectric performance," *Energy Environmental Science*, vol. 5, no. 7, 2012.

[122] Y. F. Hu, K. Lee, and S. M. Kauzlarich, "Optimization of ca14mgsb11 through chemical substitutions on sb sites: Optimizing seebeck coefficient and resistivity simultaneously," *Crystals*, vol. 8, no. 5, pp. 211–221, 2018.

[123] J. F. Rauscher, C. A. Cox, T. Yi, C. M. Beavers, P. Klavins, E. S. Toberer, G. J. Snyder, and S. M. Kauzlarich, "Synthesis, structure, magnetism, and high temperature thermoelectric properties of ge doped yb14mnsb11," *Dalton Trans*, vol. 39, no. 4, pp. 1055–62, 2010.

[124] S. R. Brown, E. S. Toberer, T. Ikeda, C. A. Cox, F. Gascoin, S. M. Kauzlarich, and G. J. Snyder, "Improved thermoelectric performance in yb14mn1xznxsb11by the reduction of spin-disorder scattering," *Chemistry of Materials*, vol. 20, no. 10, pp. 3412–3419, 2008.

[125] T. Hom, W. Kiszenik, and B. Post, "Accurate lattice constants from multiple reflection measurements. ii. lattice constants of germanium silicon, and diamond," *Journal of Applied Crystallography*, vol. 8, no. 4, pp. 457–458, 1975.

[126] J. F. Bérar and P. Lelann, "E.s.d.'s and estimated probable error obtained in rietveld refinements with local correlations," *Journal of Applied Crystallography*, vol. 24, no. 1, pp. 1–5, 1991.

[127] V. Ravi, S. Firdosy, T. Caillat, E. Brandon, K. Van der Walde, L. Maricic, and A. Sayir, "Thermal expansion studies of selected high-temperature thermoelectric materials," *Journal of Electronic Materials*, vol. 38, no. 7, pp. 1433–1442, 2009.

[128] C. A. Cox, E. S. Toberer, A. A. Levchenko, S. R. Brown, G. J. Snyder, A. Navrotsky, and S. M. Kauzlarich, "Structure, heat capacity, and high-temperature thermal properties of yb14mn1xalxsb11," *Chemistry of Materials*, vol. 21, no. 7, pp. 1354–1360, 2009.

[129] K. A. Borup, E. S. Toberer, L. D. Zoltan, G. Nakatsukasa, M. Errico, J. P. Fleurial, B. B. Iversen, and G. J. Snyder, "Measurement of the electrical resistivity and hall coefficient at high temperatures," *Rev Sci Instrum*, vol. 83, no. 12, pp. 123902–123909, 2012.

[130] C. Wood, D. Zoltan, and G. Stapfer, "Measurement of seebeck coefficient using a light-pulse," *Review of Scientific Instruments*, vol. 56, no. 5, pp. 719–722, 1985.

[131] W. Kohn and L. J. Sham, "Self-consistent equations including exchange and correlation effects," *Physical Review*, vol. 140, no. 4A, pp. A1133–A1138, 1965.

[132] P. E. Blochl, "Projector augmented-wave method," *Phys Rev B Condens Matter*, vol. 50, no. 24, pp. 17953–17979, 1994.

[133] G. Kresse and D. Joubert, "From ultrasoft pseudopotentials to the projector augmented-wave method," *Physical Review B*, vol. 59, no. 3, pp. 1758–1775, 1999.

[134] J. P. Perdew, K. Burke, and M. Ernzerhof, "Generalized gradient approximation made simple," *Physical review letters*, vol. 77, no. 18, p. 3865, 1996.

[135] G. K. H. Madsen and D. J. Singh, "Boltztrap. a code for calculating band-structure dependent quantities," *Computer Physics Communications*, vol. 175, no. 1, pp. 67–71, 2006.

[136] Madsen, "Boltztrap2, a program for interpolating band structures and calculating semi-classical transport coefficients," *Computer Physics Communications*, vol. 231, pp. 140–145, 2018.

[137] S. P. Ong, W. D. Richards, A. Jain, G. Hautier, M. Kocher, S. Cholia, D. Gunter, V. L. Chevrier, K. A. Persson, and G. Ceder, "Python materials genomics (pymatgen): A robust, open-source python library for materials analysis," *Computational Materials Science*, vol. 68, pp. 314–319, 2013.

[138] W. Setyawan and S. Curtarolo, "High-throughput electronic band structure calculations: Challenges and tools," *Computational Materials Science*, vol. 49, no. 2, pp. 299–312, 2010.

[139] G. S. Pomrehn, A. Zevalkink, W. G. Zeier, A. van de Walle, and G. J. Snyder, "Defect- controlled electronic properties in azn2sb2 zintl phases," *Angewandte Chemie-International Edition*, vol. 53, no. 13, pp. 3422–3426, 2014.

[140] F. Gascoin, S. Ottensmann, D. Stark, S. aïle, and G. nyder, "Zintl phases as thermoelectric materials: Tuned transport properties of the compounds caxyb1–xzn2sb2," *Advanced Functional Materials*, vol. 15, no. 11, pp. 1860–1864, 2005.

[141] A. F. May, M. A. McGuire, D. J. Singh, J. Ma, O. Delaire, A. Huq, W. Cai, and H. Wang, "Thermoelectric transport properties of camg2bi2, eumg2bi2, and ybmg2bi2," *Physical Review B*, vol. 85, no. 3, 2012.

[142] D. Stark, G. J. Snyder, Ieee, and Ieee, *The synthesis of CaZn2Sb2 and its thermoelectric properties.* Xxi International Conference on Thermoelectrics, Proceedings Ict '02, New York: Ieee, 2002.

[143] E. S. Toberer, A. F. May, B. C. Melot, E. Flage-Larsen, and G. J. Snyder, "Electronic structure and transport in thermoelectric compounds azn(2)sb(2) (a = sr, ca, yb, eu)," *Dalton Transactions*, vol. 39, no. 4, pp. 1046–1054, 2010.

[144] A. Zevalkink, W. G. Zeier, E. Cheng, J. Snyder, J. P. Fleurial, and S. Bux, "Nonstoichiometry in the zintl phase yb1-delta zn2sb2 as a route to thermoelectric optimization," *Chemistry of Materials*, vol. 26, no. 19, pp. 5710–5717, 2014.

[145] K. Guo, Q.-G. Cao, X.-J. Feng, M.-B. Tang, H.-H. Chen, X. Guo, L. Chen, Y. Grin, and J.-T. Zhao, "Enhanced thermoelectric figure of merit of zintl phase ybcd2-xmnxsb2 by chemical substitution," *European Journal of Inorganic Chemistry*, vol. 2011, no. 26, pp. 4043–4048, 2011.

[146] J. Shuai, H. Geng, Y. Lan, Z. Zhu, C. Wang, Z. Liu, J. Bao, C. W. Chu, J. Sui, and Z. Ren, "Higher thermoelectric performance of zintl phases (eu0.5yb0.5)1-xcaxmg2bi2 by band engineering and strain fluctuation," *Proc Natl Acad Sci U S A*, vol. 113, no. 29, pp. E4125–32, 2016.

[147] J. Shuai, Z. Liu, H. S. Kim, Y. Wang, J. Mao, R. He, J. Sui, and Z. Ren, "Thermoelectric properties of bi-based zintl compounds ca1xybxmg2bi2," *Journal of Materials Chemistry A*, vol. 4, no. 11, pp. 4312–4320, 2016.

[148] J. Shuai, Y. Wang, H. S. Kim, Z. Liu, J. Sun, S. Chen, J. Sui, and Z. Ren, "Thermoelectric properties of na-doped zintl compound: Mg 3 x na x sb 2," *Acta Materialia*, vol. 93, pp. 187–193, 2015.

[149] L. Song, J. Zhang, and B. B. Iversen, "Simultaneous improvement of power factor and thermal conductivity via ag doping in p-type mg3sb2 thermoelectric materials," *Journal of Materials Chemistry A*, vol. 5, no. 10, pp. 4932–4939, 2017.

[150] J. K. Burdett and G. J. Miller, "Fragment formalism in main-group solids - applications to alb2, caal2si2, baal4, and related materials," *Chemistry of Materials*, vol. 2, no. 1, pp. 12–26, 1990.

[151] J. F. Sun and D. J. Singh, "Thermoelectric properties of amg(2)x(2), azn(2)sb(2) (a = ca, sr, ba; x = sb, bi), and ba2znx2 (x = sb, bi) zintl compounds," *Journal of Materials Chemistry A*, vol. 5, no. 18, pp. 8499–8509, 2017.

[152] Z. M. Gibbs, H. Kim, H. Wang, R. L. White, F. Drymiotis, M. Kaviany, and G. Jeffrey Snyder, "Temperature dependent band gap in pbx (x=s, se, te)," *Applied Physics Letters*, vol. 103, no. 26, 2013.

[153] S. D. Kang and G. J. Snyder, "Transport property analysis method for thermoelectric materials: material quality factor and the effective mass model," *arXiv:1710.06896*, 2017.

[154] J. Yang, G. P. Meisner, and L. Chen, "Strain field fluctuation effects on lattice thermal conductivity of zrnisn-based thermoelectric compounds," *Applied Physics Letters*, vol. 85, no. 7, pp. 1140–1142, 2004.

[155] J. J. Kuo, S. D. Kang, K. Imasato, H. Tamaki, S. Ohno, T. Kanno, and G. J. Snyder, "Grain boundary dominated charge transport in mg3sb2-based compounds," *Energy Environmental Science*, 2018.

[156] B. Abeles, "Lattice thermal conductivity of disordered semiconductor alloys at high temperatures," *Physical Review*, vol. 131, no. 5, pp. 1906–, 1963.

[157] P. G. Klemens, "Thermal resistance due to point defects at high temperatures," *Physical Review*, vol. 119, no. 2, pp. 507–509, 1960.

[158] J. Callaway and H. C. Vonbaeyer, "Effect of point imperfections on lattice thermal conductivity," *Physical Review*, vol. 120, no. 4, pp. 1149–1154, 1960.

[159] P. G. Klemens, "The scattering of low-frequency lattice waves by static imperfections," *Proceedings of the Physical Society of London Section A*, vol. 68, no. 12, pp. 1113–1128, 1955.

[160] J. Zhang, L. Song, M. Sist, K. Tolborg, and B. B. Iversen, "Chemical bonding origin of the unexpected isotropic physical properties in thermoelectric mg3sb2 and related

materials," *Nat Commun*, vol. 9, no. 1, p. 4716, 2018.

[161] J. Zhang, L. Song, A. Mamakhel, M. R. V. Jørgensen, and B. B. Iversen, "High-performance low-cost n-type se-doped mg3sb2-based zintl compounds for thermoelectric application," *Chemistry of Materials*, vol. 29, no. 12, pp. 5371–5383, 2017.

[162] X. Sun, X. Li, J. Yang, J. Xi, R. Nelson, C. Ertural, R. Dronskowski, W. Liu, G. J. Snyder, D. J. Singh, and W. Zhang, "Achieving band convergence by tuning the bonding ionicity in n-type mg3 sb2," *J Comput Chem*, vol. 40, no. 18, pp. 1693–1700, 2019.

[163] K. Imasato, S. D. Kang, S. Ohno, and G. J. Snyder, "Band engineering in mg3sb2 by alloying with mg3bi2 for enhanced thermoelectric performance," *Materials Horizons*, vol. 5, no. 1, pp. 59–64, 2018.

[164] K. Imasato, S. D. Kang, and G. J. Snyder, "Exceptional thermoelectric performance in mg3sb0.6bi1.4 for low-grade waste heat recovery," *Energy Environmental Science*, vol. 12, no. 3, pp. 965–971, 2019.

[165] P. Gorai, B. R. Ortiz, E. S. Toberer, and V. Stevanović, "Investigation of n-type doping strategies for mg3sb2," *Journal of Materials Chemistry A*, vol. 6, no. 28, pp. 13806–13815, 2018.

[166] P. Gorai, E. S. Toberer, and V. Stevanović, "Effective n-type doping of mg3sb2 with group-3 elements," *Journal of Applied Physics*, vol. 125, no. 2, 2019.

[167] S. W. Song, J. Mao, M. Bordelon, R. He, Y. M. Wang, J. Shuai, J. Y. Sun, X. B. Lei, Z. S. Ren, S. Chen, S. Wilson, K. Nielsch, Q. Y. Zhang, and Z. F. Ren, "Joint effect of magnesium and yttrium on enhancing thermoelectric properties of n-type zintl mg3+y0.02sb1.5bi0.5," *Materials Today Physics*, vol. 8, pp. 25–33, 2019.

[168] J. Zhang, L. Song, K. A. Borup, M. R. V. Jørgensen, and B. B. Iversen, "New insight on tuning electrical transport properties via chalcogen doping in n-type mg3 sb2 -based thermoelectric materials," *Advanced Energy Materials*, vol. 8, no. 16, 2018.

[169] X. Shi, T. Zhao, X. Zhang, C. Sun, Z. Chen, S. Lin, W. Li, H. Gu, and Y. Pei, "Extraordinary n-type mg3 sbbi thermoelectrics enabled by yttrium doping," *Adv Mater*, p. e1903387, 2019.

[170] H. Wang, Y. Pei, A. D. LaLonde, and G. Jeffery Snyder, *Material Design Considerations Based on Thermoelectric Quality Factor*, pp. 3–32. Berlin, Heidelberg: Springer Berlin Heidelberg, 2013.

[171] H. Wang, X. Cao, Y. Takagiwa, and G. J. Snyder, "Higher mobility in bulk semiconductors by separating the dopants from the charge-conducting band – a case study of thermoelectric pbse," *Materials Horizons*, vol. 2, no. 3, pp. 323–329, 2015.

[172] M. Wood, U. Aydemir, S. Ohno, and G. J. Snyder, "Observation of valence band crossing: the thermoelectric properties of cazn2sb2–camg2sb2 solid solution," *Journal of Materials Chemistry A*, vol. 6, no. 20, pp. 9437–9444, 2018.

[173] H. Wang, Y. Pei, A. D. LaLonde, and G. J. Snyder, *Material design considerations based on thermoelectric quality factor*, pp. 3–32. Springer, 2013.

[174] J. Zhang and B. B. Iversen, "Fermi surface complexity, effective mass, and conduction band alignment in n-type thermoelectric mg3sb2–xbix from first principles calculations," *Journal of Applied Physics*, vol. 126, no. 8, 2019.

[175] W. Kohn, A. D. Becke, and R. G. Parr, "Density functional theory of electronic structure," *The Journal of Physical Chemistry*, vol. 100, no. 31, pp. 12974–12980, 1996.

[176] G. Kresse and J. Furthmüller, "Efficient iterative schemes for ab initio total-energy calculations using a plane-wave basis set," *Physical review B*, vol. 54, no. 16, p. 11169, 1996.

[177] S. Maintz, V. L. Deringer, A. L. Tchougréeff, and R. Dronskowski, "Analytic projection from plane-wave and paw wavefunctions and application to chemical-bonding analysis in solids," *Journal of computational chemistry*, vol. 34, no. 29, pp. 2557–2567, 2013.

[178] V. L. Deringer, A. L. Tchougréeff, and R. Dronskowski, "Crystal orbital hamilton population (cohp) analysis as projected from plane-wave basis sets," *The journal of physical chemistry A*, vol. 115, no. 21, pp. 5461–5466, 2011.

[179] R. Dronskowski and P. E. Blöchl, "Crystal orbital hamilton populations (cohp): energy-resolved visualization of chemical bonding in solids based on density-functional calculations," *The Journal of Physical Chemistry*, vol. 97, no. 33, pp. 8617–8624, 1993.

[180] J. J. Kuo, M. Wood, T. Slade, M. G. Kanatzidis, and G. J. Snyder, "Systematic over-estimation of lattice thermal conductivity in materials with electrically-resistive grain boundaries," *Energy Environmental Science*, 2020.

[181] B. M. Askerov, *Electron transport phenomena in semiconductors*. World scientific, 1994.

[182] S. D. Kang and G. J. Snyder, "Charge-transport model for conducting polymers," *Nature Materials*, vol. 16, no. 2, pp. 252–257, 2017.

[183] V. I. Fistul, *Heavily doped semiconductors*, vol. 1. Springer Science Business Media, 2012.

[184] Ziman, *Electrons and phonons: the theory of transport phenomena in solids*. Oxford university press, 2001.

APPENDIX A

The Effects of Multiple Bands on Thermoelectric Transport

A.1. Transport Function

Charge transport in a material can be described very generally using a transport function (σ_E) formalism. Using the Boltzmann transport equation for charged particles that obey Fermi-Dirac statistics we can arrive at the following for electrical conductivity (σ), Seebeck coefficient (α), and electronic thermal conductivity (κ_e).[91;182;181;183;184;55]

$$\sigma = \int \sigma_E(E) \left(-\frac{\partial f}{\partial E}\right) dE \tag{A.1}$$

$$\alpha = \frac{k_B}{e} \frac{\int \sigma_E(E) \left(-\frac{\partial f}{\partial E}\right) \left(\frac{E-E_f}{k_B T}\right) dE}{\int \sigma_E(E) \left(-\frac{\partial f}{\partial E}\right) dE} \tag{A.2}$$

$$\kappa_e = \left(\frac{k_B}{e}\right)^2 \frac{\int \sigma_E(E) \left(-\frac{\partial f}{\partial E}\right) \left(\frac{E-E_f}{k_B T}\right)^2 dE}{\int \sigma_E(E) \left(-\frac{\partial f}{\partial E}\right) dE} - \alpha^2 \sigma T \tag{A.3}$$

Where k_B is Boltzmann's constant, e is the elementary charge, T is temperature, E_f is Fermi level, $\sigma_E(E)$ is the energy dependent transport function, and $\left(-\frac{\partial f}{\partial E}\right)$ is the derivative of the Fermi-Dirac distribution with respect to carrier energy. The Fermi-Dirac distribution is given by:

$$f(E) = \frac{1}{1 + \exp\left(\frac{E - E_f}{k_B T}\right)} \tag{A.4}$$

An important observation when comparing these transport equations is the different energy dependence of their selection functions ($\sigma \rightarrow \left(-\frac{\partial f}{\partial E}\right)$, $\alpha \rightarrow \left(-\frac{\partial f}{\partial E}\right)\left(\frac{E-E_f}{k_B T}\right)$, $\kappa_e \rightarrow \left(-\frac{\partial f}{\partial E}\right)\left(\frac{E-E_f}{k_B T}\right)^2$). The differences in these selection functions leads to each of the transport coefficients proportionally sampling energy states at different breadths. This leads to the conductivity (σ) selection function sampling the narrowest window of carrier energies, and the electronic thermal conductivity (κ_e) sampling the broadest window of carrier energies (Figure A.1).

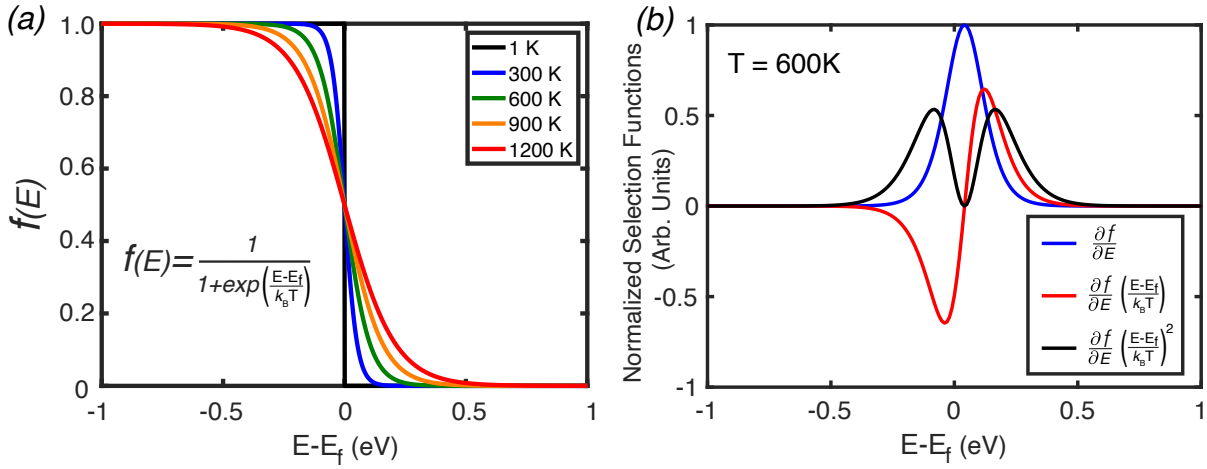

Figure A.1: (a) The distribution of fermions around the Fermi level given by the Fermi-Dirac distribution at 1K, 300K, 600K, 900K, and 1200K. (b) Selection functions for electrical conductivity, Seebeck Coefficient, and electronic thermal conductivity normalized to be on the same scale. Notice how the selection function for electronic thermal conductivity selects a broader extent of energies than the electrical conductivity selection function does.

A.2. Effective Mass Model

In a semi-classical band conduction formalism, the transport function of a material can be approximated by:

$$\sigma(E) = \frac{e^2}{3}\tau\left(E\right)\nu^2\left(E\right)g(E) \tag{A.5}$$

Where $\tau\left(E\right)$ is the relaxation time, $\nu\left(E\right)$ is the velocity of the carrier, and $g(E)$ is the density of states averaged over all states with energy E. The transport in a material that has only a single transport edge, can be described using an effective mass model. In this framework an effective mass (m^*) for a parabolic dispersion relationship ($E = \frac{\hbar^2 k^2}{2m^*}$) is found that gives the same transport properties as those measured, at a given temperature and doping level. From this dispersion relationship the velocity and 3D density of states of charge carriers in a material is given as function of energy.

$$\nu\left(E\right) = \left(\frac{2E}{m^*}\right)^{\frac{1}{2}} \tag{A.6}$$

$$g\left(E\right) = \frac{m^{*3/2}\left(2E\right)^{\frac{1}{2}}}{\pi^2\hbar^3} \tag{A.7}$$

The energy dependence of the relaxation time, $\tau(E)$, is dependent on the scattering mechanisms present in the material and is given by:

$$\tau(E) = \tau_0 \bullet \left(\frac{E}{k_B T}\right)^r \tag{A.8}$$

Here τ_0 is a reference relaxation time for carriers at $k_B T$ above the band edge and r is characteristic of the scattering mechanism present in the material. Above room temperature $r = -\frac{1}{2}$, used in the effective mass model, is commonly found in thermoelectric materials, which describes the energy dependence of acoustic and nonpolar optical phonon scattering[55]. Substituting S5, S6, and S7 into S4 with nonpolar phonon scattering and introducing the mobility parameter $\mu_0 = \frac{e\tau_0}{m^*}$ we find:

$$\sigma_E(E) = \frac{e\left(2m_e k_B T\right)^{\frac{3}{2}}}{3\pi^2\hbar^3} \bullet \mu_0 \left(\frac{m^*}{m_e}\right)^{\frac{3}{2}} \bullet \left(\frac{E}{k_B T}\right)^1 \tag{A.9}$$

Where $\mu_0 \left(\frac{m^*}{m_e}\right)^{\frac{3}{2}}$ is sometimes referred to as the weighted mobility as it is weighted by the material's effective mass[53]. Using a phonon scattering energy dependence the transport function is linear with energy and goes to 0 at the band edge (Figure A.2).

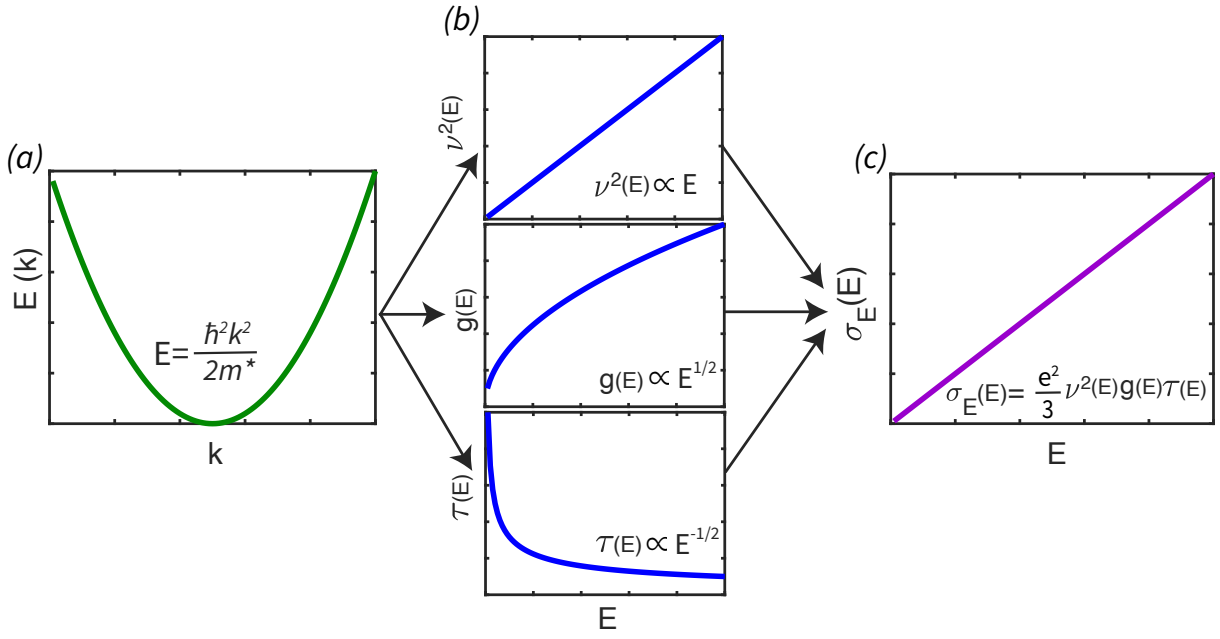

Figure A.2: (a) Parabolic dispersion relationship for an electron. (b) Energy dependence of charge carrier velocity ($\nu(E)$), density of states ($g(E)$), and relaxation time ($\tau(E)$) using a non-polar phonon scattering energy dependence. (c) The energy dependence of the transport function $\sigma_E(E)$ arising from non-polar phonon scattering.

A.3. Adding Additional Bands

So far, we have been using a transport function σ_E that is linear with energy, which is useful for describing transport arising from a single or multiple bands that have their transport edge at one particular energy. However, transport arising from multiple bands with transport edges offset in energy can also be described using the transport function framework as well. If we approximate that bands in the material are non-interacting and no intervalley scattering is present, like two independent transport channels in parallel, then the transport function becomes:

$$\sigma_{En}(E) = \sum_{i=1}^{n} \sigma_{Ei}(E) - \Delta_i \tag{A.10}$$

Where $\sigma_{En}(E)$ describes the total transport function of a material with n bands active in transport, $\sigma_{Ei}(E)$ describes the transport function of an single indexed band, and Δ_i represents the energy difference between the band edge of the currently indexed band to the band edge of the first band indexed.

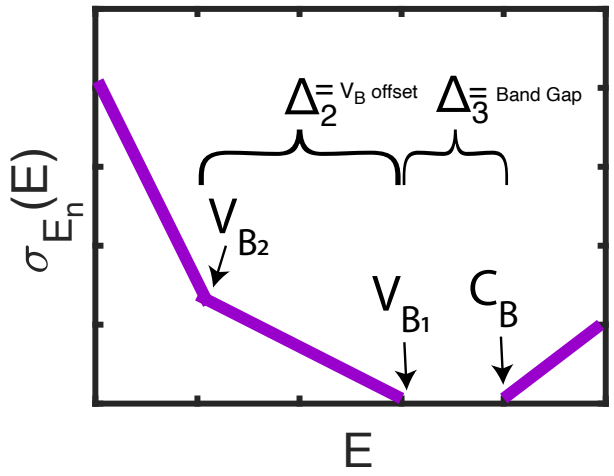

Figure A.3: The transport function of a material with 2 valence bands and one conduction band involved in transport. VB1 identifies the band edge of the first valence band, VB2 identifies the band edge of the second valence band, and CB identifies the band edge of the conduction band. Δ_2 shows the distance between the first and second valence band, while Δ_3 shows the distance between the first valence band and the conduction band, which forms the material's band gap.

A.4. Temperature Consideration

Temperature changes in a material will lead to a change in the occupation statistics of the Fermi-Dirac distribution as well as a possible change in the Fermi level placement

relative to the material's band edge(s). In the simulated data seen in Figure 3 (main paper), the Fermi level relative to the band edges was determined as a function of temperature by assuming charge neutrality in the material is maintained. In assuming charge neutrality in a p-type material, we state that the total number of holes in the material cannot increase with temperature unless it is compensated by an electron. If the Fermi-Dirac distribution is only selecting single carrier type states in two different bands, then as the function's broadening changes with temperature the proportional occupation of states from each band will change. The carrier concentration of a material is given by:

$$n = \int g(E) f dE \tag{A.11}$$

Where the density of states $g(E)$ for a single band is given by equation A.7 and the density of states for a multi band system is given by:

$$g_n(E) = \frac{\sqrt{2}}{\pi^2 \hbar^3} \sum_{i=1}^{n} m_i^{*\frac{3}{2}} \; E^{\frac{1}{2}} - \Delta_i \tag{A.12}$$

Where $g_n(E)$ describes the total density of states in a material with n bands active in transport, m_i^* is the density of states effective mass of an indexed band, and Δ_i again represents the energy difference between the band edge of the currently indexed band to the band edge of the first band indexed (Figure A.3). Therefore, using equations A.11

and A.4, and the information that charge neutrality must be maintained we can numerically solve for how the Fermi level in a material that changes with temperature. For example a material with two valence bands and one conduction band involved in transport would be governed by p1 + p2 - n = c, where p1 is the number of holes in the first band, p2 is the number of holes in the second band, n is the number of electrons in the conduction band, and c is a constant.

In addition to determining the effects a changing temperature has on a material's Fermi-level, we must also consider the effects temperature has on the mobility and therefore transport function. Experimentally the mobility of non-degenerate $Yb_{14}AlSb_{11}$, follows a $T^{-1.5}$ trend indicative of phonon scattering in a non-degenerate material. The resistivity of Yb14MgSb11 meanwhile follows a T^{-1}, which is also indicative of phonon scattering in a degenerately doped semi-conductor where the intrinsic mobility parameter has the same $T^{-1.5}$ dependence as the non-degenerate case[181]. Based on these observations we model the intrinsic mobility (μ_0) of each band to decreases proportionally to $T^{-1.5}$ consistent with the energy dependence of phonon scattering used previously[183].

A.5. Multi-Band Model Example Visualization

For the modeled transport data, a three-band model was created using DFT inputs for the band offsets between the two conduction bands (E_{offset} = 0.315 eV) as well as the band gap (E_{gap} = 0.586 eV). Additional inputs needed for this model are the intrinsic mobility and effective mass of each band. We find that following parameters qualitatively describe the experimental data measured, however slight adjustments in these parameters would also likely suffice. The intrinsic mobility for each band was set at 25 cm^2/Vs at

300K and decreased proportionally to $T^{-1.5}$ with temperature. The DOS mass of the first valence band (m*VB1) was set to $1m_e$, the DOS mass of the second valence band (m*VB2) was set to $5m_e$, and the DOS mass of the conduction band (m*CB) was set to $4m_e$. For all simulated data the carrier concentration was kept fixed and the Fermi level was varied with temperature in order to ensure charge neutrality of the simulated sample[55;91]. We would like to point out that the features in the Seebeck coefficient and thermal conductivity vs temperature and doping level that this paper set out to investigate cannot be explained by a transport function of a single band, and require the two valence bands offset in energy to be accurately described.

To begin an explanation of why a material material incongurently, we must begin with why any material sublimates. The simplest place to start is from an classical ideal gas model in which gas particles particles follow Maxwell-Boltzmann statistics where particles are considered non interacting.

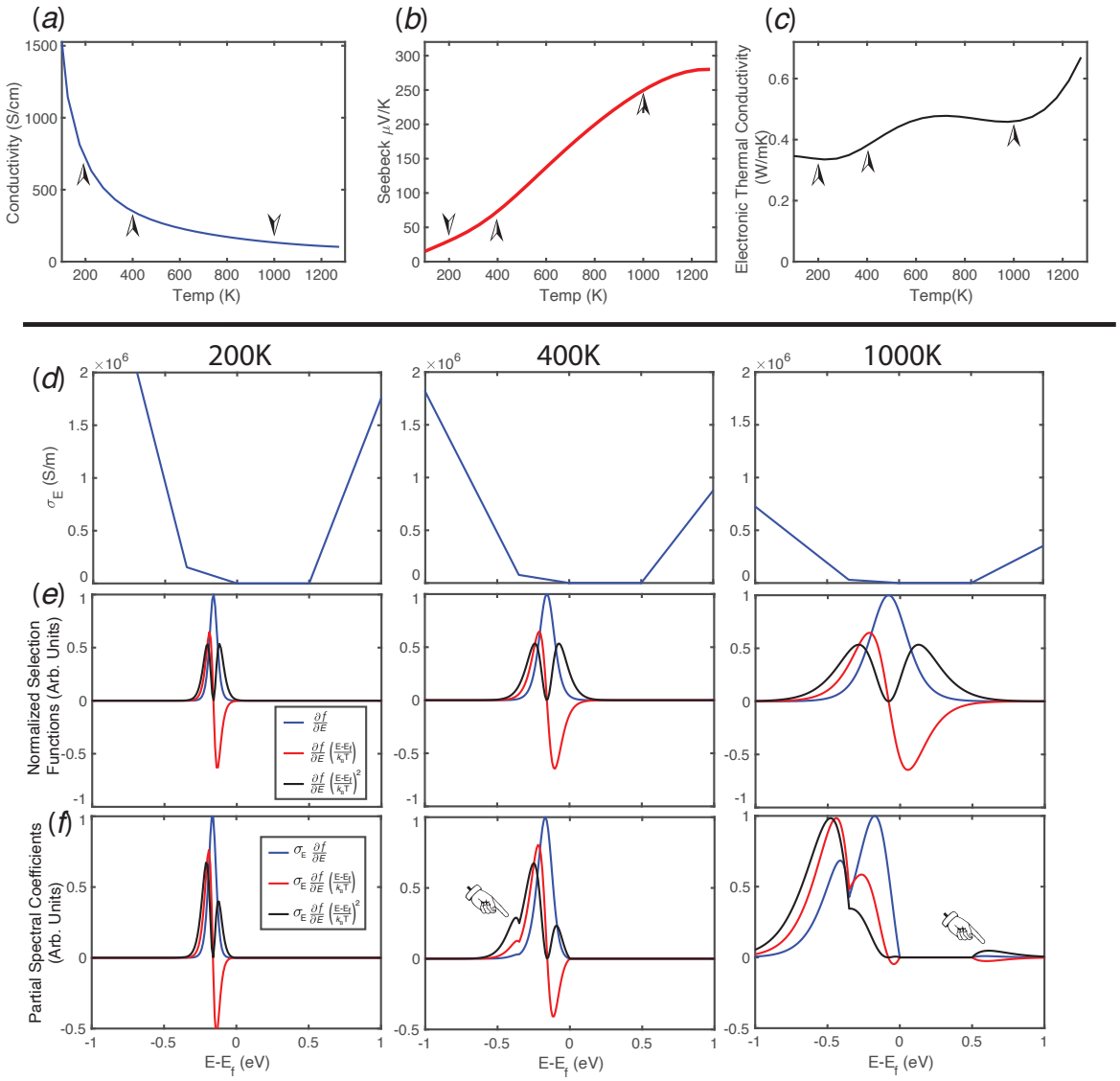

Figure A.4: (*Continued on next page) Modeled (a) electrical conductivity, (b) Seebeck coefficient, and (c) electronic thermal conductivity as a function of temperature using the three-band model inputs described in this paper for $Yb_{14}Mg_{1-x}Al_xSb_{11}$ with a fixed carrier concentration of 3×10^{20} $1/cm^3$. Arrows indicate temperatures of 200K, 400K, and 1000K which are analyzed further in parts d-f. (d) Transport function (σ_E) vs energy at various temperatures. Notice how the magnitude in σ_E decreases with increasing temperature reflecting the reduction in mobility from additional phonon scattering at higher temperatures.

Figure A.4: (*Continued) (e) Selection functions for electrical conductivity (blue), Seebeck coefficient (red), and electronic thermal conductivity (black) at various temperatures normalized to be plotted on the same scale. Notice how as the temperature increases, all selection functions broaden, with electronic thermal conductivity broadening the most. (f) Selection functions for electrical conductivity (blue), Seebeck coefficient (red), and electronic thermal conductivity (black) multiplied by the transport function (σ_E), which is proportional to the spectral function of each transport coefficient. Notice where the finger is pointing out an increase in the spectral thermal conductivity that is absent in the electrical conductivity due to the different sampling extents of the selection functions. This difference in selection function breadth accounts for the increase in thermal conductivity with temperature that is not seen in the electrical conductivity.

Vita

First & Co-First Author Papers

- **The importance of the Mg–Mg interaction in Mg 3 Sb 2–Mg 3 Bi 2 shown through cation site alloying** (Max Wood, Kazuki Imasato, Shashwat Anand, Jiong Yang and G Jeffrey Snyder), *In Journal of Materials Chemistry A*, Royal Society of Chemistry, volume 8, pp. 2033-2038, 2020.
- **Systematic over-estimation of lattice thermal conductivity in materials with electrically-resistive grain boundaries** (Jimmy Jiahong Kuo, Max Wood, Tyler J Slade, Mercouri G Kanatzidis and G Jeffrey Snyder), *In Energy & Environmental Science*, Royal Society of Chemistry, volume 13, pp. 1250-1258, 2020.
- **Improvement of Low-Temperature zT in a Mg3Sb2–Mg3Bi2 Solid Solution via Mg-Vapor Annealing** (Maxwell Wood, Jimmy Jiahong Kuo, Kazuki Imasato and Gerald Jeffrey Snyder), *In Advanced Materials*, volume 31, pp. 1902337, 2019.
- **Observation of valence band crossing: the thermoelectric properties of CaZn 2 Sb 2–CaMg 2 Sb 2 solid solution** (Max Wood, Umut Aydemir, Saneyuki Ohno and G Jeffrey Snyder), *In Journal of Materials Chemistry A*, Royal Society of Chemistry, volume 6, pp. 9437-9444, 2018.
- **Discovery of Multi-Valley Fermi Surface Responsible for the High Thermoelectric Performance in Yb14MnSb11 and Yb14MgSb11** (Christopher J. Perez, Max Wood, Francesco Ricci, Guodong Yu, Trinh Vo, Sabah K. Bux, Geoffroy Hautier, Gian-Marco Rignanese, G. Jeffrey Snyder, and Susan M. Kauzlarich), submitted.

- **Interfacial Seebeck Coefficient Uncovers Energy Filtering Effect in Graphene Wrapped Mg3Sb2** (Yue Lin, Maxwell Wood, Kazuki Imasato1, Jimmy Jiahong Kuo1, David Lam, Nooshin Mortazavi, Tyler J. Slade, Stephen A. Hodge, Kai Xi, Mercouri G. Kanatzidis, David R. Clarke, Mark C. Hersam, G. Jeffrey Snyder), submitted.
- **Phase Boundary Mapping of Tin-Doped ZnSb Reveals Synthesis Route to High Thermoelectric Efficiency** (Max Wood, Michael Y. Toriyama, Shristi Dugar, James Male, Shashwat Anand, and G. Jeffrey Snyder), In P reparation.

Contributing Author

- **Understanding the thermally activated charge transport in NaPb m SbQ m+ 2 (Q= S, Se, Te) thermoelectrics: weak dielectric screening leads to grain boundary dominated charge carrier scattering** (Tyler J Slade, Jann A Grovogui, Jimmy Jiahong Kuo, Shashwat Anand, Trevor P Bailey, Maxwell Wood, Ctirad Uher, G Jeffrey Snyder, Vinayak P Dravid and Mercouri G Kanatzidis), *In Energy & Environmental Science*, Royal Society of Chemistry, 2020.
- **Metallic n-Type Mg3Sb2 Single Crystals Demonstrate the Absence of Ionized Impurity Scattering and Enhanced Thermoelectric Performance** (Kazuki Imasato, Chenguang Fu, Yu Pan, Max Wood, Jimmy Jiahong Kuo, Claudia Felser and G Jeffrey Snyder), *In Advanced Materials*, volume 32, pp. 1908218, 2020.
- **Transition from crystal-like to amorphous-like heat conduction in structurally-complex crystals** (Riley Hanus, Janine George, Max Wood, Yongqiang Cheng, Douglas L Abernathy, Michael E Manley, Geoffroy Hautier, G Jeffrey Snyder and Raphaël P Hermann), *In* , ChemRxiv, 2020. 2019
- **Synergistically optimizing carrier concentration and decreasing sound velocity in n-type AgInSe2 thermoelectrics** (Yingcai Zhu, Yong Liu, Max Wood, Nathan Z Koocher, Yanyu Liu, Lijuan Liu, Tiandou Hu, James M Rondinelli, Jiawang Hong, G Jeffrey Snyder and

others), *In Chemistry of Materials*, American Chemical Society, volume 31, pp. 8182-8190, 2019.

- **Effect of anion substitution on the structural and transport properties of argyrodites Cu 7 PSe 6- x S x** (Friederike Reissig, Barbara Heep, Martin Panthöfer, Max Wood, Shashwat Anand, G Jeffrey Snyder and Wolfgang Tremel), *In Dalton Transactions*, Royal Society of Chemistry, volume 48, pp. 15822-15829, 2019.
- **Synthesis and characterization of vacancy-doped neodymium telluride for thermoelectric applications** (Steven J Gomez, Dean Cheikh, Trinh Vo, Paul Von Allmen, Kathleen Lee, Max Wood, G Jeff Snyder, Bruce S Dunn, Jean-Pierre Fleurial and Sabah K Bux), *In Chemistry of Materials*, American Chemical Society, volume 31, pp. 4460-4468, 2019.
- **Double Half-Heuslers** (Shashwat Anand, Max Wood, Yi Xia, Chris Wolverton and G Jeffrey Snyder), *In Joule*, Cell Press, volume 3, pp. 1226-1238, 2019. 2018
- **Improved stability and high thermoelectric performance through cation site doping in n-type La-doped Mg 3 Sb 1.5 Bi 0.5** (Kazuki Imasato, Max Wood, Jimmy Jiahong Kuo and G Jeffrey Snyder), *In Journal of Materials Chemistry A*, Royal Society of Chemistry, volume 6, pp. 19941-19946, 2018. 2017
- **Metal phosphides as potential thermoelectric materials** (Jan-Hendrik Pöhls, Alireza Faghaninia, Guido Petretto, Umut Aydemir, Francesco Ricci, Guodong Li, Max Wood, Saneyuki Ohno, Geoffroy Hautier, G Jeffrey Snyder and others), *In Journal of Materials Chemistry C*, Royal Society of Chemistry, volume 5, pp. 12441-12456, 2017.
- **Superstrengthening Bi 2 Te 3 through Nanotwinning** (Guodong Li, Umut Aydemir, Sergey I Morozov, Max Wood, Qi An, Pengcheng Zhai, Qingjie Zhang, William A Goddard III and G Jeffrey Snyder), *In Physical review letters*, American Physical Society, volume 119, pp. 085501, 2017.
- **Micro-and macromechanical properties of thermoelectric lead chalcogenides** (Guodong Li, Umut Aydemir, Bo Duan, Matthias T Agne, Hongtao Wang, Max Wood, Qingjie Zhang,

Pengcheng Zhai, William A Goddard III and G Jeffrey Snyder), *In ACS applied materials & interfaces*, American Chemical Society, volume 9, pp. 40488-40496, 2017.

- **Mechanical properties of thermoelectric lanthanum telluride from quantum mechanics** (Guodong Li, Umut Aydemir, Max Wood, William A Goddard III, Pengcheng Zhai, Qingjie Zhang and G Jeffrey Snyder), *In Journal of Physics D: Applied Physics*, IOP Publishing, volume 50, pp. 274002, 2017.
- **Ideal strength and deformation mechanism in high-efficiency thermoelectric SnSe** (Guodong Li, Umut Aydemir, Max Wood, William A Goddard III, Pengcheng Zhai, Qingjie Zhang and G Jeffrey Snyder), *In Chemistry of Materials*, American Chemical Society, volume 29, pp. 2382-2389, 2017.
- **Deformation mechanisms in high-efficiency thermoelectric layered Zintl compounds** (Guodong Li, Umut Aydemir, Max Wood, Qi An, William A Goddard III, Pengcheng Zhai, Qingjie Zhang and G Jeffrey Snyder), *In Journal of Materials Chemistry A*, Royal Society of Chemistry, volume 5, pp. 9050-9059, 2017.
- **Defect-controlled electronic structure and phase stability in thermoelectric skutterudite CoSb3** (Guodong Li, Umut Aydemir, Max Wood, William A Goddard III, Pengcheng Zhai, Qingjie Zhang and G Jeffrey Snyder), *In Chemistry of Materials*, American Chemical Society, volume 29, pp. 3999-4007, 2017.
- **A computational assessment of the electronic, thermoelectric, and defect properties of bournonite (CuPbSbS 3) and related substitutions** (Alireza Faghaninia, Guodong Yu, Umut Aydemir, Max Wood, Wei Chen, Gian-Marco Rignanese, G Jeffrey Snyder, Geoffroy Hautier and Anubhav Jain), *In Physical Chemistry Chemical Physics*, Royal Society of Chemistry, volume 19, pp. 6743-6756, 2017. 2016
- **Structure and failure mechanism of the thermoelectric CoSb3/TiCoSb interface** (Guodong Li, Shiqiang Hao, Umut Aydemir, Max Wood, William A Goddard III, Pengcheng Zhai, Qingjie Zhang and G Jeffrey Snyder), *In ACS Applied Materials & Interfaces*, American Chemical Society, volume 8, pp. 31968-31977, 2016.

- **Enhanced ideal strength of thermoelectric half-Heusler TiNiSn by sub-structure engineering** (Guodong Li, Qi An, Umut Aydemir, William A Goddard III, Max Wood, Pengcheng Zhai, Qingjie Zhang and G Jeffrey Snyder), *In Journal of Materials Chemistry A*, Royal Society of Chemistry, volume 4, pp. 14625-14636, 2016. 2015
- **Oxygen trapped by rare earth tetrahedral clusters in Nd4FeOS6: Crystal structure, electronic structure, and magnetic properties** (Qisheng Lin, Valentin Taufour, Yuemei Zhang, Max Wood, Thomas Drtina, Sergey L Bud'ko, Paul C Canfield and Gordon J Miller), *In Journal of Solid State Chemistry*, Academic Press, volume 229, pp. 41-48, 2015.